Characterisation of volcanic emissions through thermal vision

Maxime Bombrun

N° d'ordre: D.U. : 2600
EDSPIC : 708

UNIVERSITÉ BLAISE PASCAL - CLERMONT-FERRAND II

ÉCOLE DOCTORALE
SCIENCES POUR L'INGÉNIEUR DE CLERMONT-FERRAND

T H È S E

Présentée par

Maxime BOMBRUN

pour obtenir le grade de

DOCTEUR D'UNIVERSITÉ

Spécialité : Informatique & Géologie

Characterisation of Volcanic Emissions through Thermal Vision

---

soutenue publiquement le 1 octobre 2015

JURY

M. Vincent Charvillat	Rapporteur	Professeur à l'ENSEEIHT de Toulouse
M. Clive Oppenheimer	Rapporteur	Professeur à University of Cambridge
M. Thierry Chateau	Examinateur	Professeur à l'Université Blaise Pascal
M. Jacopo Taddeucci	Examinateur	Chercheur à INGV Roma
M. Vincent Barra	Directeur de Thèse	Professeur à l'Université Blaise Pascal
M. Andrew Harris	Directeur de Thèse	Professeur à l'Université Blaise Pascal

A mon père.

Acknowledgments

Cette thèse s'est déroulée dans le cadre du programme "Laboratoire d'Excellence" du pôle de recherche ClerVolc. Elle est le résultat de la collaboration du Laboratoire d'Informatique, Modélisation et Optimisation des Systèmes (LIMOS) et du Laboratoire Magmas et Volcans (LMV) de l'Université Blaise Pascal à Clermont-Ferrand.

First, I would like to thank M. Clive Oppenheimer who accepted to be member of my committee and who took the time to share his point of view about my work. I also wish to express my sincere gratitude to M. Jacopo Taddeucci who helped me like a third supervisor. I am truly grateful that he supported me during all my conferences, most of my field trips and once more for my defence. Merci également à M. Vincent Charvillat d'avoir accepté d'être rapporteur de cette thèse et pour ses conseils avisés quant à l'amélioration du manuscript. Enfin, un grand merci à M. Thierry Chateau pour avoir accepté de présider ma thèse, mais aussi pour m'avoir apporter de précieux conseils et su orienter mes recherches au travers de nos différents entretiens.

Cette thèse n'aurait pu arriver à terme sans la présence d'importantes personnes; Maxime Fouquemberg, Guillaume Paugam et Théophile Lohier ainsi que la "famille", parisienne et lyonnaise (en particulier Aurélie Dhenry, pour la relecture). Les collègues du LIMOS et ceux du LMV que j'ai rencontré aux quatre coins du monde bien plus qu'à Clermont. Enfin merci

à ma famille pour le soutien infaillible apporté pendant ces trois ans.

Finalement, je voudrais remercier mes deux directeurs de thèse, Vincent Barra et Andrew Harris. Vincent me connait depuis cinq ans, il a su me pousser toujours à fond dans mes idées, m'orienter sans contraindres et surtout, il a toujours su me faire confiance. Andy on the other hand, knows me for only three years. However, these years were full of adventures, laughs and negronis. All this could not have been possible without him, trusting me from our first meeting. I would like to thanks them both, to have make me a better person and a better scientist.

Abstract

Characterisation of Volcanic Emissions through Thermal Vision

In April 2010, the eruption of Eyjafjallajökull (Iceland) threw volcanic ash across northwest Europe for six days which led to air travel disruption. This recent crisis spotlighted the necessity to parameterise plume dynamics through emission, dispersion and fall out as to better model, track and forecast cloud motions. This eruption was labeled as a Strombolian-to-Sub-Plinian eruption type. Strombolian eruptions are coupled with a large range of volcanic event types (Lava flows, paroxysms) and eruption styles (Hawaiian, Sub-plinian) and offer a partial precursory-indicator of more dangerous eruptions. In addition, strombolian eruptions are small enough to allow observations from within few hundred meters with relative safety, for both operators and material. Since 2001, thermal cameras have been increasingly used to track, parameterise and understand dynamic volcanic events. However, analyses, modelling and post-processing of thermal data are still not fully automated. In this thesis, I focus on the different components of strombolian eruptions at the full range of remote sensing spatial scales. These range from millimeters for particles to kilometers for the entire features via satellite images. Overall, I aim to characterise volcanic emissions through thermal vision.

Keywords: Thermal imagery, Remote sensing, Strombolian eruptions, Particles, Plumes, Lava fountaining, Ash-rich thermals, Detection, Tracking

Caractérisation des Emissions Volcaniques par la Vision Thermique

En avril 2010, l'éruption de l'Eyjafjallajökull (Islande) a projetée des cendres sur toutes l'Europe pendant six jours, causant d'importantes perturbations aériennes. Cette crise a soulever la nécessité de mieux comprendre la dynamique des panaches lors de l'émission, de la dispersion, et de la retombée afin d'améliorer les modèles de suivis et de prédiction de ces phénomènes. Cette éruption a été classée comme Strombolienne. Ce type d'éruption offre un large panel de manifestations (coulée de lave, paroxysmes) et peut être utilisé comme indicateur d'éruptions plus dangereuses. Les éruptions stromboliennes permettent généralement une observation à quelques centaines de mètres tout en assurant la sécurité des opérateurs et du matériel. Depuis 2001, les caméras thermiques ont été de plus en plus utilisées pour comprendre la dynamique des évènements volcaniques. Toutefois, l'analyse, la modélisation et le post-traitement de ces données thermiques n'est toujours pas totalement informatisé. Durant ma thèse, j'ai étudié les différentes composantes d'une éruption strombolienne depuis les fines particules éjectées au niveau du cratère jusqu'à la vision d'ensemble offerte par les images satellites. Dans l'ensemble, j'ai caractérisé les émissions volcaniques à travers l'imagerie thermique.

Mots-clefs: Imagerie thermique, Télédétection, Eruptions stromboliennes, Détection, Suivi, Particules, Panaches, Fountaines de lave , Thermiques riche en cendres.

Contents

Listing of figures

Résumé

En avril 2010, l'éruption de l'Eyjafjallajökull (Islande) a projetée des cendres volcaniques sur toutes l'Europe pendant six jours, causant d'importantes perturbations aériennes [Gudmundsson et al., 2012; Langman et al, 2012; Petersen et al., 2012]. Cette crise a mis en avant la nécessité de mieux comprendre la dynamique des panaches au niveau de l'émission, de la dispersion, et de la retombée afin d'améliorer les modèles de suivis et de prédiction de ces phénomènes. Cette éruption a été classée comme Strombolienne. On retrouve ce type d'activité chez les volcans des cinq continents tels que Stromboli, Etna, Yasur et Fuego [liste exhaustive pour 2002 présentée dans Smithsonian Institution, 2005]. Les éruptions strombolienes sont relativement puissantes [Macdonald, 1972], on les classe en terme d'intensité et de magnitude entre les éruptions de type Hawaïennes et Vulcaniennes [Newhall and Self, 1982]. Les éruptions stromboliennes sont des petits évènements explosifs pouvant monter à des milliers de mètres de hauteur et survenant plus régulièrement que les Vulcaniennes, par exemple, Stromboli a une moyenne de 13 éruptions par heure [Harris and Ripepe, 2007a]. Elles sont aussi remarquables pour les arcs paraboliques incandescents tracés par les ejectas

fondus. Les émissions de bombes, blocs, lapilli et de cendres visibles sont courantes durant une activité explosive normale. Toutefois, les coulées de laves [Barberi et al., 1993], les éruptions riches en cendre [Patrick, 2007], ainsi que les paroxysmes entrainant des panaches à plusieurs kilomètres dans l'atmosphère [Ripepe and Harris, 2008], sont aussi des évènements arrivant fréquemment. L'activité strombolienne apparait aussi dans les phases de croissance et/ou de déclin de certaines éruptions plus puissantes [Vergniolle and Mangan, 2000]. Par exemple, plusieurs mois d'activité strombolienne ont précédés les éruptions sub-pliniennes du Shishaldin (Alaska) en 1999 [Dehn et al., 2002]. Ainsi, ce type d'éruption offre un large panel de manifestations et peut être utilisé comme indicateur d'éruptions plus dangereuses. De plus, les éruptions stromboliennes permettent généralement une observation à quelques centaines de mètres [Chouet et al., 1974; Blackburn et al., 1976] tout en assurant la sécurité des opérateurs et du matériel [Ripepe et al., 2004]. A Stromboli, l'activité a été observée et étudiée pendant plusieurs siècles [Washington, 1917]. Durant cette période, l'évolution constante de la technologie et la prolifération des équipements de surveillance ont améliorés notre compréhension de la dynamique du conduit et du comportement explosif [voir Harris and Ripepe, 2007a et Ripepe et al., 2008].

Au cours des vingt dernières années, la communauté volcanologique a largement accepté la télédetection thermique comme une opérationelle contribution à la surveillance et l'étude des volcans. Les volcans actifs émettent de la chaleur au travers des coulées de lave, des dômes, des lacs, du dégasement et des cratères éruptifs. Depuis 2001, les caméras thermiques ont été de plus en plus utilisées pour comprendre la dynamique des évènements volcaniques [Harris, 2013] supplantant peu à peu les analyses basées sur satellite [e.g. Dehn et al., 2001; Sahetapy-Engel and Harris, 2009; Spampinato et al., 2011; Vanderkluysen et al., 2012; Valade et al.,

2014]. Le télémesurement de l'émission de chaleur et l'exploitation des données collectées par les caméras thermiques, les satellites et/ou les radiomètres fournissent une meilleur compréhension des phénomènes volcaniques et de la dynamique des éruptions [e.g. Francis and Rothery, 1987; Oppenheimer, 1989; Holasek et al., 1996; Harris et al., 1997c; 1997d; Oppenheimer and Francis, 1997; Wooster and Rothery 1997; Oppenheimer, 1998; Dehn et al., 2000], procurant ainsi une autre approche pour les études multidisciplinaires visant à la compréhension, le suivi, la prévision, l'atténuation et la réponse aux crises éruptives. Les équipements infrarouges ont l'avantage majeur de résoudre les éléments chauds que la brume, le brouillard ou les conditions gazeuses empêcheraient de voir à l'oeil nu. Toutefois, la complexité et la taille de ces jeux de données aggravent le surplus de données inexploités et les analyses basiques, la modélisation et le post-traitement des données thermiques ne sont toujours pas complètement automatisés. De nombreux paramètres essentiels pour configurer les modèles sont encore difficiles a extraire au point de nécessité le développement de méthodologies innovantes. Pour un évènement volcanique en temps-réel, des paramètres, comme le flux de masse, la vitesse d'ascension (ou de diffusion), et le taux d'accroissement du panache ou de la lave, sont fondamentaux pour comprendre la dynamique des éruptions explosives et effusives, et les mécanismes à la source qui les gouvernent.

La motivation principale de cette thèse était d'étudier les différentes composantes d'une éruption strombolienne depuis les fines particules éjectées au niveau du cratère jusqu'à la vision d'ensemble offerte par les images satellites. Dans l'ensemble, j'ai caractérisé les émissions volcaniques à travers l'imagerie thermique et ainsi, développer les algorithms *ad hoc* à l'analyse de ses composantes. Je me suis principalement concentré sur le développement de méthodologies automatisées pour l'extraction de paramètres de panaches d'explosions de

systèmes stromboliens. Leur activité est relativement faible, mais fournit un large panel de phénomènes et de niveau de fragmentation (panaches, coulées de lave, bombes, lapilli, cendres) qui peuvent être modélisés facilement, puis réévalués pour prévoir le comportement de types explosifs plus dangereux. Parmis les nombreux volcans avec une activité strombolienne, plusieurs permettent un enregistrement à une centaines de mètres de distance du cratère et fournissant une solide source de données devenant des exceptionnels laboratoires naturels pour l'étude de la source et de la dynamique des émissions explosives.

Le premier chapitre passe en revue l'état de l'art de la télédétection thermique et son utilisation dans le suivi de l'activité volcanique. Dans cette thèse, je m'intéressais aux systèmes de télédétection basé au sol et dans l'espace, spécifiquement dans le domaine de l'infrarouge (8-14 μm). Pour la télédétection au sol, j'ai utilisé deux types d'instruments (ou capteurs) pour mesurer les photons: les caméras et les radiomètres (annexes A.1, A.3, A.4). A la différence du radiomètre qui collecte le flux énergétique en un seul point, la camera enregistre le flux énergétique en l'ensemble des points ou pixels qui compose le détecteur qui permet de former l'image. Pour ce faire, les radiations infrarouge frappe le détecteur, le chauffe et change sa résistance électrique. Ainsi, chaque pixels est caractérisé pour un bref moment par une seul valeur de radiation (e.g., la radiance spectrale) correspondant à son changement de résistance. Une fois mesurée, le changement de résistance peut être converti, par l'effect photoélectrique, en un nombre d'électrons et peut être transformer en température qui peut être attribuée au pixel dans l'image. La plupart de ces instruments utilisent un microbolomètre qui, contrairement à d'autres types de détecteurs, ne demande pas de refroidissement ce qui économise du temps, du poids, de la masse et de l'argent. L'un des plus importants aspect de la fonction et la performance du capteur, est la résolution de l'image. La résolution d'un capteur est le plus pe-

tit changement qu'il peut détecter dans l'échantillon qu'il mesure. Par exemple, la résolution d'une caméra est le plus petit objet clairement visible avec des limites distinctes. La résolution des caméras digitales peut être définies de plusieurs manières (pixel, spatiale, temporelle, spectrale). Pour la télédétéction depuis l'espace, j'ai utilisé le radiomètre avancé à très haute résolution (AVHRR, annexe A.5). Les instruments AVHRR sont des types de capteurs spatiaux principalement utilisé pour la recherche sur le changement climatique, comme la météorologie, l'évolution de la couche d'ozone, les effets de la déforestation et l'impact d'autres désastres naturels. Toutefois, les récentes avancées fournissent des mesurements pour des applications dans le civil (cartographie en ligne). En effet, la science de l'imagerie infrarouge s'est développée rapidement dans de nombreux domaines [Kylili et al., 2014]. L'utilisation des caméras thermiques dans le civil permet la lutte contre les incendies [Amon and Pearson, 2009], la surveillance des bâtiments [Kylili et al., 2014], la médecine [Arora et al., 2008], les systèmes de diagnostic assistés par ordinateur [Faust et al., 2014], la surveillance [Caballero et al., 2001] et la volcanologie [Harris, 2013]. Les utilisations de caméras thermiques en volcanologie ont été classées en cinq groupes principaux par Spampinato et al. [2011], ceux-ci étant les études des

1. zones hydrothermales et des champs de fumerolles;
2. organismes de lave;
3. activités explosives et des panaches volcaniques;
4. dépôts de coulée pyroclastique;
5. fracturations et des fissurations.

L'acquisition au sol permet l'étude de ces groupes mais impose plusieurs limites de sécurité et de logistique; le personnel et le matériel doivent être une zone sûre pour pouvoir enregistrer. En conséquence, des systèmes moins chers, permanents et automatiques ont été installés sur plusieurs volcans (voir Harris [2013] pour détail). Ils transmettent les données à un site d'observation, où un degré de traitement automatisé est nécessaire. L'objectif principal de l'acquisition par satellite est la détection et le suivi des nuages de cendre émis par les éruptions explosives et l'évaluation des risques qu'ils posent au traffic aérien. Selon Harris [2013], la plupart des avancées majeures dans l'utilisation des données satellitaires pour l'analyse de l'activité volcanique ont eu lieu durant les années 1990. Toutefois, les progrès en réception, en informatique, en traitement et en capacité de stockage fait dans les années 2000 étaient la révolution nécessaire pour faire avancer la télédétection satellite des volcans actifs, ainsi que les applications liées aux caméras et aux radiomètres.

Dans le chapitre 2, je présente une méthode pour détecter, suivre et extraire des paramètres des particules sortant du cratère, filmées par une caméra thermique haute-vitesse à Stromboli. Cette première étude se concentre sur les larges (bombes et lapilli) particules quittant le conduit. Elles sont representatives du degré de fragmentation se produisant au niveau de la source lors d'une éruption. J'ai utilisé une caméra thermique, haute vitesse pour suivre les plus rapides particules (> 300 m/s) qui, au début de cette thèse, n'avaient été que très peu observées. La caméra thermique était aussi équipée d'une lentille grossissante (annexe A.3) afin de filmer le conduit en gros plan et ainsi, enregistrer les particules au plus près de leur point de fragmentation. J'ai développé un algorithme pour détecter, suivre et paramétrer les particules pyroclastiques enregistrées en infrarouge. Cette méthode est basée sur une transformation morpho-mathématique hybridée avec un raffinement par seuillage. Le suivi est effectué par

une corrélation temporelle mais améliorée et adaptée au système. J'ai utilisé à la fois, les avantages (acquisition haute fréquence) et les défauts (artefact visuel causé par le bolomètre) de la caméra pour améliorer la précision et le contrôle du suivi. L'algorithme a montré une haute fiabilité et une capacité de détection précise sur des données expérimentales pour lesquelles des particules ont été simulées par des billes en acier de différentes tailles, chauffées dans l'eau bouillante. J'ai enregistré des vidéos infrarouge, en hautes vitesses, de 31 explosions normales à Stromboli en Octobre 2012 et Mai 2014. J'ai utilisé mon algorithme pour obtenir une base de données robuste des paramètres de 83 000 particules, tels que la vitesse, la taille, la masse et la forme de chaque particule. Statistiquement, la distribution des paramètres des 13 éruptions de 2012 est similaire à celle obtenue pour les 18 éruptions de 2014. La plupart des particules ont une taille entre 5 cm et 15 cm et la majorité des masses individuelles des bombes est en dessous de 0.4 kg. Toutefois, bien que 4 950 (6 %) des particules sont plus lourdes que 5 kg, elles représentent 59 % de la masse totale éjectée. La distribution de vitesse des particule est positivement asymétrique avec un mode entre 20 m/s et 30 m/s. L'activité explosive normale à Stromboli a généralement été considéré comme impliquant de grosses particules avec des vitesses relativement faibles, avec une moyenne d'environ 25 m/s [Chouet et al., 1974; Ripepe et al., 1993]. Récemment, cependant, Delle Donne et Ripepe [2012] et Harris et al. [2012] ont montré que quelques petites particules (typiquement de la taille d'un lapillus) peuvent être entraînées par un jet de gaz à haute vitesse, g□n□rant des vitesses moyennes de particules de 80 m/s et un maximum de 405 m/s [Taddeucci et al., 2012a]. Mes données supportent cette dualité. La résolution spatiale de notre système nous permet de détecter les particules jusqu'à 5 cm. Dans nos données plupart des bombes (taille supérieure à 6.4 cm) sont détectées, et la distribution de la vitesse des bombes a un mode situé entre 20 m/s et 30 m/s. Nos

données indiquent également que les plus petites particules, portées par le jet de gaz, ont les vitesses les plus élevées avec une vitesse maximale mesurée de 240 m/s, et une vitesse maximale potentielle estimée à 700 m/s pour les plus petits lapilli, 0.2 cm en taille, correspondant à la plus petite particule à laquelle la relation tracée sur la figure 2.16 peut être appliquée. Patrick et al. [2007] et Leduc et al. [2014] ont classés les explosions normales à Stromboli par regroupement visuel, selon si elles étaient dominées par des balistiques (Type 1), par la cendre, avec (2a) ou sans (2b) particules, ou dominées par le gaz (Type 0). A partir des mesures, j'ai pu grouper les 31 éruptions selon ces quatre même classes. La corrélation avec les données sismiques aide à comprendre le mécanisme de la source, et supporte les modèles de Gurioli et al. [2014] et Leduc et al. [2014]: les évènements de type 2a et 2b sont une conséquence de la présence d'un bouchon visqueux à la tête de la colonne de magma, sa fragmentation fournissant entre 10^3 et 10^4 kg de materiel solide à chaque éruption. Toutefois, le type 1 est une conséquence de l'éclatement du bouchon dans un conduit "plus propre", comprenant moins de matériel solide, tandis que les éruptions de type 0 n'ont quasiment pas de materiel solide. Ainsi, il faudrait modéliser l'impact du plus fin composant, la cendre dans le panache, pour complètement définir les dynamiques d'une explosions strombolienne.

Ensuite, dans le chapitre 3, j'analyse les panaches de fines particules et gaz durant leur phase d'ascension. Je présente un algorithme qui segmente automatiquement les panaches volcaniques, et extrait les paramètres clés qui peuvent être utilisé pour modéliser le comportement du panache durant son ascension et sa dispersion. Ce deuxième projet traitait des panaches volcaniques, composés de plus fine (cendre) particules. Les panaches volcaniques sont des dangereux phénomènes qui peuvent endommager les transports aériens et s'étendre sur des larges populations causant des problèmes de santé et d'architectures. Les modèles de

simulation actuels sont capable de reproduire le comportement du panache, mais demande plusieurs variables environnementales en paramètres d'entrées, qui influencent l'évolution du panache mais qui sont difficile à contraindre, particulièrement lors d'un échantillonage direct sur le site de l'éruption. Dans cette étude, j'ai utilisé une caméra thermique pour paramétrer l'ascension du panache. À distance raisonnable, les panaches sont des cibles se déplaçant lentement si bien qu'une fréquence d'acquisition d'une image par seconde est suffisante pour suivre l'évolution complète du panache au cours du temps. Toutefois, avec les capacités de stockage actuelles, un enregistrement à 30 Hz est un avantage qui permet à l'algorithme de traiter quasiment en temps réel. Cet atout est renforcé par le fait que l'algorithme est basé sur des méthodes rapides et efficace comme les transformations par ondelette, les morphologies mathématiques et la méthode d'Otsu. La détection et le suivi sont aussi totalement automatisés. Pour obtenir une valeur de vérité terrain, l'algorithme a été validé visuellement sur un jeu de données hétérogènes de vidéos thermiques et visibles. Deux cas naturels, les volcans Santiaguito et Stromboli ont été utilisés pour examiner des complications dues aux conditions changeantes du site, et trois expériences ont été réalisées pour couvrir un maximum de conditions environnementales. Les différentes conditions étaient sur l'arrière plan (vent, nuages, arbres, chaud/froid, statique/mobile, homogène/hétérogène, points chauds dans l'image, bon/mauvais contraste), sur le panache (lent/rapide, penché, chaud/froid, jet, convectif), et sur le type de données (thermique/visible). L'algorithme s'est avéré être robuste pour extraire automatiquement les paramètres du panache comme la hauteur, la largeur et l'angle de diffusion qui ont été utilisés pour calculer les valeurs des coefficients d'entraînement de l'air des jeux de donn□es qui sont cohérentes avec la littérature. Une fois que l'interface graphique pour l'utilisateur sera terminée, l'algorithme sera testé en quasi-temps réel sur un

volcan afin de valider l'implémentation d'un nouveau module pour compléter le logiciel de Valade et al., [2014] et de fournir une méthode de suivi et de paraméterisation pour la modélisation, la projection et la prévision des risques liés aux panaches volcaniques.

Le chapitre 4 suit l'évolution entre l'activité strombolienne et la fontaine de lave pour contribuer à une surveillance par radiomètre du Mont Etna. Mon algorithme détecte chaque évènement strombolien dans la montée en puissance de la fontaine de lave et extrait leurs paramètres thermiques et temporels afin de définir le mécanisme d'activation et de transition de l'activité strombolienne à la fontaine. Ce troisième projet s'intéressait au processus transitoire des épisodes de fountaines de lave. Les fontaines de lave, émises comme composante des éruptions de type Hawaïenne, sont de relativement faibles formes d'activité explosive durant laquelle des jets soutenus de particules et de gaz sont éjectés à des taux massiques de l'ordre de 10^5-10^6 kg/s en quelques heures [e.g., Mercalli, 1907; Newhall and Self, 1982; Houghton and Gonnermann, 2008]. Elles sont capable d'alimenter des panaches à plusieurs milliers de mètres d'altitude [e.g., Swanson et al., 1979; Vergniolle and Mangan, 2000; Wolff and Sumner, 2000; Andronico et al., 2008], causant des problèmes de santé et de traffic aéarien [e.g., Andronico et al., 2008; Calvari et al., 2011]. Un épisode de fontaine de lave peut durer plusieurs jours, il est donc plus facile d'obtenir une surveillance continue à partir d'une station permanente. Toutefois, les coulées de lave émanentes d'un épisode de fontaine de lave posent une réelle menace pour une installation proche du conduit et suggèrent l'utilisation de matériel à faible coût. Dans cette étude, j'ai utilisé un radiomètre bas prix, installé sur l'Etna, fin 2011, pour suivre l'activité explosive du cratère Sud-Est (SEC) et le nouveau cratère Sud-Est (NSEC); un système bien connu pour son activité de fontaine de lave fréquente [e.g., Bonaccorso et al., 2011; Calvari et al., 2011; Sciotto et al., 2011; Ganci et al., 2012; Spampinato et al., 2015 and

Fig. 4.1]. Les épisodes étudiés commençaient avec des faibles évènements stromboliens qui montaient continuellement en puissance jusqu'au climax, produisant d'immenses panaches [e.g., Calvari et al., 2011; Spampinato et al., 2015]. L'INGV de Catane a fournit huit episodes ayant eu lieu entre 2012 et le 28 Février 2013, date de la destruction du radiomètre. L'objectif était d'analyser les formes d'onde thermiques enregistrées par le radiomètre, d'extraire tout les évènements stromboliens durant la transition et de les caracteriser en terme d'énergie mais aussi sur la durée, la pente de croissance/ et de déclin. Au total, les données de huit épisodes de fontaine de lave ont fournies 1 927 évènements enregistrés et 8 537 pics, avec un nombre d'évènements variant de 66 à 650 par épisode avec une moyenne de 241 évènements par épisode. En terme de durée moyenne, on observe une légère différence entre les années, avec des durées entre 4 et 59 s en 2012 (moyenne = 18 s) et entre 4 et 55 s pour 2013 (moyenne = 21 s) (Table 4.1). Toutefois, en terme de nombre d'évènements moyen, les épisodes de 2012 en comptent plus (393) que ceux de 2013 (88), de tel sorte que la fréquence moyenne est plus élevée en 2012 (39 évènements/heure) qu'en 2013 (13 évènements/heure). La plupart des évènements ont des énergies de radiance entre 3.0×10^{6} et 5.8×10^{9} J avec une moyenne de 1.0×10^{8} J. L'énergie totale de chaque épisode varie entre 1.3×10^{10} J et 8.8×10^{10} J (moyenne = 4.2×10^{10}) en 2012, et entre 1.9×10^{9} J et 1.2×10^{10} J (moyenne = 5.3×10^{9}) en 2013 (Table 4.1). A Stromboli, la durée des émissions était comprise entre 25 s et 73 s avec une moyenne de 48 s. Le nombre d'explosions détecté par évènements est de 1 ou 2. L'énergie de radiance varie entre 2.1 $\times10^{8}$ J et 6.0 $\times10^{8}$ J avec une moyenne de 3.2×10^{8} J. On observe que même si la durée des évènements à Stromboli est plus longue en moyenne, l'énergie de radiance est plus faible qu'au Mont Etna. Finalement, en minimisant les dimensions, on observe les énergies définirent un chemin 3D vers les plus hautes énergies (i.e., le climax) qui permet de définir les

seuils thermiques qui marquent le début de la phase de transition et à le déclenchement de la fountaine de lave.

Enfin, dans le dernier chapitre, l'étude porte sur l'utilisation d'images haute-résolution acquisent par satellite afin d'observer les éruptions stromboliennes et les phénomènes associés (fontaines et coulées de lave) depuis l'espace. Dans ce cas, quelques pixels sont représentatifs de plusieurs kilomètres de coulées de lave alimentés par la fontaine et les évènements stromboliens. Pour ce faire, je présente un algorithme qui distingue les points chauds d'origine volcanique à partir des pixels saturés dans les images thermiques prises du satellite. Cette identification permet la création d'un algorithme pour extraire les paramètres des coulées de lave et de suivre leur évolution. L'objectif était de fusionner des approches acceptées (et déjà opérationnelles) avec de nouvelles méthodes de traitement d'images, comme le MNWTH et le regroupement intra-classe, pour générer une nouvelle méthode hybride de détection de points chauds d'origine volcanique. Ce dernier projet traitait des coulées de lave provenant des activités stromboliennes et de fontaines de lave, vu depuis l'espace. J'ai utilisé les données de l'AVHRR installé sur le satellite NOAA-19 pour détecter les événements volcaniques du Stromboli et de l'Etna. Les derniers systèmes satellitaires, comme le AVHRR/3, sont capables d'enregistrer les informations thermiques et sont utilisés pour détecter et suivre l'évolution d'évènements. Cependant, ce type de système de détection par satellite était originalement conçu pour les prévisions météorologiques et le suivi de la température de la surface de la mer, de sorte que les canaux thermiques ont des niveaux de saturation assez bas et donc, les pixels sont souvent saturés sur des surfaces à haute température [Harris et al., 1995b]. Plus encore quand l'environnement est chaud (particulièrement durant l'été) et/ou lorsque la surface mesurée est très réfléchissante, des pixels saturés vont apparaitre sur les surfaces ambiantes.

Un phase de “nettoyage” en pré-traitement peut réduire l’impact des pixels saturés, mais les petites surfaces hautement réfléchissantes comme les lacs peuvent avoir les mêmes caractéristiques qu’une coulée de lave dans l’image et, par conséquent, être détectées ainsi. Des masques géographiques provenant du satellite ont été utilisés dans une phase de post-traitement pour contraindre la détection à une fenêtre volcanique et minimiser l’impact des faux positifs. Enfin, j’ai testé mon algorithme sur des données de la Sicile et des îles éoliennes enregistrées en Juillet 2014 lorsque un conduit strombolien sur le flanc extérieur de la Bocca Nuova du mont Etna a nourri une série de coulées de lave. J’ai utilisé deux méthodes, l’approche MNWTH - comme utilisé dans le premier projet car l’objectif était similaire, à savoir détecter des cibles de la taille d’un pixel, et une seconde basée sur la méthode d’Otsu. J’ai aussi modifié les méthodes existantes en définissant des seuils dynamiques pour améliorer la flexibilité de la détection. J’ai comparé les résultats de l’algorithme avec une classification basée sur une détection visuelle effectuée un opérateur. L’algorithme a détecté 283 pixels comme points chauds par rapport à une valeur estimée à 398 par l’humain. Statistiquement, on a un coefficient de similarité de 71 %. Pour les 115 pixels restants, 57 n’ont pas été détectés par l’algorithme en dépit d’une température supérieure à 300 K, et 57 ont été nettoyé par la phase de post-traitement, ceux-ci correspondant aux pixels détectés par l’humain mais à l’extérieur de la fenêtre volcanique définie par l’algorithme. Une fenêtre volcanique plus grande permettrait de réduire ce nombre, mais augmenterait le risque d’accepter des points chauds non-volcanique comme des anomalies réfléchissantes. Mon projet est d’installer cet algorithme au Laboratoire marin de Plymouth pour exécuter en temps quasi-réel sur les données provenant de l’AVHRR de façon à mettre en place un service parallèle à MODVOLC pour surveiller les risques volcaniques en Europe, ainsi que les incendies et les ressources en eau, en utilisant AVHRR comme un complément

à MODIS.

Les annexes précisent les différents équipements utilisés pour l'acquisition de données des algorithmes développés dans cette thèse. Je présente aussi les bases de données statistiques comprenant les paramètres des particules et des évènements stromboliens obtenus par mes algorithmes.

Cette thèse présente plusieurs approches pour détecter et suivre les différentes cibles volcaniques dynamiques en données thermiques. Au délà de la partie algorithmique, ce travail ne fait qu'effleurer la surface des mécanismes de l'activité strombolienne. Les projets ont principalement besoin d'être étendue à une plus grande communauté qui ne doit pas se limiter à la volcanologie et, de fait, devenir plus facilement utilisable. En effet, les problématiques sont similaires dans plusieurs domaines (astronomie, oceanologie) où la télédétection thermique est en plein essor alors que l'analyse de ces données n'est pas totalement automatisée. De telles études aident à démontrer comment le traitement d'image et la télédétection thermique peuvent être utilisés en symbiose pour faire avancer la recherche scientifique.

0

Introduction

In April 2010, the eruption of Eyjafjallajökull (Iceland) threw volcanic ash several kilometres up into the atmosphere, an event which led to air travel disruption across northwest Europe for six days and which included the closure of airspace over many parts of Europe [Gudmundsson et al., 2012; Langman et al, 2012; Petersen et al., 2012]. This recent crisis spotlighted the necessity to parameterise and simulate plume dynamics through emission, dispersion and fall out as to better model, track and forecast cloud motions and locations. This eruption was classified as a Strombolian-to-Sub-Plinian eruption type. Numerous volcanoes from the five continents produce strombolian activity, e.g., Stromboli, Etna, Yasur, and Fuego [exhaustive list for 2002 in Smithsonian Institution, 2005]. Strombolian eruptions are a relatively mild form of explosive volcanic activity [Macdonald, 1972] which can be placed, based on its intensity, magnitude and style, between Hawaiian and Vulcanian eruptions [Newhall and Self, 1982]. Strombolian eruptions are small explosive events, 100s to 1000s of meter in height which occur more frequently than Vulcanian, e.g. Stromboli have an average of 13 eruptions per hour [Harris and Ripepe, 2007a]. They are also notable for the brilliant incandescent parabolic arcs traced by their molten ejecta. Emission of bombs, blocks, lapilli, and minor coarse ash is common during normal explosive activity with eruptive volumes of 10^4 m^3 [Newhall and Self, 1982; Harris et al., 2013a]. However, lava flows [Barberi et al., 1993], and ash-rich eruptions [Patrick, 2007], plus paroxysms that send ash clouds to several kilometers [Ripepe and Harris, 2008], are frequent events as well. Strombolian activity also appears in the waxing and/or waning phases of more powerful eruptions [Vergniolle and Mangan, 2000]. For example, several months of strombolian activity preceded sub-plinian eruptions of Shishaldin (Alaska) in 1999 [Dehn et al., 2002]. Thus, strombolian eruptions are related to, and associated with, a large range of volcanic event types and eruption styles

and offer a partial precursory-indicator of more dangerous, and powerful eruptions. In addition, strombolian eruptions, due to their mild nature, are predictable and small enough to allow observation from within few hundred meters [Chouet et al., 1974; Blackburn et al., 1976] with relative safety, for both operators and material [Ripepe et al., 2004]. On Stromboli, Strombolian activity has been observed and studied over several centuries [Washington, 1917]. Over this period, the constant evolution of technology and the proliferation of monitoring equipment has improved our understanding of conduit dynamics and explosive behavior [see Harris and Ripepe, 2007a and Ripepe et al., 2008 for review].

Active volcanoes emit heat through lava flows, domes, lakes, degassing and erupting vents. Remote measurements of heat emission from such active features provide insights into the physical processes governing the associated volcanic activity [e.g. Francis and Rothery, 1987; Oppenheimer, 1989; Holasek et al., 1996; Harris et al., 1997c; 1997d; Oppenheimer and Francis, 1997; Wooster and Rothery 1997; Oppenheimer, 1998; Dehn et al., 2000]. However, analyses and modelling as well as post-processing of thermal data are still not fully automated, and quantitative parameters to feed to the modelers and responders in near-real time remain difficult to extract and provide.

Since 2001, thermal camera video has been increasingly used to track, parametrize and understand dynamic volcanic events [Harris, 2013], such that the use of such a capability is beginning to eclipse that of the satellite-based perspective [e.g. Dehn et al., 2001; Sahetapy-Engel and Harris, 2009; Spampinato et al., 2011; Vanderkluysen et al., 2012; Valade et al., 2014]. However, the complexity and size of these data sets are compounding the current problem of ever-accelerating data dates so as to require development new and different methodologies. For on-going volcanic events, parameters, such as mass flux, ascent (or spreading) velocity

and plume or lava expansion spreading rate, are key for understanding the dynamics of the explosive and effusive eruptions and the source mechanisms that drive them.

In this thesis, I concentrate on the different components of strombolian eruptions at the full range of remote sensing spatial scales. These range from millimeters (for individual particles in single thermal camera pixels) to kilometers (for the entire features imaged with the satellite field of view). Overall, I aim to characterise volcanic emissions through thermal vision.

The first chapter reviews the state of the art of thermal remote sensing and its use in tracking volcanic activity. In Chapter 2, I present an algorithm to detect, track, and extract parameter for hot vent-leaving particles in high-speed thermal video as recorded at Stromboli. Next, in the chapter 3, I step back and observe volcanic plumes of finer particles and gas during their entire ascent phase. I present an algorithm to automatically segment volcanic plumes, and extract key parameters which can be used to model plume behavior during its ascent and dispersion. Once these coarse strombolian plume components (bombs and lapilli) have been analysed, I move on to a more general angle. Chapter 4 follows the evolution of strombolian activity to lava fountaining to contribute to near-real time radiometer-based surveillance at Mount Etna. My algorithm defines every strombolian event in the build-up to fountaining, and extracts their temporal and energy-based parameters, so as to define the trigger mechanisms for fountaining onset and the transition from milder strombolian events. Finally, in the last chapter, I step back to take a high-spatial resolution satellite-based approach to my investigations so as to fully observe strombolian eruptions and their associated phenomena (fountains and lava flows) from space. In this final case, a few pixels are representative of kilometer-long lava flows fed by fountaining and strombolian events. To achieve this, I

present an algorithm to distinguish real volcanic hot spots from outliers due to saturated pixels in thermal satellite images. This identification allows creation of an algorithm to extract lava flow parameters and to track the event evolution. I specify, in the appendices, the different equipment types used for the acquisition of the data used in the four main algorithms developed in this thesis. I also present statistical data bases produced by these algorithms, including large statistical data bases for particles and event parameters.

Every object in the Universe with a temperature above absolute zero radiates in the infrared, so this part of the spectrum contains a great deal of information

Frank J. Low

1

A Brief History of Thermal Remote Sensing

1.1 Scan of the earth

The term remote sensing was introduced during the 1960s and its definition is "the observation and measurement of an object without touching it" [Curran, 1985]. The oldest remote sensing instrument (after the eye) is the photographic camera. The first fixed image was acquired in 1816 by Nicéphore Niépce, but the invention of the early forms of the camera can be traced to the 1840s. The pioneer, Louis Daguerre, presented his daguerreotype camera to the French Academy of Sciences in 1839, but this balloon-mounted system was rather impractical. However, the ingenious Gaspard Félix Tourhachon (known by the pseudonym Nadar) solved the puzzle by succeeding to keep the camera stable and in autumn 1858 produced the worlds first photographs taken from the air [Soucoup and McCully, 2005]. During the 20th century this method became operational, with surveillance by aerial photography on modified combat aircraft for military and reconnaissance purposes being common during World War I and World War II, to reach a climax during the Cold War. However, since 1960, the development of remote sensing platform and sensor technology has improved drastically and, new methods and technologies for sensing of the Earth's surface have now moved far beyond the traditional black and white aerial photograph. Recent technologies include thermal cameras, lasers, radars, sonars, seismometers and gravimeters mounted on satellites, drones and tripods.

Here, my interested is in ground-based and space-based remote sensing, specifically in the thermal infrared (8 - 14 μm). For the ground-based remote sensing approaches, I deal with two types of instrument designed to measure photons: cameras and radiometers. The difference between the two is that radiometers collect radiant flux for a single point, whereas

an imager records radiant flux for all points, across the image array.

Remote sensing instruments (sensors) that instantaneously measure radiation coming from the entire scene are termed framing systems (Figure 1.1 (a)). They are non scanning devices that capture light almost instantaneously when the shutter is opened and then closed (this is human eye or a photo camera). But when the camera and/or the target moves, as with a movie camera, it is, in a sense, performing scanning as such. One of the most vital aspects of sensor function and performance is the image (or frame) resolution. The resolution of a sensor is the smallest change it can detect in the quantity that it is capable of measuring. For example, the resolution of a camera can be viewed as the smallest object clearly visible with distinct boundaries. The image resolution of digital cameras can be described in many different ways (pixel, spatial, spectral, temporal, and radiometric).

The fundamental principle underlying sensor operation centers on what happens in a critical component - the detector. The detector consists of an array of individual spatial elements that represent a corresponding square, rectangular, or circular area (ground resolution cell) in the scene being imaged. In the sensor, each cell is associated with a pixel (picture element) that is tied to a microelectronic detector. The size of a pixel and the number of pixels per line define the pixel resolution (or pixel density) in pixels per inch (ppi) or pixels per centimer (ppcm). If the number or the size of pixels are unknown, they can be calculated from the spatial resolution. The size of the scene is determined by the aperture and optics of the system that together define the field of view (FOV). The FOV is a solid angle across which a detector is sensitive to electromagnetic radiation, i.e. the extent of the observable world that is seen at any given moment. In remote sensing, the area coverage of the pixel (that is, the ground cell area it corresponds to) is determined by the instantaneous field of view (IFOV,

β_{IFOV}) of the sensor system. IFOV is a function of the optics of the sensor, the sampling rate of the signal, the dimensions of any optical guides (such as optical fibers), the size of the detector, and the altitude above the target or scene. Thus, we can correlate the dimension of the sensor (X_H for the height and X_W for the width) with the angle of the IFOV: $X_H = 2[f \tan(\beta_V/2)]$ and $X_W = 2[f \tan(\beta_h/2)]$. In these equations β_V is the vertical angle of the FOV, β_h is the horizontal angle of the FOV, and f is the focal distance of the sensor. By dividing the size of the image (in pixels) by the dimension of the sensor (in cm), we can obtain the pixel resolution (in ppcm).

The invention of the charge-coupled device (CCD) in 1969 by Willard Boyle and George E. Smith pushed forward the capability of acquisition devices. Then, in 1975, Steven Sasson developed the first camera utilising digital technologies, rather than analog, to capture and store images. A digital camera contains an X-Y array of detectors that discharge photon-induced electrons continuously. This discharge translates into a signal of varying voltage. The discharge is tracked by sampling the detectors systematically. This digital format made it possible to display and analyse imagery using computers, a technology that was also undergoing rapid changes during the 1970s. Computer technology was moving from large mainframe machines to small microcomputers and providing information more in graphic form rather than simply providing numerical output.

The CCD technology approach to sensing electromagnetic radiation (EMR) also led to development of sideways-tracking systems (or "push broom" imagers) (Figure 1.1 (b)). This is regularly used for a passive remote sensing of Earth from space. Sideways-tracking imagers normally involve a one-dimensional (1D) array of detectors, which uses the motion of the aircraft or satellite to move the 1D array across the ground to build up a 2D image over time.

Such systems cannot be used for real-time imaging, and must look perpendicular to the direction of travel.

After World War II, and through the 1950s, the Cold War created a need for the United States to understand the military strength of the Soviet Union (and *vice versa*). Reconnaissance planes could only penetrate the airspace of the country under surveillance and surface-to-air missiles could easily shoot them down. Thus, in 1955, U.S. President Dwigth D. Einsenhower announced that the United States would launch an artificial satellite, and the race to space began. Russia won the first event with the success of Sputnik I (October 1957), however the U.S.A. launched the first orbiting satellite in January 1958. Even if it was not the main purpose of this competition, the development of artificial satellites in the second half of the 20th century allowed global scale radiometry for civilian and scientific applications. After the launch of Sputnik I, placing film cameras on orbiting spacecraft became possible. The first cosmonauts and astronauts used hand-held cameras to document selected regions and targets of opportunity as they orbited the globe. Sensors tuned to obtain black and white TV-like images of Earth flew on meteorological satellites in the 1960s. Other sensors on those satellites made soundings or measurements of atmospheric properties at various heights. The 1960s also witnessed the launch into orbit of the first communications satellites. However, satellite remote sensing matured in the 1970s, when instruments flew on Skylab and on Landsat satellite series, the first satellite dedicated to mapping natural and cultural resources across land and ocean surfaces. Such satellite-based sensor systems were mainly designed and used for global change research, such as weather forecast, ozone layer evolution, deforestation effects, and natural disasters impact; but recent advances provide global measurements for other wide-reaching civilian applications (e.g. web-based mapping and earth surface viewing ser-

vices). A specific, and one of the oldest, cases of a satellite-based system that detects in the thermal infrared is the Advanced Very High Resolution Radiometer (AVHRR, Appendix A.5). AVHRR instruments are a type of space-borne sensor operated by the National Oceanic and Atmospheric Administration (NOAA). On 23 November 1960, the NOAA satellite TIROS-2, carrying an infrared radiometer, was launched from Cape Canaveral marking the beginning of the thermal remote sensing from space. From there-on, an instrument with an infrared capability has been flown on the NOAA-satellites series through today, meaning that we now have more than 50 years of data and experience with this technology and data type. A Low Resolution IR Radiometer (LRIR) recorded between 1966 and 1972, a Very High Resolution Radiometer (VHRR) between 1972 and 1978, and the AVHRR since 1978, thus providing continuous high quality data for hot spot tracking since this time. The dynamic nature of volcanic eruptions benefits from regular collection of thermal data at a high frequency. As a result, workers began to look towards low-spatial-resolution meteorological satellites which, out of necessity, acquire data on an hourly to daily basis. Because no dedicated satellite mission with a primarily volcanological role has been launched, this has dictated the rate of progress in satellite-based volcano monitoring which has been limited by, for example, low gain settings so that data are typically saturated over high temperature active, volcanic targets. Thus, operation of infrared-capable sensors for weather and Earth observation purposes has been fundamental in the evolution of the thermal remote sensing of active volcanism, but has meant that the remote sensing volcanologist has had to work within certain limits.

Radiometer (Figure 1.1 (c)) is a general term for any instrument that quantitatively measures the radiant flux of EMR in some interval of the electromagnetic (EM) spectrum. When the radiation is light received by the detector across a narrow spectral band including the vis-

(a) (b) (c)

Figure 1.1: Main thermal remote sensing instruments: Thermal camera (a), AVHRR satellite (b), and Radiometer (c)

Table 1.1: Abbreviations and limits to the regions of the electromagnetic spectrum within the IR waveband

Division Name	Abbreviation	Wavelength
Visible	VIS	0.4-0.7 μm
Near-infrared	NIR	0.7-1.1 μm
Short-wavelength infrared	SWIR	1.1-3.0 μm
Mid-wavelength infrared	MIR, MWIR	3.0-5.0 μm
Long-wavelength infrared	TIR, LWIR	5.0-20 μm

ible, the term photometer can be substituted for radiometer. This definition spans the full EM spectrum, including wavelengths from 3 Ångströms (X-ray) to 3 km (radio frequencies). Here, I narrow the definition down by being strictly interested in infrared (IR) radiometry, i.e. measurements across the 0.7 μm - 20 μm waveband of the spectrum. Because I am not interested in either the visible (VIS) or the ultra-violet (UV) spectral bands, I will consider the radiometer as an infrared radiation detector. In Table 1.1), following the nomenclature of Schott [2007], I further subdivide the infrared; and this terminology will be used throughout this thesis.

1.2 The nominal red edge of the visible spectrum

Infrared radiation (IR) was discovered by Sir William Herschel in 1800. Using a mercury thermometer as a radiation detector, and splitting the colors of the spectrum using a Newton prism, Herschel tested the heating effect of each portion of the visible spectrum to defined filters for sun spot observations. He found a zone outside the visible portion of the spectrum where heating reached a maximum, i.e., he had discovered thermal infrared radiation. From thereon, the development of thermal detectors was mainly focused on the use of thermometer until the invention of the thermocouple by Seebeck in 1821. Seebeck discovered that when any conductor was subjected to a thermal gradient, it generated a voltage, this became known as the thermoelectric effect or Seebeck effect. Leopoldo Nobili then fabricated the first thermocouple in 1829. Thermocouples can be connected in series to form a thermopile. The output is the sum of the voltages across the individual junctions, giving larger voltage and power output than is possible with a single device. The main advantage of a thermopile is that it covers a broad spectral range (200 nm- 30 μm) and can thus be used for temperature measurement across a wide temperature range (typically - 30 to 1200 °C). Macedonio Melloni, in 1840, showed that a person 10 meters away could be detected with this device. Since then, thermopiles have been used in modern radiometers to detect the presence of icebergs and steamships as patented in 1913, and improved in 1914 following the loss of the Titanic in 1912. Radiometers have also been used to detect forest fires in 1934, with first use in volcanology being 1964 [Decker and Peck, 1967].

The microbolometer forms the basis of most portable thermal imagers (also known as TIC or thermal imaging cameras or thermographic cameras). The forerunner to the mi-

crobolometer was the tasimeter, invented in 1877 by Edison. Composed of compressed carbon, the electrical resistance of the tasimeter varied when heated. Three years later, in 1880, Langley developed a more sensitive instrument, the bolometer, which consisted of a blackened platinum strip which operated on the same principle as the tasimeter, i.e. its electrical resistance varied when heated. Langley's bolometer was able to detect the heat from a cow over a distance of 400 m. Like rocketry, the development of the thermal resistive (bolometric) principle of detecting radiation progressed considerably during World War II, with Luchin designing the first semiconductor bolometer in the USSR, and the superconducting bolometer being invented in the USA. In the late 1970s, Honeywell International Inc. developed the microbolometer technology as part of a classified contract for the US Department of Defense, which declassified the technology in 1992. A microbolometer is a specific type of bolometer used as a detector in a thermal camera. Infrared radiation strikes the detector material, heating it and changing its electrical resistance. Thus, each pixel is characterised for a brief time by some single value of radiation (e.g., spectral radiance) corresponding to this resistance change. Once measured, the resistance change can be converted, by the photoelectric effect, into a number of electrons and can be processed into temperature which can be used to assign each pixel in the image a meaningful value. Unlike other types of infrared detectors, microbolometers do not require cooling which saves time, weight, bulk, and money. Older thermal imagers required a cool down time in excess of 10 minutes before being usable; the first thermal imaging cameras took one hour to produce a single image leading to research to improve the speed and accuracy of the technology.

The first conventional thermal imaging cameras were produced following the development of the first infrared line scanner by Texas Instruments in 1947. Thermographic cameras

produce a thermal image of a scene that provides information about both its temperature and radiative properties, a capability which makes TIC useful for a multitude of thermal feature detection and tracking roles. Thus, in 1956, Texas Instruments took the lead in research and development of infrared technologies.

A military-oriented advance in TIC technology occurred with the development, in the late 1950s, of Infrared Search and Tracking (IRST) systems to improve all-around situation awareness. These sensors react like B-scopes used on early radars, making noise whenever any IR light falls on the detector. Such systems are passive, meaning that they do not give out any radiation of their own, unlike radar and thus signal is difficult to detect. These methods were designed to detect and track objects which give off infrared radiation such as vehicles, ships and aircraft [Yilmaz et al., 2003], and were first developed for air defense applications [Jong, 1995], as well as for other military applications. Thermal emission from gears operating on tanks or helicopters can, for example, be used to detect, track and lock-on to the target, so that many automatic target recognition (ATR) algorithms have been proposed to this end [Li et al., 2001].

Another important evolution was the invention of the first forward looking infrared (FLIR) camera in 1963. This term is used to distinguish these systems from sideways-tracking infrared systems. The first serious application was during the Vietnam War in the 1960s so as to provide gunship crews with night vision. The first IR high-temporal-resolution (operating at 20 Hz) ground-based infrared imaging system, was produced in 1965 and marked the beginning of the mass production of IR cameras for civil applications. The first hand-held system came with the introduction of high-spatial resolution focal plane arrays (FPA) in 1993, and the first uncooled micro-bolometer-based system was produced in 1997. These

developments, coupled with evolutions in high-speed digital electronics that allowed imagery to be stored on small memory disks, "revolutionized the commercialization of thermal imaging systems" [Holst, 2000]. From this time onwards, IR imaging science expanded rapidly in many domains [Kylili et al., 2014]. TIC civilian applications include fire control [Amon and Pearson, 2009], buildings monitoring [Kylili et al., 2014], medicine [Arora et al., 2008], computer-aided diagnosis systems [Faust et al., 2014], surveillance [Caballero et al., 2001] and volcanology [Harris, 2013].

1.3 On the Volcanology's Remote Service

1.3.1 A View to a Volcano

In this section, I focus on two groups of ground-based volcanological applications, the first includes work carried out using radiometers; the second examines applications of thermal cameras.

The work of Macdonald [1963] (as updated by Harris, [2013]) reported most known temperature measurements at active volcanic systems for the period of 1900 to 1966. From these reviews we can trace the first temperature measurement to the study of a lava flow on Stromboli (Italy) as made by Brun in 1901 using a thermocouple in direct contact. Then, in 1909, Daly completed the first non-contact measurement at Kilauea (Hawaii), using a pyrometer to obtain temperatures across the surface of Halemaumau's active lava lake. One of the first field-based thermal measurement campaigns at an active volcano was completed by Thomas A. Jaggar [1917a; 1917b]. He illustrated the benefits of remote thermal measurements against the common contact measurements, describing problems including equipment and personnel safety as well as the limited measurement time available for a contact measurement im-

posed by the radiated heat from a lava lake. The first ground-based used of a radiometer was reported by Decker and Peck [1967]. They obtained a surface temperature profile across the cooling lava lake within Kilauea's Alae crater during 1964. The first attempt to run a radiometer continuously at a volcanic target was completed for a persistent degassing vent by Tazieff [1970], logging the thermal signals generated by hot gas exiting an active vent on Mt. Etna in 1969. Shimozuru [1971] presented thermal waveforms acquired using continuously logging radiometers targeted at explosions from Akita-komaga-take (Japan) in 1970. Between 1965 and the end of 2007, at least 60 studies reported results obtained using ground-based radiometers for explosions, fumaroles and geothermally heated surfaces as well as lava flows, lakes and domes [Harris, 2013].

Shimozuru and Kagiyama [1978], completed one of the first deployments of an "infrared camera" to provide ground-based infrared surveys after eruptive episodes at the Japanese volcanoes of Kusatsu-shirane and Mihara-yama in 1976. In fact, the camera was a broad-band (8-12.5 μm) bolometer-based radiometer attached to a scanning device. Most of the thermal cameras used in volcanology until 1981 were scanning systems [Yuhara et al., 1981; Ballestracci and Nougier, 1984]. This changed with the publication of USGS volcanological reports that included information from uncalibrated thermal camera video to track surface temperature prior to, and after, the 18 May 1980 eruption of Mount St. Helens (USA).

The declassification of the microbolometer allowed the first uncooled microbolometer-based thermal camera to go on-line in 1997. McGimsey et al. [1999] was one of the first to use it to record eruptive activity at Pavlov and Shishaldin volcanoes during their 1997 and 1999 eruptives phases. However, the publication of eight papers reporting applications of camera systems based on FPAs of uncooled micro-bolometers in 2002 may define this year as

the entry of the hand-held thermal camera into the volcanological literature [Harris, 2013]. These applications to volcanological science by thermal cameras were clustered in five main groups by Spampinato et al. [2011], these being studies of

1. hydrothermal areas and fumarole fields;
2. lava bodies;
3. explosive activity and volcanic plumes;
4. pyroclastic flow deposits;
5. fracturing and cracking.

The most popular of these applications has been analysis of explosive activity, which accounted for 48 % of the studies published between 2001 and 2011 [Harris, 2013]. In fact, some of the first publications involving the application of thermal camera data in the domain of volcanology focused on the dynamics of explosive eruption plumes [Dehn et al., 2001]. The key advance in generating this popularity in volcanic studies has been the ability to collect thermal video with spatial resolutions of a few centimeters and sampling frequencies of up to 120 Hz, with the operator being free to choose and modify the dynamic range, sampling rate, field of view, and targeted area, as well as acquisition start and stop times. In fact, the technology was accepted immediately as a valid surveillance and monitoring tool. Thus, four years after the take-off studies of 2002, Ball and Pinkerton [2006] and Sawyer and Burton [2006] tested the performance of the FLIR-systems cameras and the effects of volcanic gas on hand-held thermal camera measurements.

However, the ground-based acquisition imposes several safety and logistic limits; personnel and hardware have to be in a safe area to record. As a result, permanent, low cost and unmanned systems have been set up at several volcanoes (see Harris [2013] for review). These transmit data back to an observatory site, where a degree of automated processing is required.

1.3.2 The Ground is Not Enough

The first paper describing satellite observations of active volcanism was published by Gawarecki et al. [1965], five years after the launch of the first infrared satellite, TIROS-2. This paper reported the detection of thermal anomalies in infrared data collected over an active lava flow field. Then, Williams and Friedman [1970] published the results from an analysis of infrared data for the 1966 eruption of Surtsey (Vestmannaeyjar, Iceland). Their work defined the basic utility of satellite data for analysis of volcanic hot spots, this being both the detection of the hot spot and the constraint of its heat flux. This was the beginning of satellite remote sensing of active volcanism. Since 1970, more than 100 scientific papers have been published about the examination of volcanic hot spots associated with active lava flows, lava domes, lava lakes, active vents, fumaroles and crater lakes [Harris, 2013]. One of the main data sources for satellite-based thermal studies of volcanic hot spots has been data from the AVHRR. Between 1960 and 2005, NOAA launched 34 satellites in this series. These data allowed 39 % of the main satellite-based studies between 1965 and 2005 [Harris, 2013]. Although the AVHRR sensor was not designed with the detection and measurement of volcanic hot spots in mind, it provided SWIR, MIR and/or TIR data that could be used for such an application. The first publication dealing with AVHRR data for a volcanic hot spot occurred in 1982. Wiesnet and D'Aguanno [1982], who focused on an active lava lake at

Mt. Erebus (Antarctica), were followed by Bonneville et al. [1985], Scorer [1986], and Bonneville and Kerr [1987] who all published studies that used AVHRR data for Mount Etna (Italy). Later, Rothery et al. [1988] explored the likely sources of error in making satellite-based measurements of volcanic thermal phenomena, including a consideration of pixel size, the point spread function, atmospheric effects, and re-sampling problems resulting from geometric rectification. Most importantly, Rothery et al. [1988] defined the basis of a major theme in satellite-based high-spatial-resolution thermal analysis: the dual-band methodology - as introduced by Dozier [1981] for industrial and fire applications - which allowed estimation of the size and temperature of a sub-pixel heat source. Further applications of the dual-band method have been developed to deal with lava flow heat loss estimations [Oppenheimer, 1991] and time series analysis of active lava domes [Oppenheimer, 1993]. By the end of the 1990's a total of 38 papers had been written presenting use application of the dual-band method to satellite IR data containing volcano hot spots [Harris, 2013]. At the same time, the first "real-time" volcano monitoring was setup by the remote sensing group at the University of Alaska Fairbanks, UAF [Dean et al., 1998]. The main aim was detection and tracking of ash clouds emitted by explosive eruptions and assessing the hazard these posed to air traffic. Mostly using AVHRR data, UAF provided activity level information for over 100 volcanoes, many of which were un-observed from the ground. The need to deal on a 24 hour basis with satellite data for volcano hot spots detection resulted in a major research efforts at UAF [Wyatt and Dean, 1995; Dean et al., 1996; Schneider et al., 2000; Roach et al., 2001; Dehn et al., 2000;2002 and Dean et al., 2002;2004] culminating with the development of an AVHRR-based hot spot detection algorithm (OKMOK).

According to Harris [2013], most of the major advancements in use of satellite data for

analysis of volcanic activity occurred during the 1990s. However, the advances in reception, computing, processing and storage capacity made in the 2000s were the revolution needed to push forward satellite remote sensing of active volcanism, as well as ground-based camera and radiometer driven applications.

When they were a good way out to sea, Odysseus could not resist a taunt. He called out, and Polyphemus came to the edge of the seaside cliff. In his fury he tore up a huge boulder and flung it at the ships.

The Odyssey, Book IX - Homer

2

Strombolian Ballistics

2.1 Particle-size Study

2.1.1 Target

Stromboli volcano (Aeolian Islands, Italy) was selected as a target, it being a reliable emitter of particles where mildly explosive activity has persisted at-leasted since 500 AD [Rosi et al., 2000]. Currently, activity is characterised by emissions of gas, bomb, lapilli and ash mixtures [Patrick et al., 2007; Gurioli et al., 2013; Leduc et al., 2014]. In addition, eruptions occur (on average) at a rate of 13 eruptions an hour [Harris and Ripepe, 2007a; Ripepe et al., 2008] and are sufficiently small that measurements can be made, and methodologies tested, close to the source in reasonable safety. Stromboli has thus become famous as being an outstanding natural laboratory for studying the source and dynamics of explosive emissions. Because measurement of particle exit parameters is an important objective in the study of explosive emissions, studies aimed at designing methodologies to extract parameters, and to create particle size, mass, and velocity databases, have tended to target Stromboli [Chouet et al., 1974; Ripepe et al., 1993; Patrick et al., 2007; Delle Donne and Ripepe, 2012; Harris et al., 2012, 2013b; Taddeucci et al., 2012a]. Recently, technological advances including the development of field portable high speed visible and thermal cameras, have allowed new insights into particle emission dynamics and how those dynamics relate to associated source processes [Patrick et al., 2007; Taddeucci et al., 2012a; Harris et al., 2012; Gurioli et al. 2013, 2014; Genco et al., 2014]. For example, Patrick et al. [2007] classified normal explosions at Stromboli into two groups: Type 1 eruptions, which are dominated by coarse ballistic particles, and Type 2 eruptions, which are ash dominated with (2a) or without (2b) large numbers of pyroclastic particles demonstrating that there are at least two distinct populations of Strombolian erup-

tion highly dependant on its geophysical components. A fundamental result of this work, however, based upon analysis of the thermal imagery, is that strombolian particle behavior is still poorly understood; despite the frequency of activity and number of particles involved in each emission at Stromboli, large, statistically robust databases for vent-leaving particle dynamics remain scarce. Here, we provide insights into plume emission and ascent dynamics which shed light on the source mechanism. Indeed, measuring parameters of all particles as they exit the vent during an explosive eruption is the best way to gather parameters such as size, shape, velocity and mass for the solid (particulate) fraction of the plume.

Particle size distribution has long been known to be a particularly useful parameter to measure if we are to understand the fragmentation process and particle emission dynamics [e.g., Walker, 1971, 1973; Wohletz et al., 1989]. These data can be obtained from the deposit or from visible and infrared imagery of an active eruption [e.g., Chouet et al., 1974; Ripepe et al., 1993; Harris et al., 2012]. Likewise, individual particle and total deposit mass has increasingly been obtained from thermal camera imagery [Patrick et al., 2007; Taddeucci et al., 2012b; Delle Donne and Ripepe, 2012; Harris et al., 2013a]. Mass and mass flux are again fundamental parameters for understanding the dynamic evolution of an explosive event, as well as for event classification and characterisation in terms of magnitude and intensity [Newhall and Self, 1982]. Emission, or launch, velocity is a key parameter for constraining particle trajectories and fall out range [e.g., Lorenz, 1970; Self et al., 1980; Kilgour et al., 2010]. Initially, particle velocities were obtained using photoballistic analysis of visible imagery [Chouet et al., 1974; Blackburn et al., 1976; Ripepe et al., 1993], but thermal camera imagery is becoming increasingly used [Patrick et al., 2007; Harris et al., 2012; Delle Donne and Ripepe, 2012] along with videos from high-speed visible cameras [Taddeucci et al., 2012a; Gaudin et al.,

2014a, 2014b; Genco et al., 2014]. The use of portable (handheld) forward looking infrared (FLIR) cameras has become widespread in volcanology since their first use by McGimsey et al. [1999] to image warm deposits at Pavlof and Shishaldin volcanoes between 1997 and 1999 [Harris, 2013]. Thermal infrared imagery collected at wavelengths of 7–14 μm is able to achieve a number of tasks difficult or impossible to accomplish using other tools. The main advantage offered by the infrared camera is that the hot particles are easily spotted due to their high contrast when set against a cool background. In addition, small (subpixel) hot particles, invisible to the naked eye, become apparent due to their lighting up of a whole pixel [Harris et al., 2012].

The thermal camera used in this study was a FLIR manufactured by FLIR Systems [*], this being the SC655 which acquires 640 × 480 pixel images at 7.5-13 μm (Appendix A.1). The camera was equipped with a 3.6× magnification lens (Appendix A.2) and recorded at 200 frames per second. In order to allow data transfer at these frame rates, the image height is automatically reduced to 120 pixels. The focal length of the lens (f) was 88.9 mm and the pixel spatial resolution (IFOV) was 0.19 mrad.

We completed two measurements campaigns, one in 2012 and a second in 2014. In 2012 we completed eight hours of recording spread over four days spanning 27 September to 5 October 2012 during which we recorded 13 eruptions. In 2014 we recorded eight hours on 17 and 18 May, capturing a further 18 eruptions. We set up the thermal camera at Pizzo Sopra la Fossa (PSF: 918 m above sea level) which overlooks Stromboli's active crater terrace. The terrace itself is aligned NE-SW with dimensions of 200 by 230 m and contains all of the active vents (Figure 2.1). In historical times, the crater terrace has hosted three main craters [Washing-

[*] www.flir.com

ton, 1917], which today are named South-West (SWC), Central (CC) and North-East (NEC). During 2012, SWC hosted two active vents, two puffing vents were active atop a small cone in CC, and NEC also contained two active vents. In 2014, SWC contained three active vents, plus four degassing vents. CC comprised a large central cone, whose summit vent produced near continuous spattering and explosions, and NEC comprised two pits each containing an active vent. We set up on the SW end of PSF (UTM coordinates: WGS84 0518574 4293754) from where we viewed the most active vent in SWC over a line-of-sight distance of 280 m. We also set up on the NE end of PSF (UTM coordinates: WGS84 0518580 4293785) from where we were also able to record data for an active vent in NEC over a distance of 250 m. All 13 eruptions recorded during 2012 were from SWC, with 13 eruptions being recorded from SWC in 2014 and five from NEC. Each event is referenced using 4 digits for the month and day (MMDD), then nine digits for the time (in hour, minutes, seconds and nanoseconds) from the beginning of the video clip from which the data sequence is extracted (HHMMSSNNN). During the 2012 campaign, a Guralp CMG-40T 30-second broadband seismometer was also installed near the thermal camera acquisition point.

Figure 2.1: Stromboli's active crater terrace viewed from Pizzo Sopra la Fossa.

In this study, we are not interested in trajectories [Vanderkluysen et al., 2012]. Here we use thermal video data to fully parameterise the emission dynamics of bombs, blocks, and lapilli. Our aim is to capture the vent leaving properties, as close to the point of fragmentation as possible, of all measurable particles, primarily size, shape and mass. Such parameters collected later along the flight path, or once the particle is on the ground, will be very different and heavily modified as compared with those that were actually present as the particles exited the vent. For instance, a molten ejecta may deform and fragment in flight as well as upon ground impact. This, for example, will change the field collected shape and size parameters. Thus, by computing particle parameters as soon as they exit the vent, our results are valid for the vent leaving conditions. Because of our frame rate (200 Hz), this allows generation of frequency distributions with thousands of points for each eruption, even if the emission lasts just a few seconds. We use these results to further develop the source mechanism and emission model for ballistic-dominated explosive events at Stromboli proposed by Gurioli et al. [2014]. However, given (i) the large number of particles (tens of thousands, Chouet et al., 1974), (ii) high particle velocities [Taddeucci et al., 2012a] and (iii) the quantity of data (two hundred 640×120 pixel images per second, 150 kB in size, every second or 1.8 GB per minute) we need a simple and efficient algorithm to allow parameter extraction. Here, we present an algorithm based on a mathematical morphology transformation hybridised with a refinement by thresholding [Bombrun et al., 2014].

2.1.2 Algorithm Presentation

Segmentation

Thermal infrared imagery is particularly useful because the thermal contrast between small hot targets and a cold background means that they can easily be seen (or detected) when they may be invisible to the naked eyes, thus providing information which is not available in visible images. However, the low signal-to-noise and fuzzy target boundaries increase the difficulty of using thermal infrared (IR) video for IR Search and Tracking (IRST) systems [Mahulikar et al., 2007]. Indeed, IR images are usually characterised by a complex background which has a low contrast with the target. This problem becomes worse for targets imaged over greater distances. In these cases, the small hot target will appear as a dim point moving fast across, and blending in and out, of a heavily cluttered background. To improve target detection, a pre- or post-processing method is essential. The main challenge was to deal with the background problem. To help address this issue, the background can be divided into "static background", which corresponds to an image acquired before the event that generated the target, and a "variation background" or "dynamic background" [Zhong and Sclaroff, 2003], which is the moving part of the video that we do not want to detect (e.g., clouds or bids, in the specific case of volcanic eruptions). The static background can usually be removed through application of different approaches as reviewed in Brutzer et al., [2011]. The most commonly used method is background subtraction, which consists of detecting the moving objects from the difference between the current frame and a reference frame, called the 'background image' [Piccardi, 2004]. It is a really fast process which requires only a background image. However, since we are not able to forecast eruption, raw sequences

are essentially composed of frames anterior to the event. Thus, the easiest and fastest way to remove the background image (regard at time $t = 0$) is to consider the difference between the current frame I_t and the background image, i.e. the initial frame I_0. In the same way, the variation background can be removed by subtracting the previous frame I_{t-1} from the current frame I_t. Because these two effects are not independent, we use a weighted differentiation scheme to model both the static and variation backgrounds. Thus, given m frames and $T_0 = \varnothing$

$$T_t = I_t - \frac{\alpha I_{t-1} + \gamma I_0}{\alpha + \gamma} \; \forall \, t \in \{1, m\} \tag{2.1}$$

where T_t is the differentiated image at time t, and α and γ are weights found empirically which change according to the predominance of the static versus dynamic background.

In parallel with the first step, a working area mask is defined. This corresponds to the elements which were not present in the initial frame, and therefore were present in the variation background. Thus, if a global threshold th is applied based on the difference between I_t and I_0, a mask $\mathcal{M}_t$ can be obtained:

$$\mathcal{M}_t = \mathbf{1}_{\{I_t - I_0 \geq th\}} \tag{2.2}$$

Since this step is to accelerate the computation, the value of the threshold th is chosen to not be strict but in contrary to remove only parts which are not part of the event. The image to be processed (F_t) may then be defined as the Hadamard product (or entrywise product) $F_t = T_t \cdot \mathcal{M}_t$. In the image, only the foreground and a low intensity hint of the background persist. Since we only want to compute the major connected components among the brightest features, which correspond to the targets, we process F_t using a New White Top-Hat trans-

form [Bai and Zhou, 2010]:

$$MNWTH(f) = f - min\left\{\left[(f \oplus \Delta B) \ominus B_b\right], f\right\} \tag{2.3}$$

where $\oplus$ is the dilation operator and $\ominus$ the erosion. Parameters ΔB and B_b are both square-shaped structuring elements. We apply a 21 pixel diameter box with, following [Bai and Zhou, 2010], a three-pixel wide perimeter for ΔB. That is, pixels in the central 15-pixel-wide box have values of zero, and the three-pixel-wide perimeter has values of one. From an explosive

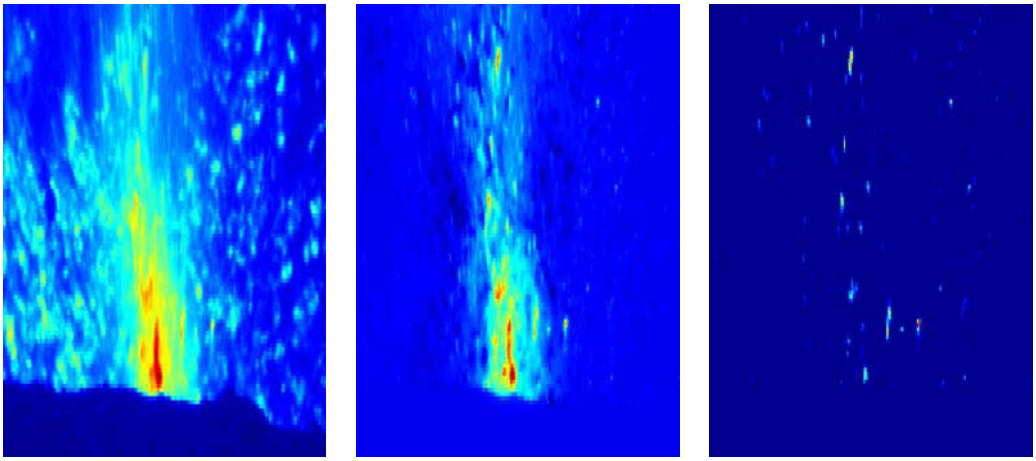

(a) (b) (c)

Figure 2.2: Segmentation of particles. The processus of segmentation started with the original image (a), which is subtracted from the original image (b). The morpho-math method provided us an image of the segmented particles (c)

eruption sequence (Figure 2.2 (a)), and using the background subtraction method (Figure 2.2 (b)), we are now able to get a segmented image of the particles (Figure 2.2 (c)).

Tracking

Once targets have been detected in each frame, they can be tracked to predict the trajectory and the velocity of a particle through time. We considered the maximum intensity pixel (p) of a particle (i) as the reference position at time t. We note $\omega_{p,i,t} = (x_{p,i,t}, y_{p,i,t})$, this reference position. For any particle i, at any time t, we determined it with a sub-pixel accuracy following Shindler et al., [2010]:

$$x_o = x_p + \frac{\ln(I(x_p - 1, y_p)) - \ln(I(x_p + 1, y_p))}{2(\ln(I(x_p - 1, y_p)) + \ln(I(x_p + 1, y_p))) - 4\ln(I(x_p, y_p))} \tag{2.4}$$

The y-coordinate, y_o, can be defined analogously. Hereinafter, we consider the sub-pixel accuracy for the position of the particles, i.e. $\omega_{p,i,t} \equiv \omega_{o,i,t} \equiv \omega_{i,t} \equiv \omega(x_{i,t}, y_{i,t})$. We note N_t, the number of particles detected at time t ; thus, given the position of all particles at time t ($\omega_{i,t}\ \forall i \in \{1, N_t\}$) and the velocity $U_{i,t-1}$, of the particle i at time $t-1$, an estimated position ($\omega^\star_{i,t+1}$) of the particle i at time $t+1$ can be predicted with $\omega^\star_{i,t+1} = \omega_{i,t} + U_{i,t-1}$. The algorithm then matches the predicted position ($\omega^\star_{i,t+1}$) with one of the known position ($\omega_{i,t+1}$) under several conditions:

- Particles have to be closed to the predicted position. In a short period of time, the acceleration should not change significantly and thus, the predicted position will be closed to the exact position, in fact, we minimised the Euclidean distance between $\omega^\star_{i,t+1}$ and the N_{t+1} particles:

$$\min_k \|\omega^\star_{i,t+1} - \omega_{k,t+1}\|\ \forall\ k \in \{1, N_{t+1}\} \tag{2.5}$$

This hypothesis has to be taken lightly since the initial velocity is unknown. We used an initial velocity of zero for the estimation which can preclude the tracking of very fast particles described in Taddeucci et al., [2012a].

- Particles stay at the same gray level trough time. In a short period, even if we are considering an object which is cooling, the temperature recorded between two frames separated by two-hundredths of a second should not change much. Thus we searched for a particle which has minimal differences between the intensity of the previous position and the intensity of all potential positions, so a new constraint is added:

$$\min_{k} \|I(\omega_{k,t+1}) - I(\omega_{i,t})\| \; \forall \; k \in \{1, N_{t+1}\} \tag{2.6}$$

Thus, $\omega_{i,t+1}$ is solution of a linear function which is minimised subject to conditions (2.5) and (2.6). Two more hypotheses help to reduce the number of false detection during the tracking process.

- We considered that objects are moving in one direction. Particles may be moving up (ascending) or down (descending), but we are only interested in the ascending particles. This problem does not arise immediately, but particles fall back down later in the event to follow descending paths. Thus, we considered for an acceptable position, $\omega_{i,t+1}$ only $\omega(x_{i,t+1}, y_{i,t+1} < y_{i,t})$ for an ascending event, and $\omega(x_{i,t+1}, y_{i,t+1} > y_{i,t})$ for a descending event.

- During the differentiation process a tail appeared behind each particle. This phenomenon could be used to track particles. Because this tail is a residual of the previous position, it appears during the differentiation process that the position $\omega_{i,t}$ is composed of a neg-

ative intensity pixels in the frame $t + 1$. Finding only positive gray level value in the neighborhood of this position allows us to eliminate false detections and moreover, negative values point out the trajectory of our target.

Hypotheses on the shape and the number of pixels which composed the particles have been explored. However, particles are rotating on several axes making these hypotheses unsuitable.

2.1.3 Parameter computation

Acquisitions of volcanic videos are subject to the direct environment. Our videos were taken from uneven surfaces from an oblique vantage point. This raises geometric issues which have to be considered for the calculation of pixel dimensions within the image field of view [Harris, 2013]. To extract quantitative information for each particle, we need to express the pixel dimensions (height or width noted X) in millimeters (X_{mm}). The conversion to millimeters is done using:

$$X_{mm} = \frac{Rd}{f\sin(90 - \varphi)} X_{pix} \tag{2.7}$$

where R is the spatial resolution of the camera sensor, i.e. the size of one pixel, d is the distance between the camera and the target, f is the focal length, φ is the tilt angle of the camera during the acquisition (Figure 2.3). Although the tilt angle can mathematically be 90°, such a condition is never approached in reality, see Figure 2.3. Moreover in this figure, the geometry of the schematic in the dashed square allows us to compute the sensor resolution:

$$R = \frac{X_{sensor}}{X_{screen}} \tag{2.8}$$

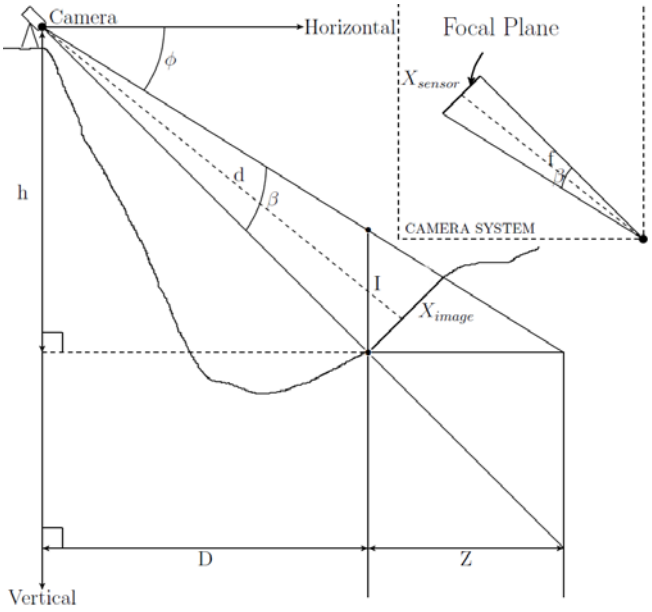

Figure 2.3: Image Geometry: h is the height of the camera, D, the horizontal distance, Z and I, respectively the horizontal and vertical projection

where $X_{sensor} = f\tan\beta$ is the size of one dimension of the sensor, X_{screen} is the size of the image (480 for the height, 640 for the width) and β is the angle of the detector field of view (18.8° for the height, 25° for the width). We remark that the resolution is identical for the height and the width which is consistent with square shapes of common sensors. Finally, we consider:

$$Y = \frac{Rd}{f\sin(90 - \varphi)} \tag{2.9}$$

such as, $X_{mm} = YX_{pix}$.

The segmentation part of our algorithm provides the dimensions of the particle in the image plane. To characterise particle dimension, we considered the radius of the short axis (r_S) and the radius of the long axis (r_L). Using these measurements we defined the characteristic radius (r) using the two axes, so that $r = (r_S + r_L)/2$. To convert to particle volume

we applied a spheroidal assumption that used the short and long axis radii to estimate the volume of particle i (V_i). Particles that are fluid and, at the vent, moving at high velocity in a quasi-vertical direction, tend to take on an elongate shape stretched in the direction of flight [Macdonald, 1972]. This can be best described by a prolate spheroid, so that:

$$V_i = \frac{4}{3}\pi r_S^2 r_L \tag{2.10}$$

To define an appropriate density conversion, we plotted density versus b-axis length for all lapilli and bombs collected at Stromboli between 2008 and 2011 (Figure 2.4). This plot combined measurements from samples of fine (1-2 cm) and large (4-5 cm) lapilli collected during June 2008 from two bomb-dominated normal explosions [Colò, 2012], plus 53 bombs taken from a bomb field of a major explosion in January 2010 by Gurioli et al., [2013]. We also plotted the density of two bombs collected, in 2008 [Gurioli et al., 2014], from a bomb-dominated normal explosion whose particle trajectories were defined by Vanderkluysen et al. [2012], plus two bombs collected from a gas-dominated explosion in 2011 [Leduc et al., 2014]. For the density conversion, we split the distribution into two fields: lapilli and bombs. For the bombs (6.5 cm to 35 cm), we see no real trend with increasing size, but the cluster is fairly tight with a mean and standard deviation of 1800 $\pm$ 200 kg/m^3. Likewise the lapilli field (0.2 cm to 6.5 cm) forms a cluster with a mean and standard deviation of 980 $\pm$ 110 kg/m^3. We used these two values for our size-dependent conversion to mass. Thus, the mass of all particles detected is calculated with an error $\pm$ 11 % due to the uncertainty in density. Now, given this appropriate density, particle volume can be converted to mass (m_i):

$$m_i = \varrho_i V_i \tag{2.11}$$

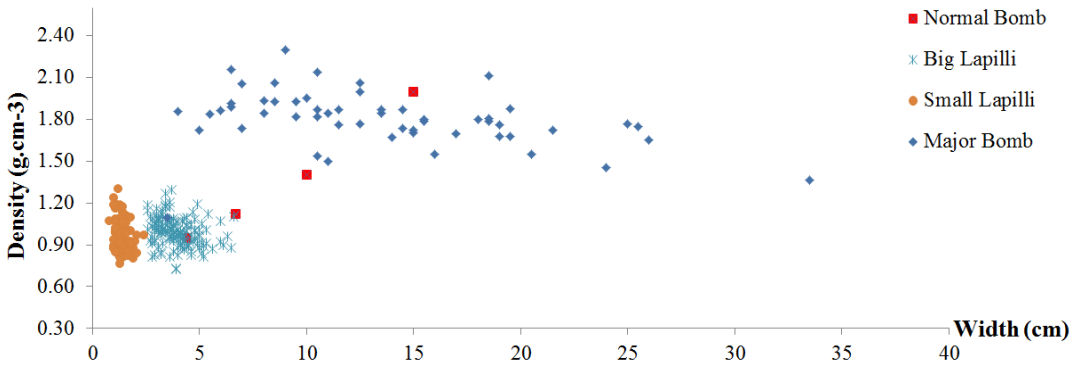

Figure 2.4: Correlation between the particle size and density from sample data for Stromboli's scoria.

The tracking step of the algorithm computed the velocity of particles following first detection [Bombrun et al.,2014]. In raw form this is expressed in terms of the number of pixels travelled by the particle between two consecutive frames, separated by time t. This will be in units of pixels per frame. Thus the pixel velocity (U) of the particle i at time t is:

$$U_{i,t} = \frac{\|\omega_{i,t+1} - \omega_{i,t}\|}{(t+1) - t}; \tag{2.12}$$

We now complete the transition to the estimation of the real velocity in m/s using $U_{m/s} = \nu Y \times U_{pix/fr} \times 10^{-3}$, in which ν is the frequency of image acquisition (200 Hz in our case) and Y is the scale factor defined in Equation 2.9. Particle locations are accurate to within one pixel, leading to absolute uncertainties on velocity of $\pm$ 0.2 m/s (for particles traveling vertically) which can lead to an uncertainty of $\pm$ 2 m/s in the worst case of a particle moving away from the focal plane at an angle of 6°.The particle database for each eruption can thus be used to produce particle size, mass and velocity distributions.

Now that we have particle velocity (U_i) and mass (m_i), we can estimate the particle kinetic

energy (ε_i):

$$\varepsilon_i = \frac{1}{2} m_i U_i^2 \tag{2.13}$$

We can finally produce distributions for each parameter and integrate each parameter through time to obtain volumes, masses and energies released over given periods of time and thus a global vision of the eruption dynamics. To do this, let K={m, V, ε}, so that:

$$K_t = \sum_i K_i \tag{2.14}$$

where K_t is the global parameter {m, V, ε} for all particles. If integrated over the entire emission, this will yield total volume, mass or kinetic energy. If integrated over discrete time steps, and divided by time step duration, this will give volume or mass flux. Thus, we extracted characteristic parameters of thousands of particles.

2.1.4 High-speed limits

Given the high-frame rate acquisition expected from the system, our objective was to record at up to 200 Hz. At his speed, we should be able to detect the high-speed particles which going up to 400 m/s [Taddeucci et al., 2012a]. However, the detector material sets a limit. The focal plane array (FPA) of the FLIR camera is composed of microbolometers. Infrared radiation in the wavelength range 7 to 14 µm strikes the detector material, heating it, and thus changing its electrical resistance. The time required for the detector to change temperature is called the response time. This corresponds to the elapsed time between an input step, and the moment when the output becomes 95 % of its final value [Butterworth, 1968]. This is reached after a time approximately thrice the thermal constant τ_{th} of the bolometer. A

common time constant for a bolometer is 8 ms [Budzier et al., 2006], (see Appendix A.1), so the expected response time is 24 ms. However, image acquisition at 200 Hz corresponds to a cycle duration of 5 ms (Figure 2.5), and a time constant of 0.8 ms. Thus, in this case, the time constant of the bolometer is ten times too slow. As a result, an inertia effect is created forming a tail that extended behind particles, marking the line of their trajectory. In effect, we have oversampled, in a temporal respect, in regard to the response time; the tail shows the position of the particle at the previous time. However, even if this artifact is displayed on individual

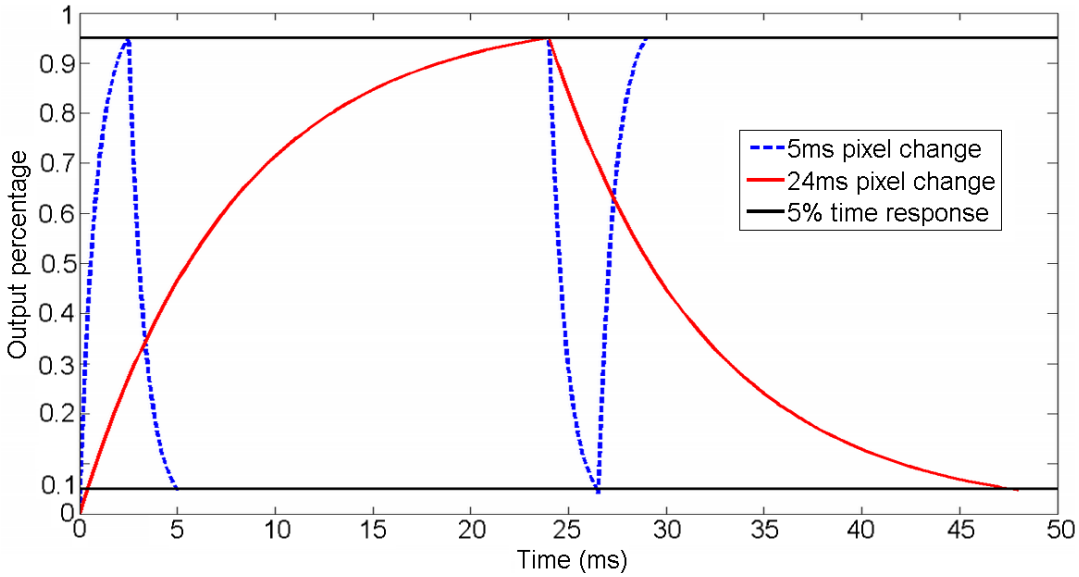

Figure 2.5: Heating and Cooling of a bolometer

images, we make sure through controlled experiment that our algorithm compensates for it (Figure 2.6).

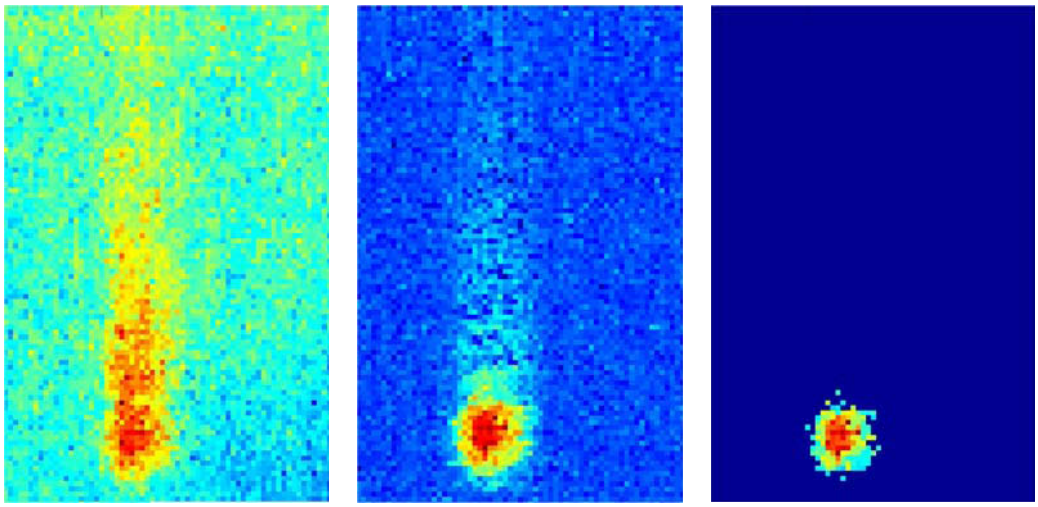

(a) (b) (c)

Figure 2.6: Removal of the tail artifact (a). The subtraction weaken the intensity (b), allowing the threshold to removed it (c)

2.1.5 Controlled experiment

We setup an artificial experiment carried out using a population of particles of known size to test our method. Three hundred steel balls usually used in ball bearings with a density of 7 790 kg/m^3 were used. We first boiled the ball bearings in water and then launched them vertically in front of the thermal camera, which was positioned horizontally (φ=0) at 4.8 m from the launch area. Background was at room temperature. For this test, parameters such as particle density, size, distribution, volume and mass were known so that they could be compared with the algorithm output. This allowed generation of a database using twelve videos of less than five seconds in duration. For each sequence, 30 ball bearings (3 sizes, 10 balls for each range) were launched in a first time, then dropped to reduced motion toward or away from the camera. Launches were carried out with particles of 6 mm, 8 mm, 10 mm, 12 mm, 14 mm, 17 mm and 20 mm in diameter for a total of 255 detections in 304 launches. The percent-

Table 2.1: Comparison of our results S_1 and the real size S_2 with the Bland-Altman test. No.d and No.l are the number of particles detected and launched respectively. For each size, m is the mean and σ is the standard deviation of the difference $(S_1 - S_2)$ while p is the percentage of points beyond the interval $[m - 2\sigma, m + 2\sigma]$

Sample parameters				Statistics for particle size (mm)				
Size (mm)	No.d	No.l	% detected	m	σ	p (%)	m-2σ	m+2σ
6	52	70	74	-1.8	1.8	7.7	-5.4	1.7
8	51	66	77	0.3	2.6	3.9	-4.8	5.5
10	37	40	92	-0.5	2.2	8.1	-5.0	3.9
12	23	25	92	-0.7	1.4	4.3	-3.6	2.1
14	24	30	80	-0.6	3.5	8.3	-7.5	6.3
17	42	43	98	-0.5	5.1	7.1	-11	9.7
20	26	30	77	-2.8	2.3	0.0	-7.4	1.9
All	255	304	84	-0.9	3.1	5.1	-7.1	5.3

age of particles successfully detected varies with size and is detailed in Table 2.1. Because our background was homogeneous, the impact of the static background is insignificant. Thus, we set the parameters for the background subtraction (Equation 2.1) to $\alpha = 1$ and $\gamma = 0$. The value of the threshold used in Equation 2.2 was $th = \mathcal{M} - \sigma$, where $\mathcal{M}$ was the mean of the intensity of the image and σ was the standard deviation of the differentiated image. The difference between the actual particle dimensions and those returned by our algorithm under experimental conditions is given in Figure 2.7. Some unexpected results were observed. They result from two causes. First, even if launches were carried out as vertically as possible, some ejecta moved towards, or away from, the camera, thus changing size in terms of pixel dimension (i.e. for a particle moving away from the camera, the effective spatial resolution will decrease, so that the particle apparent size will also decrease). Because we were only able to process results in the image plane, these ejecta suffered from a scaling factor problem; which is a limit. The other one is the cooling time of the ball bearings. The smaller the particle, the faster it will cool, so that small particles quickly become difficult to distinguish from the back-

ground by the area computation part of the algorithm. Thus, tests that were completed with smaller targets (4 mm) were not conclusive (one in twenty detected). To ensure the quality

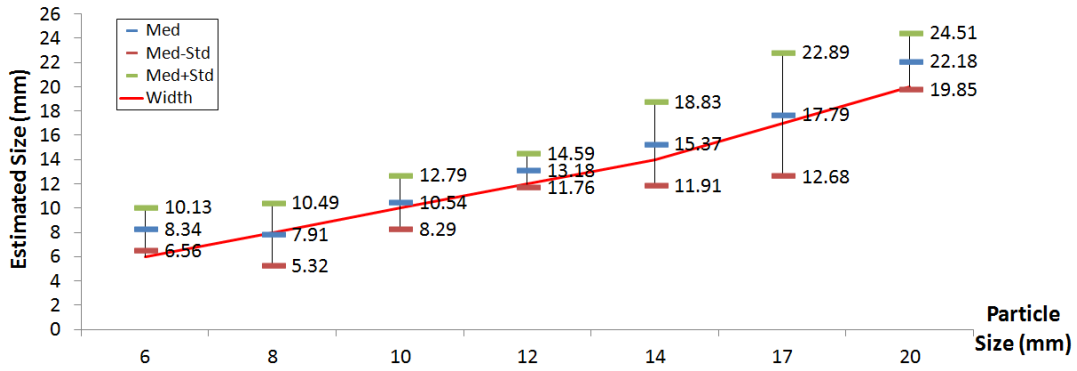

Figure 2.7: Measured versus actual particle diameter

of our results, we used a Bland–Altman statistical test [Bland and Altman, 1986]. For each ball bearing, we plotted the difference between the real and estimated values (S_1 and S_2) as a function of the mean of these two samples. Next, we computed the mean (m) and standard deviation (σ) of the difference ($S_1 - S_2$) and the percentage of points (p), which were beyond the interval $[m - 2\sigma, m + 2\sigma]$, i.e., >0.95 of our values are within 2σ of the mean. We found that $p = 0.05$, meaning that 95 % of our measurements are inside the 95 % limit of agreement (Figure 2.8). The Bland-Altman test allows us to assert that the measurement is statistically equivalent to the ground truth.

2.2 Stromboli volcano

Our study focuses on 13 eruptions from the South-West crater in 2012, plus 13 eruptions from the South-West and 5 eruptions from the North-East in 2014. We begin by considering a single eruption from the South-West crater in 2012. The eruption occurred on 30 October

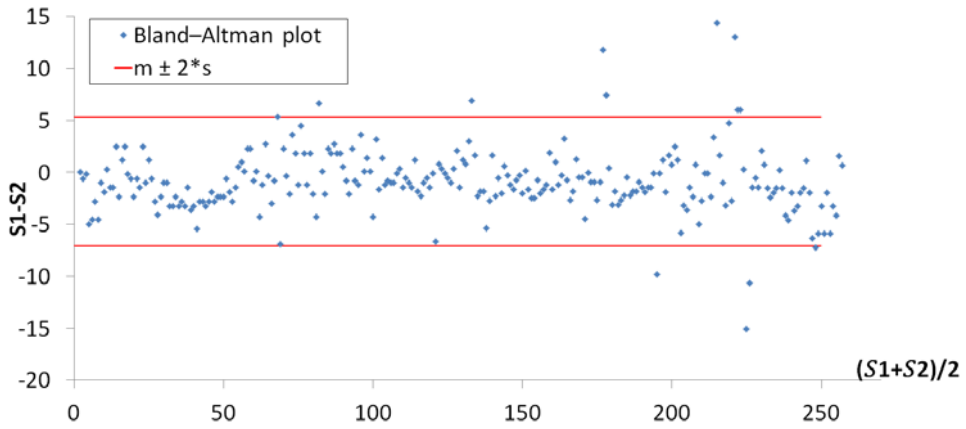

Figure 2.8: Bland–Altman plot between two sample sets S_1 and S_2

at 11:58:26 UTC (reference: 09-30_1354l3067). The eruption lasted 17 seconds during which 4 382 particles were detected meaning that, when time-averaged, the emission rate was 258 particles per second. The particle size distribution has a peak at the interval of 8 to 10 cm, with a mean particle width of 11 cm and a standard deviation of 4 cm, indicating a slight skew towards larger particles. Such a positive skew is common to all distributions (Table 2.2). The particle mass distribution revealed that most particles had a low mass, i.e. 3 773 or 86 % of all of the detected particles had a mass of less than 2 kg. This population accounts for 2 470 kg, or 45 % of the total mass. The remaining 1 912 or 14 % of the particles thus accounted for 55 % of the total mass ejected, this being 5 450 kg. The particle velocity distribution had a mode between 20 m/s and 30 m/s, with an average velocity of 34 m/s on which the standard deviation is 23 m/s. Particle velocities at Stromboli are generally less than 100 m/s [Chouet et al., 1974; Blackburn et al., 1976; Ripepe et al., 1993; Patrick et al., 2007]. Here, 97.6 % of all of particles measured have velocities of less than 100 m/s. However, 103 particles (2.3 %) had velocities greater than 100 m/s and up to 216 m/s. This approaches the higher velocities recently found for normal activity at Stromboli by Taddeucci et al. [2012a], Delle Donne and

Ripepe [2012], Harris et al. [2012] and Genco et al. [2014]. All of our fast moving particles are relatively small being less than 20 cm in width. The kinetic energy carried by lapilli and bombs during this eruption was 4.1 MJ, the equivalent of 1 kg of TNT. This is consistent with the kinetic energy range of 0.7 to 5.2 MJ as measured at Stromboli during four explosions by Ripepe [1996] in 1991. These similarities down the years point to a consistency in the intensity and magnitude of activity over the time scale of decades, and to the temporal resilience of the system.

Table 2.2: Comparison of data for a single explosion from 2012, all SWC explosions from 2012, all SWC explosions from 2014 and all NEC explosions from 2014

Parameter	Set	Minimum	Maximum	Mean	Standard deviation	Skew	Kurtosis
Width (cm)	09-30_1354130 67	5.5	37	11	4.0	1.7	4.4
	SWC 2012	5.5	64	12	5.5	2.2	7.8
	SWC 2014	5.7	73	7.8	5.0	4.4	27
	NEC 2014	6.1	64	9.3	5.3	3.1	14
Mass (g)	09-30_1354130 67	153 ± 17	$0.3 \times 10^5 \pm 0.4 \times 10^4$	$1.2 \times 10^3 \pm 1.4 \times 10^2$	$2.2 \times 10^3 \pm 2.4 \times 10^2$	6.1	53
	SWC 2012	153 ± 17	$2.1 \times 10^5 \pm 2.4 \times 10^4$	$2.3 \times 10^3 \pm 2.6 \times 10^2$	$6.2 \times 10^3 \pm 6.8 \times 10^2$	12	230
	SWC 2014	174 ± 19	$2.9 \times 10^5 \pm 3.2 \times 10^4$	$1.2 \times 10^3 \pm 1.3 \times 10^2$	$6.9 \times 10^3 \pm 7.7 \times 10^2$	16	385
	NEC 2014	215 ± 24	$2.2 \times 10^5 \pm 2.5 \times 10^4$	$1.6 \times 10^3 \pm 1.8 \times 10^2$	$6.3 \times 10^3 \pm 7.0 \times 10^2$	14	307
Velocity (m/s)	09-30_1354130 67	8.2	216	34	23	2.9	12
	SWC 2012	7.7	224	33	24	3.1	13
	SWC 2014	8.0	226	51	39	1.5	2.1
	NEC 2014	8.6	240	53	39	1.8	3.0
Average total kinetic energy (MJ)	09-30_1354130 67			4.1			
	SWC 2012			3.9			
	SWC 2014			4.4			
	NEC 2014			11			
Average number of particles detected per second	09-30_1354130 67			260			
	SWC 2012			156			
	SWC 2014			202			
	NEC 2014			451			
Total number of particles detected	09-30_1354130 67			5 449			
	SWC 2012			29 552			
	SWC 2014			31 493			
	NEC 2014			22 175			

2.2.1 Campaigns Results

The 2012 dataset

Statistically, the distribution for all parameters derived from the total 2012 dataset was similar to that obtained for the single eruption described above. We thus assume that all events are analogous or self-similar and can be related to the same process. From here onwards, we consider the total dataset as a reliable descriptor of all 2012 events we studied. In 2012, emission durations ranged from 5 seconds to 50 seconds, with an average of 16 seconds. The number of particles detected during a single explosion ranged from 650 to 5 240 with an average of 2 270. A total of 29 550 particles were detected for all 13 eruptions. Due to the large number of the particles detected, the dataset is statistically robust; even if some false detections occurred, they will have a vanishingly small impact on the final statistics. The particle size distribution (Figure 2.9.a) reveals that the majority of the particles (82 %) have widths of between 5 cm and 15 cm with an average of 12 cm. However, these results have to be treated with caution because particles with widths less than 5 cm will not be detected due to the spatial resolution of our system. Masses erupted a range between 1 270 kg and 11 820 kg with an average of 5 340. Individual bombs have masses up to 214 kg and, while 90 % of the particles were less than 5 kg, 75 % were less than 2 kg (Figure 2.10.a). However, the 1 021 particles greater than 25 cm (i.e., 3.4 % of the total detected particles) account for 36 % of the total mass. Velocities again had a mode between 20 m/s and 30 m/s with an average of 33 m/s (Figure 2.11.a), and 97 % of particles had a velocity less than 100 m/s with a maximum velocities being up to 224 m/s. Again, only the smallest particles are characterised by such high velocities.

a) SWC 2012

b) SWC 2014

c) NEC 2014

Figure 2.9: Particle size distribution for eruptions from SWC in 2012 (a), SWC in 2014 (b) and NEC in 2014 (c) with, the cumulative number of particles detected for each case.

The SWC dataset from 2014

In 2014, another campaign was carried out at Stromboli. First, we focus on the 13 eruptions which occurred from the South-West crater. This dataset provides information on a further 31 500 particles. Emission durations ranged from 6 s to 22 s, with an average of 12 s, and the number of particles detected during a single explosion ranged from 610 to 4 385 with an average of 2 420. A total of 31 500 particles were detected during all 13 eruptions. The particle size distribution (Figure 2.9.b) reveals that the majority of the particles (63 %) were below 6 cm and the distribution was tighter than in 2012. Masses erupted ranged between 1 840 kg and 4 740 kg, with an average of 2 908 kg. Ninety-six percent of particles were less than 5 kg, and 93 % were less than 2 kg (Figure 2.10.b). However, the 584 particles that were greater than 25 cm (i.e., 1.8 % of the total detected particles) accounted for 56 % of the total

a) SWC 2012

b) SWC 2014

c) NEC 2014

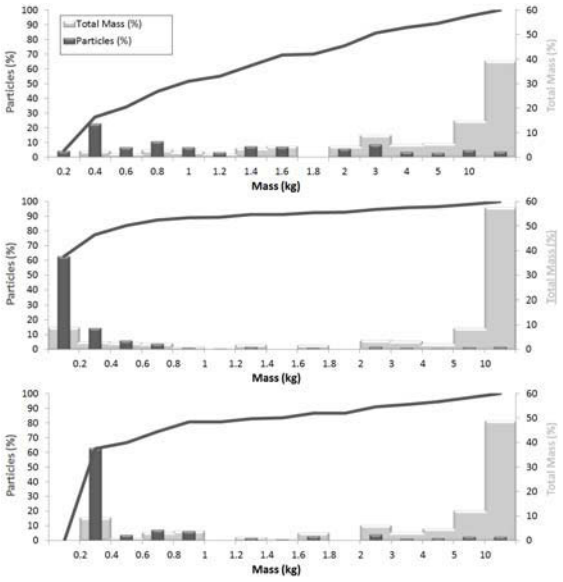

Figure 2.10: Particle mass distribution, total mass distribution and distribution function, for eruptions from SWC in 2012 (a), SWC in 2014 (b) and NEC in 2014 (c). The light gray histogram shows the impact of heavy particles on the total mass.

mass. The particle velocity distribution (Figure 2.11.b) had a mode between 20 m/s and 30 m/s. The average was 51 m/s, with 88 % of the particles having a velocity of less than 100 m/s, and maximum velocities being up to 226 m/s.

The NEC dataset from 2014

Now, we consider the five eruptions which occurred at the North-East crater in 2014. This dataset provides information for a further 22 175 particles. Emission durations ranged from 7.5 s to 16 s, with an average of 10 s. The number of particles detected during a single explosion ranged from 2 580 to 5 320 with an average of 4 435. A total of 22 175 particles were detected during all five eruptions. We note that emission rates in terms of number of particles per second (pps) was higher at NEC (450 pps) than at SWC during both 2012 (155 pps) and

a) SWC 2012

b) SWC 2014

c) NEC 2014

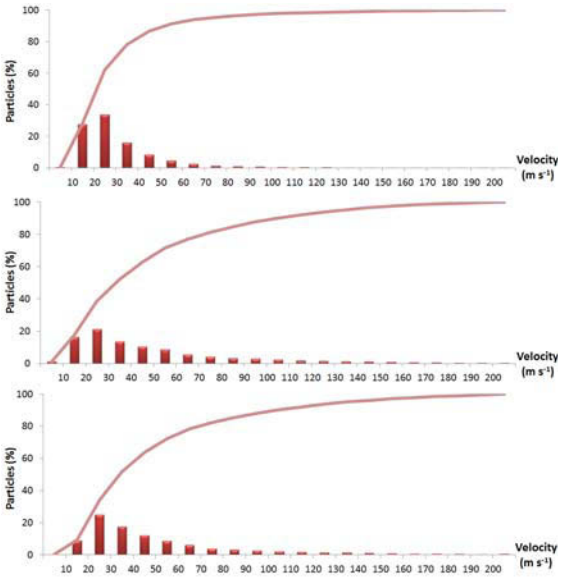

Figure 2.11: Particle velocity distribution and distribution function for eruptions from SWC in 2012 (a), SWC in 2014 (b) and NEC in 2014 (c).

2014 (200 pps). The particle size distribution for NEC (Figure 2.9.c) was similar to that of the SWC with a mode between 6 cm and 8 cm. Masses recorded at NEC ranged between 3 540 kg and 10 255 kg with an average of 6 845 kg. Ninety-five percent of all particles erupted were less than 5 kg, and 87 % were less than 2 kg (Figure 2.10.c). However, the 495 particles that were greater than 25 cm (i.e., 2.2 % of all detected particles) accounted for 45 % of the total mass. The velocity distribution (Figure 2.11.c) had a mode between 20 m/s and 30 m/s with an average of 52 m/s. For the NEC case, 88 % of particles had a velocity less than 100 m/s, with maximum velocities being up to 240 m/s.

Differences: 2012 versus 2014 – a measure of fragmentation efficiency?

The proportion of low mass particles erupted in 2012 (75 % < 2 kg) was less than in 2014 (93 % < 2 kg at SWC, and 87 % at NEC). This difference is reflected in the size distributions

that were skewed towards bombs in 2012 and towards lapilli in 2014. Because bombs account for a disproportionate percentage of the mass of each eruption, the bomb-dominated SWC eruptions of 2012 were generally of a higher mass (average of 5 340 kg) than in 2014 (average of 2 908 kg), even though particles were erupted at a lower rate in 2012 (155 pps in 2012 versus 200 pps in 2014). This is all consistent with greater degrees and higher efficiency of fragmentation, and higher explosion energies in 2014 as opposed to 2012, so as to create a larger number of smaller particles in the second year. Indeed, kinetic energies were also higher at SWC in 2014 (average = 4.4 MJ) than in 2012 (average = 3.9 MJ). In addition, eruptions in 2012 had lower average velocities (33 m/s in 2012 versus 51 m/s in 2014) and a lower number of high velocity particles, i.e. 3 % were ejected at velocities greater than 100 m/s in 2012 compared with 12 % in 2014. This seems to support the model where small particles are carried by the fast moving gas phase [Harris et al., 2012], where the greater number of small particles available for gas-transport in 2014 meant that there was a larger population of high velocity particles in that year. These results point to a scenario whereby changing degrees of fragmentation efficiencies can be tracked using the global mass and kinetic energy parameters, as well as the typical particle velocity, size, and number statistics for each eruption.

2.2.2 Validation

In Figure 2.12, we compare our results (Figure 2.12.b) with those obtained from 690 bombs sampled from a fall out field associated with a major (bomb-dominated) explosion (Figure 2.12.a) at Stromboli [Gurioli et al., 2013]. We also compare our results with those obtained from a weak (lapilli-dominated) explosion sampled towards the end of the 2012 campaign [Harris et al., 2013b]. This lapilli sampling involved laying out of four tarps (3×4 m plastic

sheets) on 28 September 2012. These were placed on the outer flank of the SWC, 75 m SW of the active vent, and were retrieved on 5 October 2012. Upon retrieval all juvenile coarse ash, lapilli and Pele's hair were collected. This sample provides the "multiple explosion" distribution of Figure 2.12.c. On 5 October, fine material from SWC explosions was being blown (by the wind) off of the top of plume towards the SW. Here, material landed on a tarp that had just been cleaned following an explosion at 15:50 (local time). Fall out onto the tarp began 20-30 seconds after bomb fall out within the crater was heard to finish, and all coarse ash, lapilli and Pele's hair that arrived during the 10 second-long fall out event were collected. These were returned to the lab where their sizes and masses were measured. In total 48 lapilli were collected for the 5 October 15:50 event with a total weight of 5.27 g, the largest being 2.3 cm (0.68 g) and the smallest being 2-3 mm (0.01 g). This sample provides the "single explosion" distribution of Figure 2.12.c.

The thermal-camera-derived particle size distribution is between the "bomb-dominated" and "lapilli-dominated" end-members (Figure 2.12.b), and is similar to the distribution obtained by Colò [2012] for a normal explosion at Stromboli. We note that the fine tail made up of fine lapilli and coarse ash is not well defined because of the detection limits of our camera. In effect, the particles smaller than the pixel size, i.e. 5.3 cm in diameter, are not detected. However, even if the number of particles that comprise the lapilli and ash component of such emissions is significant, their impact in terms of mass is not [Gurioli et al., 2013].

The "lapilli-dominated" samples collected from the tarps at SWC during the same campaign have a lapilli and coarse ash dominated distribution (Figure 2.12.c). This is consistent with visual observations. On 27 September 2012, SWC was noted as giving impressive bomb and gas rich explosions, with heavy bomb loading to 250 m above the vent, with NEC giving

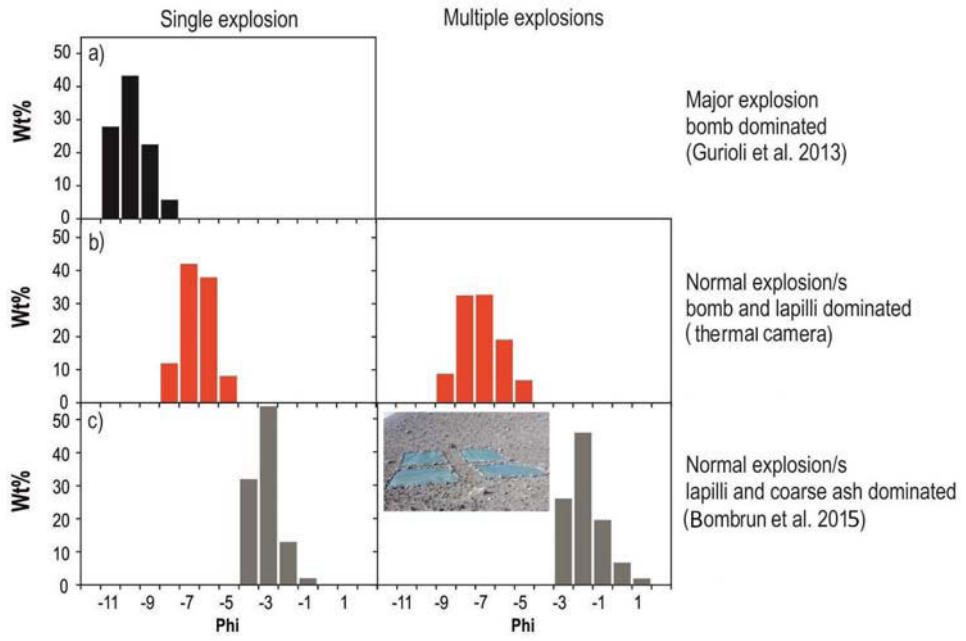

Figure 2.12: Particles weight percent by class size ϕ. For three eruption types: a bomb-dominated explosion (a), a normal explosions (b) and a lapilli-dominated explosions (c).

less frequent and less vigorous eruptions. However, by 5 October the SWC was giving ash jets loaded with small bombs and lapilli, with the highest fragments reaching just 50 m above the vent. By this time, however, NEC was giving impressive bomb-rich bursts to 200-250 m. While most of the events sampled by the thermal camera were collected during the first two days of the 2012 sampling period (27-28 September), the sampling that contributes to the size distribution given in "multiple explosion" distribution of Figure 2.12.c was completed on 5 October and comprised fine-grained material that fell out on that day. Bad weather would have blown away all other material settling onto the sheets during preceding days, and no bombs or burn holes were observed. This is supported by the agreement between the "multiple explosion" and "single explosion" distributions of Figure 2.12.c.

For the single explosion sampled at 15:50 on 5 October, if we multiply the number of coarse ash, lapilli and Pele's hair falling in our 12 m^2 control zone (areal number density = 4 m^{-2}) by the 4 000 m^2 fall out area identified using the thermal imagery obtained from an airborne (helicopter) vantage point), we obtain a total particle number of 16×10^3 for this size range. This compares with a particle number of 1.3-1.6 $\times$ 10^3 for the coarse lapilli-bomb size range obtained for SWC eruptions using the thermal camera on the same day. However, if we multiply the mass area density for coarse ash, lapilli and Pele's hair (0.44 g m^{-2}) by the fall out area we obtain 1.8 kg, compared with 1 270 to 11 822 kg obtained for the lapilli and bomb size range. Thus, for this lapilli-dominated event, while the thermal camera only captured 10 % of the particles by number, it captured 100 % of the emission by mass.

The last parameter that cannot be validated from the ground-deposit is the velocity of our particles. However, our results from Stromboli are consistent with ballistic particle velocities estimated using various other methodologies applied to image data for eruptions at Stromboli

and Etna since 1974 (Table 2.3). The last row of Table 2.3 shows that the correlation between our results and those previous studies agree within the 68 % tolerance interval.

Uncertainty on our final level of measurement is a function of errors in particle shape and velocity, lack of constraint on the particle density, and errors due to omission and commission or false positives (missed particles and mis-identified particles). The error in parameter computation is a function of pixel size, this being constrained by the sensor resolution, and camera distance from the target. False detections are hard to identify, however the image environment at Stromboli is quite static so that errors of omission dominate over errors of commission. The controlled experiment defined in Part 2.1.5 recovered 90 % of particles released, with 95 % of the size measurements being within the limit of agreement.

For measurements of lapilli and bomb dominated explosions, our method thus appears valid and offers a means to obtain a larger database than is possible by field sampling. It can also provide data in real-time, multiple times a second. In addition, we measure the particle dimensions and shape at the vent, before modification due to in-flight tearing or collision, or fragmentation upon ground-impact. To push the lower limit of our detection to smaller sizes, we could move the equipment closer to the source, or apply lenses with greater magnification, to the extent that safety and technology allows.

2.2.3 Discussion

Our method allows the construction of a dataset containing size, mass and velocity measurements for 83 000 particles emitted during 31 explosions. Similarity between the parameters derived for the individual event used, the 2012 data set and the 2014 data set show that the events are extremely repeatable, suggesting bomb-dominated eruptions (Type 1) and ash-

Table 2.3: Particle Exit Velocities for Eruptions at Stromboli and Etna.[a]

Study		Velocity (m/s)			Reference
Eruption	Method	Min	Max	Mean	
Etna (Italy)	Photo-ballistics	15	79	51[b]	McGetchin et al. [1974]
Stromboli (Italy)	Photo-ballistics	2.5	72	26	Chouet et al. [1974]
Stromboli (Italy)	Average particle tracking	-	-	22[c]	Ripepe et al. [1993]
Stromboli (Italy)	Acoustic Doppler Sounder	20	80	41	Weill et al. [1992]
Stromboli (Italy)	Micro Radar Doppler	0	32	10	Hort and Seyfried [1998]
Stromboli (Italy)	Thermal video (6 Hz)	26	71	47	Vanderkluysen et al. [2012]
Stromboli (Italy)	Thermal video (30 Hz)	3.0	101	34	Patrick et al. [2007]
Stromboli (Italy)	Thermal video (30 Hz)	9.0	129	46	Harris et al. [2012]
Stromboli (Italy)	Thermal video (50 Hz)	23	203	-	Delle Donne and Ripepe [2012]
Stromboli (Italy)	High-speed video (500 Hz)	<50	405	136	Taddeucci et al. [2012a]
Stromboli (Italy)	High-speed video (500 Hz)	0.1	241	51	Gaudin et al. [2014b]
Stromboli (Italy)	High-speed Thermal video	7.7	240	45	This study
Mean $\overline{x}$ (Standard deviation σ)		11 (10)	141 (113)	49 (35)	
Confidence intervals[d]		1.0−21	28−254	14−84	

[a] Note that particles with diameters of 27 to 64 cm moving in the velocity range of 35-46 m/s are also reported in Figure 8a of Ripepe et al. [2001].

[b] Median value.

[c] Mean of the means from 6 eruptions with $\overline{x}$ of 16.3, 18.5, 15.8, 14.4, 22.3 and 21.7 m/s.

[d] The confidence interval is $[\overline{x}\text{-}\sigma - \overline{x} + \sigma]$. Data of Ripepe, [1993] and minimum value from Taddeucci et al., [2012a] are not included.

dominated eruptions (types 2a, 2b) can be associated with a similar source mechanism which did not change within or between our measurement periods.

Particle numbers, sizes, shapes and masses

Our particle counts range between 612 and 5 316 per eruption, with an average of 2 684 particles. In Figure 2.13, we assess particle shape in terms of the following normalised shape index: $r = (r_L - r_S)/(r_L + r_S)$. Using this index, a perfectly oblate shape will have a value of -1/3 whereas a perfectly prolate shape will have a value of +1/3; a perfect sphere will have a value of zero. We found that only 17 % of our particles approximate a spherical shape. Of the remaining 83 %, 29 % are oblate and 54 % are prolate. The dominance of the prolate shape is consistent with deformation or stretching in the direction of motion. Typically our prolate particles are up to 5.6 times longer (in the flight direction) than they are wide (index = 0.7). In the oblate direction, as we move from an index of -0.2 to -0.6 fragments become increasingly string-like, being stretched in the horizontal direction until we reach a value of -1; which is technically impossible. On the video, fluid particles are seen to stretch in the flight direction, tear and spin, with stretching occurring over timescales of tenths of a second. As already stated, our aim is to capture the initial vent-leaving shape before in-flight or ground impact-induced deformation and secondary fragmentation. We observe both of these processes beginning to occur, so as to modify the size and shape distributions, over just the first few meters of flight. However, we find no relation between size and shape, probably because all of our particles are quite large, molten and deformable, so that all sizes in our range undergo motion-induced deformation.

The majority of Chouet et al.'s [1974] particles have diameters of less than 30 cm. In

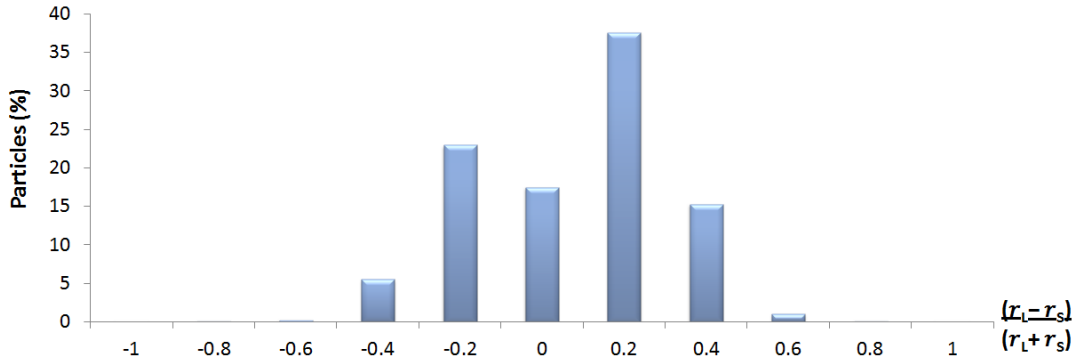

Figure 2.13: Particle shape distribution of the whole dataset (SWC 2012 and SWC/NEC in 2014). Most of the particles do not have a spheroid shape but have either an oblate or prolate shape.

our study, 99 % of particles are below this limit, of which 62 % fall in the bomb category (i.e., they are >6.4 cm). This reduces to 11.5 % if we consider the absolute total from the projection of Figure 2.14. Our projections indicate that, by size, the emission is dominated by particles smaller than 5.3 cm. This is consistent with the comparison with the lapilli field sample completed in 2012, where the thermal camera captured around 10 % of the particles by number. In terms of total erupted masses during individual explosions, we obtain a range of 1 270 to 11 822 kg, with a mean of 4 585 kg. This is consistent with recent measurements of mass, which indicate eruptive masses of up to 35 000 kg [Ripepe et al., 1993; Ripepe, 1996; Harris et al., 2012], compared with 8 and 10 kg obtained by Chouet et al. [1974].

Projections and correlations in the total dataset

If we plot size against the number of particles, we find that number increases with decreasing size in an exponential fashion (Figure 2.14). The trend indicates a total number of lapilli and bombs emitted during all 31 events of 450 000. Because we detected a total of 83 000 particles, due to spatial resolution problems, we are missing around 367 000 of the smallest

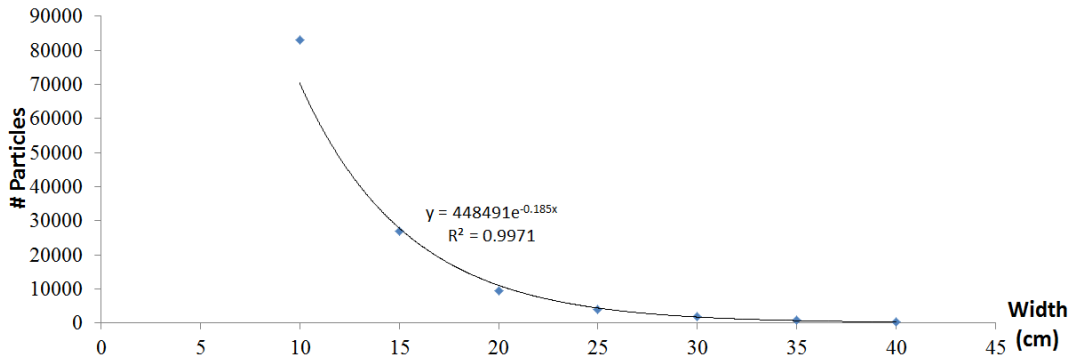

Figure 2.14: Trend between the total number of particles detected and their size

(< 5.3 cm) particles. This leads us to underestimate the total particle number by 80 %.

The mass plot shows a linear relation between particle size and mass (Figure 2.15). The relation suggests a total mass erupted during the 31 events of 151 000 kg, compared with the total mass measured of 142 000 kg. This means we have captured at-least 94 % of the total mass emitted. This is consistent with the findings of Gurioli et al. [2013] who found that 31 % of the mass erupted during a major explosive event at Stromboli was accounted for by the largest particles. In our case, most of the mass is accounted for by particles with a size greater than 5.3 cm. It means that even if we only detect 20 % of the particles by number, we only under-estimate the total mass by 6 %, although both absolute totals (number of particles and mass) may be obtained from extrapolation of the two relations. This is again consistent with Gurioli et al. [2013] who found that although the largest particles (> 1 m) accounted for 31 % of the deposit by volume, they only accounted for 1 % by number.

By number, the emission is thus dominated by small (<5 cm) particles. Currently we can only obtain the small particle population by extrapolation from our limited, albeit statistically robust, data set. However, by mass, we can directly measure almost 95 % of the emission.

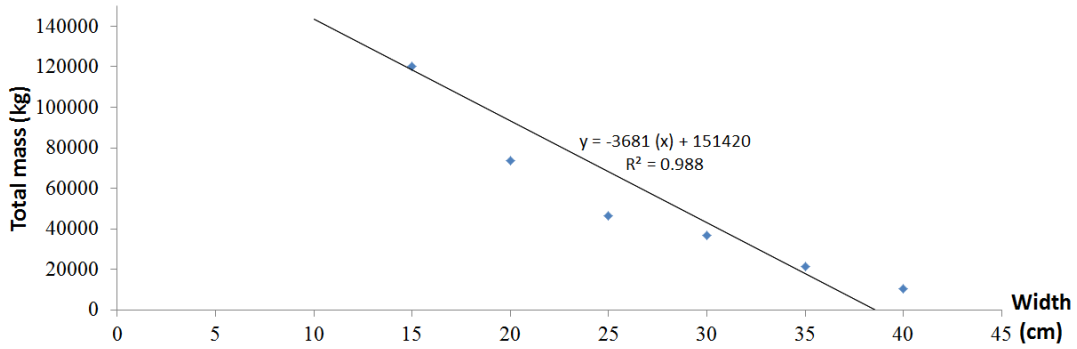

Figure 2.15: Trend between mass and width of particles

If we plot size against velocity we find a degree of scatter. However, only the largest particles have the lowest velocities, and the smallest particles have the highest velocities (Figure 2.16). This is consistent with the results of Harris et al. [2012] who found that, during explosions at Stromboli, a spray of small, high velocity particles was launched at the beginning of 32 eruptions analysed. If we extrapolate using the velocity versus size trend as plotted in red on Figure 2.16, we obtain,

$$U = -120.2ln(D) + 504.93 \qquad R^2 = 0.97 \tag{2.15}$$

over the size range 0.2 cm to 60 cm. Assuming that the particles reach their terminal velocity in the conduit, the velocity of the gas cloud (U_{gas}) can be related to the velocity of the particles (U) by [Steinberg and Babenko, 1978]:

$$U_{gas} = U + \left(\sqrt{\frac{4g\varrho_{particle}}{3C_D\varrho_{gas}}}\right)\sqrt{D} \tag{2.16}$$

where g is acceleration due to gravity, $\varrho_{particle}$ is the particle density, ϱ_{gas} is the gas density, C_D

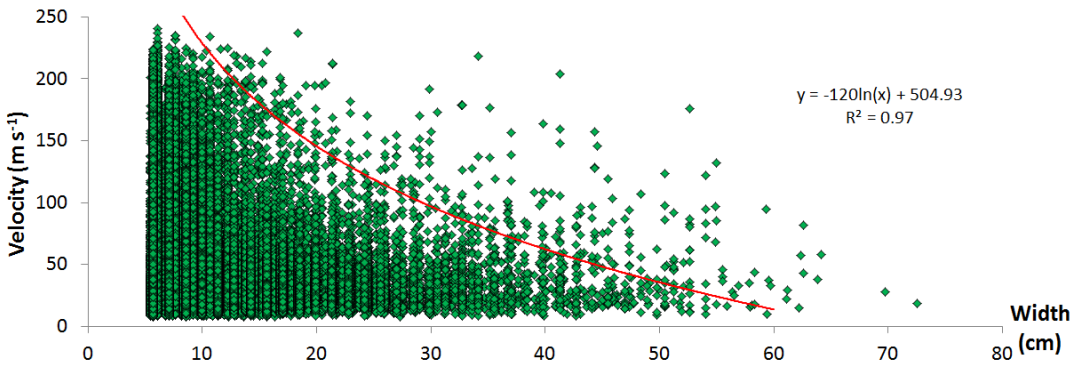

Figure 2.16: Correlation between size and velocity for particles detected in the whole dataset (SWC 2012 and SWC/NEC in 2014).

is the drag coefficient and D is the particle diameter. Following Chouet et al. [1974], this equation has commonly been reduced to [e.g., Ripepe et al., 1993]:

$$U = U_{gas} - k\sqrt{D} \tag{2.17}$$

The trend of Equation 2.15 defines the maximum limit of the D versus U scatter for each of our 31 explosions. This empirical fit can also be approximated by,

$$U = U_{gas} - \sqrt{D} \tag{2.18}$$

Thus, following Steinberg and Babenko [1978], the upper limit of the relation follows a rule whereby particle velocity decreases with the square root of particle diameter. Below this limit, we have a "black cloud" of data points (Figure 2.16). This scatter is likely due to the large number of gas densities likely apparent between eruptions, and during single events [Harris et al., 2012]. Our observations of both visible, thermal and UV video suggest that all of the parameters in the Steinberg and Babenko [1978] relation, including gas density, is likely change over

the time scale of a few tenths of a second, making application of such a simple relation to a single explosion problematic to say the least. In addition, although some particles may be coupled to the gas phase, thereby obeying this law, others will be undergoing varying degrees of decoupling. Complete decoupling means we revert to the relation,

$$U = \sqrt{\frac{dg}{sin(2\vartheta)}} \tag{2.19}$$

in which d is distance reached by the particle and ϑ is the launch angle. In short, the "black cloud" of Figure 2.16 is formed because particles with the same width show a large range of velocity and vice versa: the same velocity can be reached by different particles. This scatter indicates a large variability in the analysed explosive dynamics. The trend becomes narrower towards the large particle – low velocity end of the plot, indicating that variability increases as particle size decreases; suggesting that only the smallest particles are capable of revealing the complexities and variability's of particle launch dynamics.

Using Equation 2.15, we obtain a maximum velocity of 456 m/s for a particle width of 1.5 cm, in line with the findings of Taddeucci et al., [2012a], and up to 700 m/s for the smallest particle to which this relation can be applied. Note that these 'extrapolated' maximum velocities' are based on extrapolation of data for observed particles into a field of non-observed particles. However, the excellent correlation coefficient [$R^2 = 0.97$] for the trend gives us confidence in these extrapolated values for particles that were too small to resolve by our camera system. For us, the extrapolations are thus only valid down to lower size range of lapilli and cannot be used to assess ash parameters. Following our argument above, our physical explanation for these high velocities is that of Harris et al. [2012] whereby the smallest particles are

carried by the fast moving gas phase which accounts for the highest velocities found for the lapilli, so that they are markers for the gas velocity. Bombs are decoupled from the gas phase due to their mass and are just driven by momentum so that lowest velocities are found for the largest particles.

Automatic Classification

Patrick et al. [2007] defined Type 1 eruptions, which are dominated by coarse ballistic particles, and Type 2 eruptions, which are ash dominated with (2a) or without (2b) large number of lapilli- to bomb-sizes pyroclasts. To this, Leduc et al., [2014] added a third category: Type 0. This event type is characterised by gas-dominated, high velocity jets with velocities of 100's m/s but involving few or no lapilli or bombs. Goto et al. [2014] geophysically defined such gas-rich and fragment-poor event types finding them to be characterised by a dominant shock-wave component and supersonic velocities. Although Goto et al. [2014] termed this eruption style Type 3, we prefer Type 0 because this nomenclature fits the initial classification philosophy:

- Type 2: Two solid components = fine (ash) plus coarse (lapilli + bombs);
- Type 1: One solid component = coarse (lapilli + bombs);
- Type 0: No solid components = gas only (with aerosols);

Of course there is a continuum between these three classes of normal explosion. Type 0 may have a few or several particles entrained in the gas jet [Leduc et al., 2014]; Type 2, as recognised by Patrick et al. [2007], may range between fine (Type 2a) and coarse (Type 2b) particle dominated. Likewise, Type 1 may be more or less particle loaded. All normal explosions will

involve gas, but the key in this classification is the relative proportions of gas to fine and coarse material.

To classify the eruption types we used their histograms for velocity, size, and mass, all parameters being summarised in Table 2.2. For velocity and size we used 11 bins, and 26 bins for mass, which when lumped together provided a total of 48 dimensions available for event characterisation. We used the k-means algorithm of MacQueen [1967] an iterative refinement technique which partitions observations into k clusters by minimising the sum of intra-cluster variances. Usually, the Euclidean distance is used for clustering [e.g., MacQueen, 1967]. However, we used the Bhattacharyya distance [Bhattacharyya, 1943], which measures the similarity of two probability distributions, as is appropriate for the case in hand. We used k=3 to separate the events into three classes, Type 2a, 2b and 1 (we had no Type 0 cases), by running this clustering algorithm. We then completed a visual cluster analysis which classified the eruptions depending on their visual character as observed from viewing the thermal video. A comparison of the results from the automatic and manual methods is given in Table 2.4. We find that our algorithm separated out ballistic-dominated eruptions (Type 2b), mis-classifying only one event. However, there is some mixing of Type 2a and 1. This is because the classification is based on particle parameters and because Types 2a and 1 have similar particle characteristics, we cannot distinguish them using our data alone. This classification would be improved if we had simultaneous eruption of the fine particle and gas content. For now, if we lump 2a and 1 together, we only have one mis-classification (Table 2.4).

Table 2.4: Preliminary results of the clustering algorithm on the 2012 dataset. Classification done in three types: ash with bombs and lapilli (Type 2a), ash without lapilli and bombs (Type 2b) and gas dominated plus coarse (Type 1)†

Eruption reference	Type 2a	Type 2b	Type 1	Type 2a+1
09-27_154909271		V K		
09-27_155839983		V K		
09-28_135432903	V K			V K
09-30_125847157	K		V	V K
09-30_131721017			V K	V K
09-30_132029052			V K	V K
09-30_133102430_1			V K	V K
09-30_133102430_2	K		V	V K
09-30_134451828	K		V	V K
09-30_135413067	K		V	V K
10-05_144505552	V	K		V
10-05_145321701		V K		
10-05_150241747		V K		

†The visual clustering is represented by the black Vs whereas the K-means clustering is the red Ks.

Source mechanism

We see from Table 2.4 that, during the 2012 experiment, the eruptions cycled from ash-and-bomb rich (Type 2a and 2b) to bomb-and-gas rich (Type 1) and back again to 2a-2b over a time scale of 10 or so hours. We also find that during 2012 explosions had lower particle numbers, velocities and kinetic energies than in 2014, but involved greater masses. This, as already stated, points to a more efficient, energetic and gas driven explosion mechanism in 2014 compared with 2012.

Eruptions at Stromboli have been classically explained by generation of a large gas mass, or slug, which ascends the magma filled conduit to burst at the free-surface [Jaupart and Vergniolle, 1989; Vergniolle and Brandeis, 1996; James et al., 2004]. Bomb-rich eruptions may be the result of fragmentation of a viscous, degassed plug or rheological layer at the head of

the magma column which fragments upon arrival of the slug [Gurioli et al., 2014], and/or the extraction of the degassed material stuck to the conduit wall by passage of the slug [Lautze and Houghton, 2005]. Textures and associations of different textural facies, including the presence of dense, crystal-rich degassed material mixed with juvenile material in bombs sampled by Gurioli et al. [2014], was consistent with the cap-model. Breaking of a cap would also require a greater degree of seismic energy, as opposed to a situation where fragmentation is caused by bursting of a bubble at a low viscosity and yield strength magma surface [Gurioli et al. 2014; Leduc et al., 2014]. It would also explain lower particle numbers, velocities and kinetic energies, along with larger particles, during such events cap-dominated events. We thus suggest that during Type 1 and 2 activities, which possess these dynamic characteristics, a complete cap was in place which fragmented upon arrival of the gas slug, following the model of Gurioli et al. [2014].

During type 1 and 2 events, Gurioli et al. [2014] and Leduc et al. [2014] suggested that magma levels were relatively high with the magma column being capped by degassed material and/or, following Patrick et al. [2007], scoria. While fragmentation of the cap feeds an impressive Type 1 particle emission [Gurioli et al., 2014], the particles being accidental incorporation of previously degassed material [Harris et al., 2012], grinding of scoria adds the ash component to the Type 2 events [Patrick et al., 2007]. However, convective overturn of the cap can result in a cleaner conduit, with a lower level, where the bubble bursts at a fresh-magma surface, or through a thinner cap, so that the particle load of the gas jet is small-to-non-existent and exit velocities are high due to coupling of rare, but small, particles to the gas phase [Leduc et al., 2014]. These are Type 0 events. We indeed find that the fastest moving particles are small, but rare; and capable of attaining velocities towards 500 m/s. The fresh

conduit scenario fits our Type 1 scenario for the 2012 data set where seismic energy kinetic energy and particle mass is lower due to presence of a smaller cap than during the Type 2a and 2b events. In addition, the lower masses and smaller particle sizes, but high velocities, particle numbers and kinetic energies during 2014 suggest a more efficient, less cap-dominated, fragmentation model for 2014 compared with 2012. However, we do not record true Type 0 events as particle loads are still quite high and relatively high particle masses are inconsistent with true, completely cap-free and particle-free, Type 0 activity.

There is bound to be a continuum of styles from Type 0 through Type 1 to Types 2a and 2b. We suggest, that the continuum is from Type 0, which has the lowest particle masses and no cap influence, through Type 1 – which has moderate particle masses and some cap influence – to Types 2a and 2b, which have highest particle masses and a strong cap influence and/or interaction with scoria plugs. As we move through this sequence, the gas influence also decreases so that the size of the population of fastest moving particles decreases, kinetic energy decreases, but seismic energy increases as more energy is produced by cap breakage than simple bubble bursting in a low viscosity fluid. Fragmentation efficiency also decreases, so that the number of particles erupted decreases, but their size increases. Between the two end-member conduit scenarios, capped and uncapped, there is a density-driven convective overturn event [Allard et al., 1994; Stevenson and Blake, 1998], after which the cap rebuilds, to push the system back to the initial conditions. The duration of our cycles ($\approx$ 10 hours) may be the timescale of cap construction and overturn during the 2012 experiment. Indeed time scale of the persistence of our two eruption types and associated characteristics is consistent with time scale of convective overturn recorded in similar geophysical data sets at Stromboli [Ripepe et al., 2002; 2005; 2008]. Convective overturn at Stromboli has been associated with

changes in the seismic-acoustic-thermal delay [Ripepe et al., 2001; 2002], which are thought to relate to changes in the magma level [Ripepe et al., 2005; 2008]. Unfortunately, during our analysis period seismic signals were so weak that we were unable to examine delay times.

2.3 Conclusion

Strombolian eruptions are a relatively mild form of explosive volcanic activity. Emission of bombs, blocks and lapilli are common during normal explosion at Stromboli. Moreover, monitoring and collecting particles can be done over a reasonablely short distance with relative safety. However, despite the frequency of activity and number of particles involved in each emission, large, statistically robust databases for vent-leaving particle dynamics remain scarce. We used a new approach for detecting, tracking and parameterising small dim target in infrared images. The method is based on a mathematical morphology transformation hybridised with refinement by thresholding. Tracking is performed with a temporal correlation but improved and adapted to our system. We used both, pros (high-speed rate) and cons (tails artifact caused by the bolometer) of our camera system to enhance the matching accuracy. Results on artificial, controlled experiment show that our algorithm provides high reliability and an accurate detection capability regardless of the size distribution.

We collected high frame rate thermal video for 31 normal explosions at Stromboli during October 2012 and May 2014. Constraint of the vent-leaving particle dynamics allows us to move closer to validating a model for Stromboli, whereby the system cycles between periods of capped behavior during which the slug fragments through a cap of degassed magma, and free-surface behavior when the cap is absent so that slugs burst through lower viscosity (uncapped) magma. We used our algorithm to obtain a statistically robust database of 83 000

particles to compute the size, mass and velocity of each particle. Statistically, the distribution for all parameters computed for the 13 eruptions of 2012 is similar to that obtained for the 18 eruptions of 2014. Most of the particles have sizes between 5 cm and 15 cm, and the majority of individual bomb masses are below 0.4 kg. However, although 4 950 (6 %) of the particles are heavier than 5 kg, they represent 59 % of the total mass erupted.

The particle velocity distribution is positively skewed with a mode between 20 m/s and 30 m/s. Normal explosive activity at Stromboli has typically been viewed as involving large particles with relatively low velocities, with a mean of around 25 m/s [Chouet et al., 1974; Ripepe et al., 1993]. Recently, however, Delle Donne and Ripepe [2012] and Harris et al. [2012] have shown that a few small (typically lapilli-sized) particles can be ejected as part of an initial high velocity gas-jet, which has average velocities of 80 m/s and a maximum of 405 m/s [Taddeucci et al., 2012a]. Our data support this duality. The spatial resolution of our system allows us to detect particles down to 5 cm. In our data most of the bombs (size greater than 6.4 cm) are detected, and the bomb velocity distribution has a mode between 20 m/s and 30 m/s. Our data also indicate that the smallest particles, carried by the gas-jet, have the highest velocities with a maximum measured speed of 240 m/s, and a projected maximum potential velocity of 700 m/s for the smallest lapilli (0.2 cm in size), as extrapolated to the lowest particle size to which the relationship plotted on Figure 2.16 can be applied.

Patrick et al. [2007] and Leduc et al. [2014] classified normal explosions at Stromboli by visual clustering, the classification depending on whether they were ballistic dominated (Type 1), ash dominated, with (2a) or without (2b) particles, or gas-dominated (Type 0). We used our measured parameters to cluster our explosions into the same four classes. Correlation with seismic data helps to understand the source mechanism, and support the models

of Gurioli et al. [2014] and Leduc et al. [2014]: Type 2a and 2b events are a consequence of the presence of a viscous, degassed cap at the head of the magma column, its fragmentation providing 10^3 to 10^4 kg of solid material in each eruption. However, Type 1 are a consequence of slug bursting in a "cleaner" conduit, involving a lower mass of solid material, where true Type 0 eruptions involve almost no solid material. Thus, we need to model the impact of the finer component, the ash in the plume, to completely define the dynamics of a strombolian explosion.

The column of smoke is the relationship between earth and heaven, pointing out the path through fire to salvation.

The Penguin Dictionary of Symbols - Chevalier and Gheerbrandt

3

Plume Tracking Algorithm

3.1 Plume characteristics

3.1.1 Motivation

An eruption column (or volcanic plume) emitted during an explosive volcanic eruption consists of a mixture of particles, gase, and entrained atmospheric air [Sparks et al., 1997; Carey and Bursik, 2000]. Eruption-column height is a useful way of measuring eruption intensity is also a key source term for models [Bonnadonna et al., 2012] and provides a first-glance visual assessment of its hazard. Volcanic plumes are slow moving objects which may be dispersed on both local and global scales. Indeed, depending on the strength of the eruption, plumes can rise from a few tens of metres up to tens of kilometres above the vent. Several factors control the height that an eruption column can reach. Intrinsic factors include the diameter of the erupting vent, the gas content of the magma, the velocity at which the mixture is ejected, and the properties of the pyroclastic mixture [e.g. Wilson et al., 1978; Woods, 1988]. Extrinsic factors can also have an impact, with winds limiting the height of the column [Bursik, 2001], and the local atmospheric temperature gradient potentially decreasing the buoyancy of the plume.

The threat the airborne volcanic particles represent to both human health and aviation safety is a well-known issue and a hot topic during the last decade. From a microscopic point of view, ash particles are abrasive and can be so fine that they are ingested deep into the lungs and/or cause acute ocular problems. Ash-related poor health symptoms include respiratory problems (nasal, throat and airway irritation, coughing and severe bronchitic symptoms) [Martin et al., 1986; Horwell and Baxter, 2005], eye symptoms (corneal abrasions or scratches, acute conjunctivitis, eye inflammation, photosensitivity) [Fraunfelder et al. 1983] and skin ir-

ritation (not common unless the ash is acidic). A person exposed to fine ash for many years can develop serious lung disease, this period being reduced (days to weeks) if the ash contains crystalline silica [Baxter, 2000; Gudmundsson, 2011]. Ash fall can also have indirect effects such as road deterioration (and poor surface grip), power outage, water contamination, and roof collapse [e.g. Blong, 1984].

On 24 June 1982, British Airways Flight 9 (BA 09) emergency-landed in Jakarta after it flew into a cloud of volcanic ash thrown up by the eruption of Mount Galunggung (Indonesia) resulting in the failure of all four engines [Tootell, 1985]. A nearly identical incident occurred on 15 December 1989 when KLM Flight 867 flew into the eruption plume of Mount Redoubt (Alaska) causing all four engines to fail and forcing the crew to make a safe, but emergency landing at Anchorage [Casadevall, 1993]. In each case, the pilots were caught by surprise but they were able to glide far enough to exit the ash cloud, and restart the engines. In fact, pilots observed St. Elmo's fire, noted the acrid smell of sulfur gas, observed fine dust quickly filling the cabin and experienced moderate turbulence whilst in the ash cloud. Ash also entered the jets' engines and caused surging, flameout and immediate thrust loss of all four engines [Miller and Casadevall, 2000]. No on-board systems were able to detect the cloud (the weather radar showed clear skies) and only three minutes elapsed between the St. Elmo's fire effect on the windscreen and the moment that all four engines failed. Following these aviation incidents, and a rapid and sustained growth in air traffic, airborne volcanic ash has received increased attention from both the carrier and the volcanology communities [Bonadonna et al., 2012].

Imaging eruption plumes is an essential component in improving the understanding of plume dynamics and the hazards they pose. However, relatively few eruption plumes have

been imaged with the original intention of making scientific measurements [Sparks et al., 1997] and, furthermore, very few of these have been acquired at a frame rate sufficient to capture dynamic processes occurring in the plume [Clarke et al., 2002; Formenti et al., 2003]. Finally, due to the complexity of ascending volcanic plumes and despite the increasing availability of remote sensing techniques, tracking plume ascension, computing plume and source parameters, and modeling the impact of the vent geometry and exit conditions on the plume dynamics remain major challenges [Patrick et al., 2010; Harris et al., 2013a; Valade et al., 2014]. This study provides a fast and robust algorithm which can be used on volcanic site to estimate several plume parameters such as height, width and spreading angle at regular intervals of time (Figure 3.1), from which the plume parameters required to properly constrain geophysical models can be obtained. These parameters have previously been retrieved from thermal video for Strombolian eruptions [Patrick, 2007; Sahetapy-Engel and Harris, 2009; Valade et al., 2014]. Furthermore they can be used to infer entrainment dynamics in these plumes as a function of conditions such as particle concentration and size distribution as well as source size, shape and velocity [Jessop and Jellinek, 2014; Cerminara et al., 2015; Jessop et al., 2015]

3.1.2 Morphology

Following Turner [1962], the basic conceptual model for the plume includes two main parts: the steady plume and the plume front which is the uppermost head of the plume fed continuously by the steady plume. During the ascent of the plume, changes in intrinsic and environmental parameters shape the plume into four main types defined by Turner [1969] (Figure 3.2). On the basis of the morphology, they are defined as follows:

1. Jets - A high-velocity plume driven by high initial momentum [Morton, 1959; Crapper,

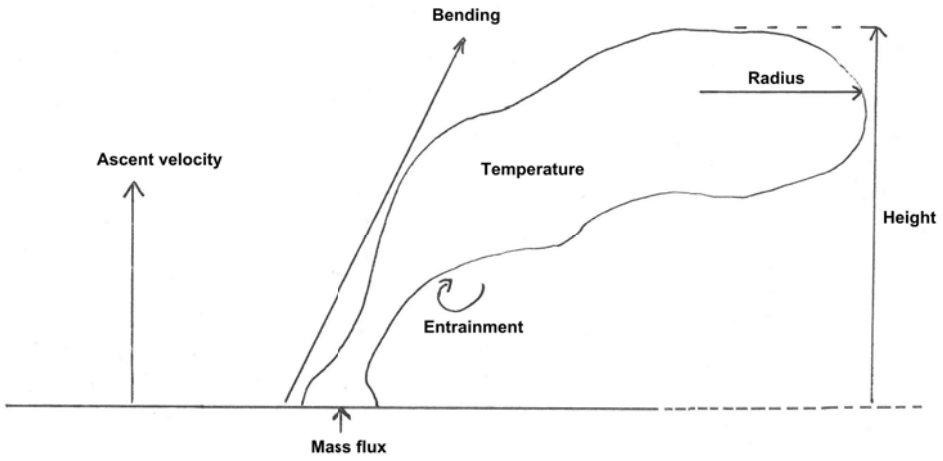

Figure 3.1: Plume parameters measurable from thermal imagery

1977]

2. Starting plumes - A steady buoyant plume has a feeder column below a bulbous form which shows signs of spreading with height. The plume front begins to form a thermal.

3. Rooted thermals - The plume front is a well formed convecting thermal with a classic mushroom-shaped form to the system.

4. Discrete thermals - The plume front and the steady plume are now detached and/or emission of the steady plume has died out. The plume is no longer fed but the thermal is still able to convect and ascend under its own buoyancy.

3.1.3 Physical model

Models have been applied, with considerable success, to describe the dynamics of Plinian plumes, but they are also applicable to less explosive events. Whereas violent eruptions pro-

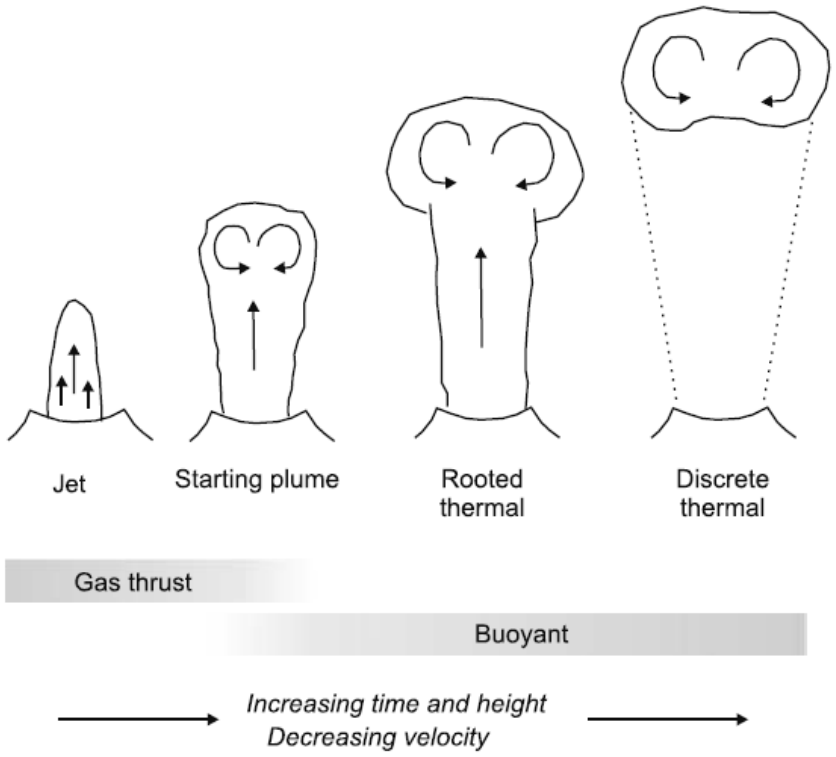

Figure 3.2: Plume morphologies resulting from discrete explosions. *Figure taken from Patrick, 2007.*

duce a large amount of very fine ash, less energetic eruptions produce much larger particles so that the potential for affecting turbulent entrainment is greater. The ascension and spread of a volcanic plume in the atmosphere is governed by the entrainment and heating of ambient air as well as the source conditions and environmental stratification [Morton et al., 1956; Woods, 1995], so that the rise height (H_o) being defined:

$$H_o \sim (2\alpha_e)^{-1/2} f_o^{1/4} N^{3/4} \tag{3.1}$$

Where α_e is the entrainment coefficient, f_0 is the buoyancy flux at the source, and N is the buoyancy frequency defined by the density stratification of the atmosphere.

Recent studies suggest that inertial particles have a large role to play in determining entrainment dynamics and that α_e depends on the buoyancy of the jet [Kaminski et al., 2005; Jessop and Jellinek, 2014]. The buoyancy term in Equation 3.1 thus need to be combined with a function describing the flow gradient, which is conventionally expressed as a Richardson number, $R_i = g' r / \bar{u}$. Here, r,$\bar{u}$ and g' are respectively the local jet radius, mean axial velocity, and gravity corrected for altitude. Throughout this study, subscript 0 refers to the value at the source, so that $\bar{u_0}$ is the initial velocity while r_0 is the vent radius. In general, $Ri \propto |Ri_0|$; thus, a proportionality coefficient (β) was defined as $Ri = \beta |Ri_0|$ [Jessop and Jellinek, 2014]. We assume our system to be under steady state conditions so that the conservation laws of volume (q), momentum (m) and buoyancy (f) can be expressed as follow:

$$\frac{dq}{dz} = 2\alpha_e m^{1/2}, \quad m\frac{dm}{dz} = g' q^2, \quad \frac{df}{dz} = -N^2 q \tag{3.2}$$

Where $q = r^2 \bar{u}$ and $m = r^2 \bar{u}^2$ [Woods, 2010], so that $r = q\sqrt{m}$ [Turner, 1962]. We differentiate this last equation over the height:

$$\frac{dr}{dz} = 2\alpha_e - \frac{\beta |Ri_0|}{2} = \tan \vartheta \tag{3.3}$$

However, this model requires input of several unconstrained key parameters which are difficult to measure, but may be provided through image processing of thermal video.

Classical models show that the entrainment of air can be used to predict the motion of the plume, and has no dependence on the vent size, geometry, or mass loading. Indeed, the

rate of entrainment of air is calculated with an equation of the general form:

$$\frac{dm_a}{dt} = \mathcal{A} u_v \alpha_e \varrho_{air} \tag{3.4}$$

where dm_a/dt is the mass flux of air into the plume, $\mathcal{A}$ is the entrainment surface area, u_v is the bulk upward velocity and ϱ_{air} is the density of air. Of these variables $\mathcal{A}$, u_v and α_e can be calculated from the thermal image but they depend on the model used to describe the plume. The Gaussian model assumes velocity to decay in a Gaussian fashion around the point of maximum upward velocity near to the center of the plume. The "top hat" model assumes that all properties, such as upward velocity, temperature and density, are constant across the plume so that they can be described by a single bulk value which is constant, horizontally, across the plume. The gaussian model usually depicts the radial profiles of these properties well [Dai et al., 1995] but the top hat approximate has also produced realistic comparisons with observed plumes [Sparks et al., 1997]. Following Patrick, [2007], we convert the visible radius (r) measured from the thermal imagery to the top hat radius (b) following:

$$\begin{aligned} &\text{for thermals:} && b = 0.9\ r \\ &\text{for steady plumes:} && b = 0.71\ r \end{aligned} \tag{3.5}$$

The conversion is dependent on the shape of the plume. Air entrainment directly controls the lateral spreading rate of the plume. Thus, the morphological distinctions are important for understanding plume dynamics. For example, discrete thermals have much greater spreading angles, and thus subjecting to greater degrees of air entrainment than jets. The air entrainment coefficient can be calculated by solving the following, plume-form-dependant, equa-

tions of Morton et al. [1956] and Turner [1962; 1973]:

$$\begin{aligned} &\text{Jet:} && \frac{db}{dh} &&= 2\,\alpha_e \\ &\text{Steady plumes:} && \frac{db}{dh} &&= \frac{6}{5}\,\alpha_e \\ &\text{Discrete thermal:} && \frac{db}{dh} &&= \alpha_e \end{aligned} \tag{3.6}$$

The evolution through time of the height and the radius of the plume allows us to calculate the air entrainment coefficient. In the review by Sparks et al. [1997], the typical top hat entrainment coefficients are

- 0.06 (for jets);
- 0.07 (for steady, buoyant plumes);
- 0.12 (for thermals at the plume front with velocities greater than 15 m s^{-1});
- 0.22 (for thermals at the plume front with velocities less than 15 m s^{-1});

Moreover, the evolution of the radius is directly linked to the evolution of the area such that $A = \pi b^2$ and the height can be used to calculate the velocity of the plume, this being the differential of altitude between two known image times. These parameters have to be converted to units of meters before use in equation 3.4. The conversion is completed by multiplying the measurement (in pixels) by pixel dimension (p_{size}) which can be calculated, following Harris, [2013], through:

$$p_{size} = \frac{2Dtan\left(\frac{-}{2}\right)}{\sin(90 - \varphi)} \tag{3.7}$$

where D is the distance to the target, β is the field of view, and φ the inclination of the acquisition system.

3.2 Plume-size study

3.2.1 How to segment volcanic plume

Our primary objective was to develop an operational algorithm capable of detecting a moving plume and parameterising its dynamics through time. The thermal camera used in this study was a forward looking infrared (FLIR), this being a FLIR Systems SC660. This camera was equipped with an internal battery and an internal memory card providing a safe and autonomous system for data acquisition. The focal length was 38 mm and the instantaneous field of view (IFOV) was 0.65 mrad. Given the slow motion of the target, frame rates over 1 Hz are more than sufficient to record the ascent dynamics. Here we recorded at 30 Hz, which corresponds to the maximum frame rate at which we can still transfer of full size frames with dimensions of 600 $\times$ 480 pixels.

However, recording at 30 Hz to avoid the loss of data forced us to consider the parameter step, this being the gap minimum between two frames to have a significant evolution in the plume. Thus, a first phase of the algorithm was to consider the differentiation ($D_{t,t-step}$) between the current frame (I_t) and the previous frame (I_{t-step}) so as to highlight the dynamic background. We applied a single level discrete 2-D wavelet transformation, using a Daubechies wavelet (db1), on the absolute value of $D_{t,t-step}$, to compute the approximation coefficient matrix [Daubechies, 1992]. The approximation coefficients are the high-scale, low-frequency components that contain much less noise than the original image and enhance the contrast, but which are around half the size of the original image. We next performed a direct reconstruction from the 2-D wavelet coefficient to obtain a reconstructed approximation

image.

From the absolute value of the reconstructed image, we computed a single threshold for the image using Otsu's method [Otsu, 1979] to obtain a partial mask of the plume. We cleaned this mask by applying a morphological opening transformation with a one pixel radius disk and removing detected elements of less than five pixels in area. We applied this mask by performing the same process with another differentiation, $D_{t,Ref}$, this being the difference between the current frame (I_t) and a reference frame recorded before the event (I_{Ref}). We summed the two masks to obtain the final differentiated mask. However, because the wavelet transformation produced an approximation image, we then performed a morphological reconstruction, i.e., we applied a repeated dilation process to the mask until its contour fitted the original image, I_t. Each successive dilation was constrained to lie underneath I_t. We cleaned the final image by removing outliers to finally compute the plume exterior contour using a Canny edge detector [Canny, 1986].

The steps of our algorithm are summarised in Figure 3.3 and highlight the efficiency of the algorithm, this being highlight by its speed of processing of around a frame per second. It also emphasises its autonomy since it does not require any user input. Finally, because it is difficult to obtain ground-truth at the natural system, we applied the algorithm to different data sets to visually validate the robustness of the technique under different environmental conditions for both natural and controlled (man-made) explosions.

3.2.2 The Euro-American data set

The first sequence used was a thermal video of the ascension of an ash plume at Santiaguito volcano (Guatemala). The Santiaguito lava dome complex is composed of four main

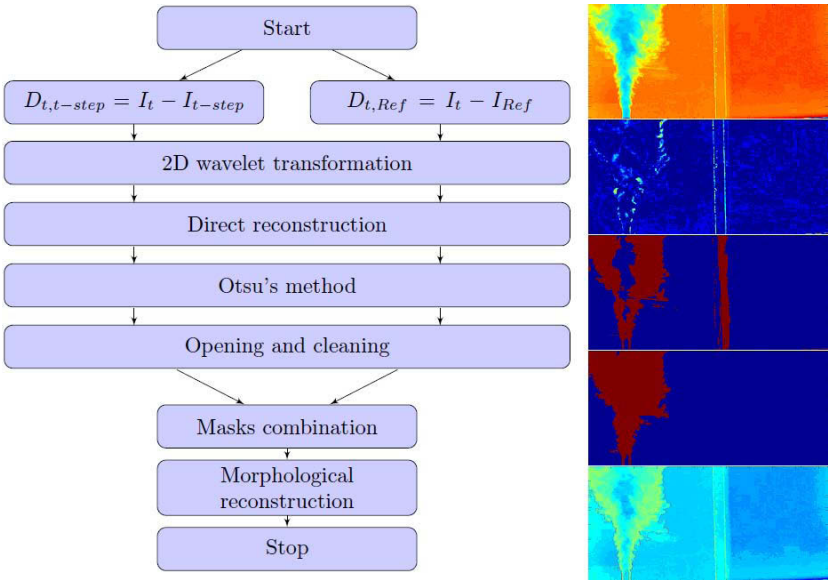

Figure 3.3: The plume tracking algorithm

centers: El Caliente, El Brujo, La Mitad et El Monje [Rose 1987; Harris et al., 2003a]. Since 1977, the Caliente vent (2 520 m asl) has been considered to be the principal vent of Santiaguito with persistent low to moderate intensity explosions occuring at a typical frequency of 1.7 explosions per hour [Rose, 1987; Sahetapy-Engel et al., 2004; 2008; Johnson et al., 2004]. These explosions produce vertical ash plumes up to 4 km height [Bluth and Rose, 2004]. The video used here was recorded in 2005 [Sahetapy-Engel and Harris, 2009] using a FLIR Systems ThermaCam^{TM} (Model S40). The images that comprise the video were 320 $\times$ 240 pixels in dimension with a field of view of 24° $\times$ 18° (IFOV is 1.3 mrad). The camera recorded at 30 frames per second and the emission was 170 s (5 100 frames) in duration. The camera was tripod mounted 4.5 km south of Caliente. Given the vent location in the image, the plume can be tracked over $\approx$1140 m. The background was composed of a homogeneous sky with low-contrast meteorological clouds, with the ground contrasting well with the plume (Figure

3.4(a. left)). A lava flow was apparent on the left-hand side of the vent, its low surface temperature meaning that the contrast with ambient ground was low [Harris et al., 2002]. The targeted plume began as a slow steady plume, then spread laterally until becoming a rooted thermal.

In the next three descriptions, the thermal camera used was a FLIR SC660 with a field of view of 24° × 18° (IFOV was 0.65 mrad). Videos were 640 × 480 pixels in dimension and were recorded at a frame rate of 30 Hz. The second video was recorded at Stromboli volcano (Italy) on 28 May 2012 [Harris et al., 2013b]. The camera was set up at Pizzo Sopra la Fossa and pointed at the North-East crater over a line of sight distance of 300 m so that the image covered a height of 94 m. Plume emission lasted 67 s (i.e. 2 000 frames). The background was a homogeneous sky and cold ground around the vent, although another puffing vent on the left of the active vent produced an unwanted hot plume (Figure 3.4(b. left)). In addition, the distance between the camera and the vent was shorter than at Santiaguito, thus the impact of heat radiated by the crater was more problematic. During plume ascent, overturn convection thermally renewed the plume surface so as to continually bring hot spots to the surface of the plume to create a heterogeneous intensity to the plume images, thus making intensity tracking difficult. Due to wind effects, the target was a bent-over plume.

The third video was recorded at an outdoor experimental facility near Buffalo, USA. During June 2014, the University at Buffalo completed experiments that used small chemical explosive charges buried in layered aggregates to simulate the effects of subsurface hydrothermal and phreatomagmatic explosions [Valentine et al., 2015]. At the same time, three more powerful blasts were performed. These released a plume of fine sand particles. The blast used to test our algorithm was that of Pad 5, Blast 4. The energy produced by the explosion was

2.30×10^6 J and the depth of the charge below the surface was 0.5 m. The camera was set up 74 m from the source so that the field of view was 23 m in height. The ambient background was composed of trees at ambient temperature, moving in the wind to create a moving background. The top of the video comprised sky that had a good contrast with the trees. On the ground, two stacks of sand were warmer than the general background due to the sunny conditions which also heated a pole present in the image. This video was the most difficult to process due to the numerous and contrasting features in the scene (Figure 3.4(c. left)). The plume, ejected by the explosion, rose quickly to 10 meters, then formed a rooted thermal before slowly moving to the right due to a weak wind.

The last video recorded with the FLIR SC660 was at an outdoor facility near Munich, Germany, where the Ludwig-Maximilians University completed large-scale ash settling experiments in June 2014 [Cimarelli et al., 2013]. Natural basaltic ash (0 – 500 μm) was released with different controlled volumetric flow rates using a shock tube system. The experiment used to test our algorithm was that of experiment #33. The sample came from Monte Rossi Scoria (Italy); it was water saturated, the sample porosity was 30 %, its volume was 29.44 cm^3 and the pressure of the decompression was 15 MPa. Due to the amount of pressure and the volume of the sample, the experiment was six frames in duration (0.2 s). The camera was set up horizontally at a distance of 4 m so that the field of view was 1.2 m height. The algorithm succeeded in performing plume detection despite the fact that the sample was colder than the background which was composed of non-moving trees and a cable (Figure 3.4(d. left)). The target was thus a cold, but very fast, jet.

Jessop and Jellinek [2014] completed indoor experiments using preparations of mixtures of fresh water and particles with different, but known, parameters such as size, density, and

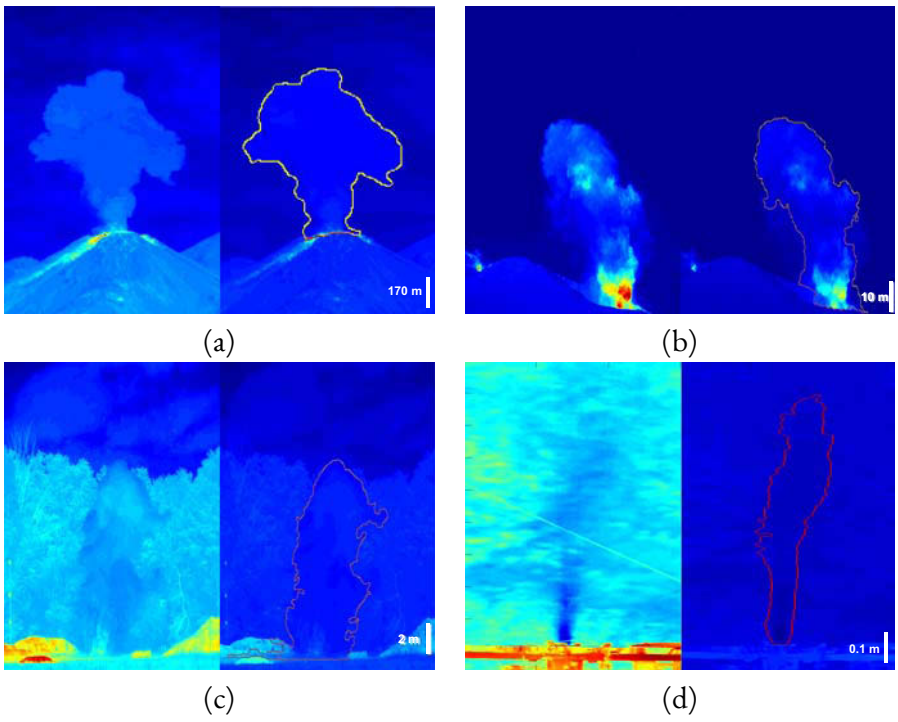

Figure 3.4: Performance of the plume segmentation algorithm when applied to videos of plumes at Santiaguito volcano (a), Stromboli volcano (b), Buffalo (c) and Munich (d)

distribution. The experiment was recorded using a digital single-lens reflex camera recording at one frame per second. The mixture was injected into a water tank (20 cm deep layer of salt water overlain by a 40 cm deep layer of freshwater) through a nozzle. The diameter and the flare angle of the nozzle were modified to represent the different vent geometries seen in natural eruptions. The experiments highlighted that the mass of the particles contribute to, and augment the angular momentum of entraining eddies, while the shape of the eddies is affected by the nozzle geometry. Following the same method, Carazzo et al. [2014] completed a similar experiment to produce a bent-over plume. To simulate the effect of the wind, they setup a carriage over the tank so that the source could be moved.

Frame	Relative Time	Height (m)	Radius (m)
500	00:00:16	117	66
1000	00:00:33	204	100
1500	00:00:50	303	148
2000	00:01:06	405	184
2500	00:01:23	485	206
3000	00:01:40	543	221
3500	00:01:56	602	241
4000	00:02:13	645	259
4500	00:02:30	645	288
5000	00:02:46	645	309

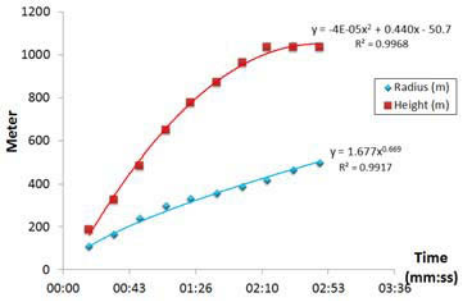

Figure 3.5: Evolution of the radius and the height of the Santiaguito plume through time.

3.2.3 Results

We begin by considering the evolution of the plume at Santiaguito (Table in Figure 3.5 left). The evolution of height with time follows a quadratic function, while the radius approximates a power function (Figure 3.5 right). Using these values and the form of equation 3.6 applied for steady plume, we calculate an average air entrainment coefficient for Santiaguito of 0.21 ± 0.05.

Now, we reiterate the process for each dataset (Table 3.1). Our results are consistent with those from Sparks et al. [1997]. We found a low air entrainment coefficient for the cold jet plume of Munich and higher values for the plumes at Santiguiato and that generated at Buffalo. Because of the quick ascent of the plume due the high pressure of the charges at Buffalo, in most of the frames considered for the calculation, the plume was already in a rooted thermal phase and had all the characteristics of a slow moving plume with a high air entrainment coefficient. At Stromboli, probably due to the strong wind and the fast movements of the plume, the air entrainment coefficient seems to be transitional between jet and steady-plume. This points out the necessity to consider the plume as a whole system to calculate these pa-

Table 3.1: Air entrainment coefficients based on the visual morphology classification approach

Location	$\alpha_e \pm$ STD	Plume type [Patrick et al., 2007]
Munich	0.03	True jet
Stromboli	0.13 ± 0.05	Transitional
Santiaguito	0.21 ± 0.05	Slow plume
Buffalo	0.28 ± 0.09	Slow plume

rameters, and thus to be far enough to record the general dynamics of the plume during its full ascent.

We note that, in our study, we used a constant radius and height for each time step t. However, the air entrainment coefficient is variable not only in time but also in altitude [Kaminski et al., 2005; Carazzo et al., 2008a; 2008b]. However, our aim was not to strictly apply geophysical models to our data sets but to use this case study as a validation of our algorithm.

3.3 Conclusion

Volcanic plumes are dangerous phenomenon which can damage aircraft and cause fall out over large populations causing widespread health and structural problems. Current simulation models are able to simulate plume behavior, but require input of unconstrained or poorly constrained parameters which are difficult to measure on site. In this study, we used a thermal camera to parameterise the plume ascent. Considering a good safety distance, plumes are slow moving targets so that an imaging frequency of one frame per second is sufficient to follow the full plume evolution through time. However, considering the current technology, a 30 Hz record is an affordable bonus which allows the algorithm to be close to real-time. This

asset strengthened due to the fact the algorithm is based on fast and effective methods such as wavelet transformations, mathematical morphologies and Otsu's method. Detection and tracking is also fully automatic and does not require any user input.

To obtain a ground-truth value to validate the algorithm we used a visual validation through a heterogeneous data set of thermal and visible videos. Two natural cases, Santiaguito and Stromboli volcanoes, were used to examine out complications due to varying site condition, and three experiments were completed to broaden the scope of dissimilarity. The different conditions were on the background (cold/warm, static/moving, homogeneous/heterogeneous, hot spots, good contrast / poor contrast), on the plume (slow/fast, bent-over, cold/warm), and on the data type (thermal/visible). The algorithm proved to be robust enough to automatically extract plume parameters such as height, width and spreading angle which can be applied to calculate air entrainment coefficient values that are consistent with the literature.

Once the graphical user interface (Fig 3.6) will be finished, we expect to test this automatic algorithm in near-real-time on a volcano so as to implement a new module to supplement the software of Valade et al. [2014] and provide a tool box for near-real time plume tracking and parameterisation for improved modeling, simulation, projection and forecast.

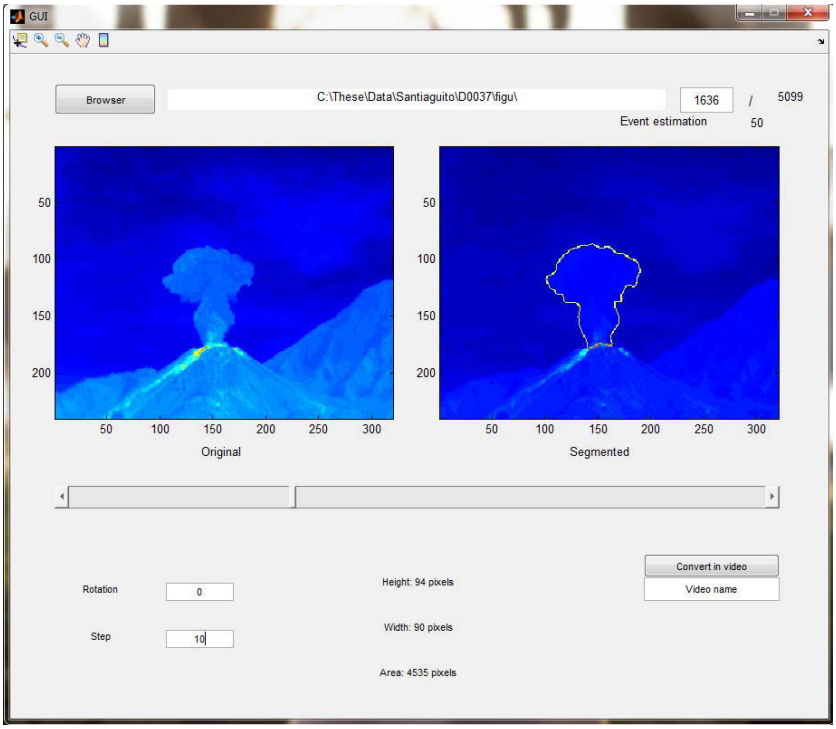

Figure 3.6: Preliminary Graphical User Interface for the Plume Tracking Algorithm

The closer you think you are, the less you'll actually see.

Now you see me - J. Daniel Atlas

4

On the transition from strombolian to fountaining activity: A thermal energy-based driver

Lava fountains, erupted as part of "Hawaiian style" events, are a relatively weak form of volcanic explosive activity by which sustained jets of molten pyroclasts and gas are ejected at mass eruption rates of 10^5-10^6 kg/s over time periods of a few hours [e.g., Mercalli, 1907; Newhall and Self, 1982; Houghton and Gonnermann, 2008]. However, they are frequently occurring events which characterise activity at basaltic centres such as Mount Etna (Italy) and Hawaii [e.g., Heliker and Mattox, 2003; Behncke et al., 2006; Stovall et al., 2010]. They are capable of feeding tephra plumes to altitudes of up to several thousand metres [e.g., Swanson et al., 1979; Vergniolle and Mangan, 2000; Wolff and Sumner, 2000; Andronico et al., 2008], causing local air fall damage and presenting a hazard to air traffic operations [e.g., Andronico et al., 2008; Calvari et al., 2011]. As a result, research and technology development has focused on understanding the trigger mechanisms for fountaining onset and the transition from milder strombolian events [e.g. Allard et al., 2005; Vergniolle and Ripepe, 2008; Calvari et al., 2011; Ganci et al., 2012; 2013; Gouhier et al., 2012; Bonaccorso et al., 2013a; 2013b], as well as methods to track event evolution in near-real time [Bonaccorso et al., 2011; Sciotto et al., 2011]. The most quantitative way to track the onset and evolution of a fountaining in near-real time is through ground-based remote sensing, including geophysical observations, volcanic plume geochemistry and thermal cameras [Ramsey and Harris, 2013; Spampinato et al., 2015]; as well as satellite-based observations if the event is sufficiently long-lasting and the satellite temporal resolution sufficiently high [Aksahal, 2013; Ganci et al., 2011; 2013].

Radiometers have proved to be a particularly powerful tool for constraining and characterising explosive eruption styles [e.g., Harris and Ripepe, 2007b; Harris et al., 2008; Sahetapy-Engel et al., 2008] and defining transitions between different explosive or degassing regimes [e.g., Marchetti and Harris, 2008; Pioli et al., 2008; Marchetti et al., 2009], as well as to ex-

amine relations between explosion style and other system parameters [e.g., Harris et al., 1996; Ripepe et al., 2002; 2005; Spampinato et al., 2015]. The advantage of radiometers is that they are low cost, and are capable of high sampling rates while keeping data rates, and processing requirements, to a minimum [e.g., Zettwoog and Tazieff, 1972; Harris et al., 2005; Murè et al., 2013]. The high sampling rates allow characterisation of explosion-related waveforms developing over time-scales of a few tenths of a second [e.g., Shimozuru, 1971; Johnson et al., 2004; Ripepe and Harris, 2008], and repeating at frequencies of just a few seconds to tens of seconds [e.g., Johnson et al., 2005; Harris and Ripepe, 2007c; Branan et al., 2008]. At the same time, the low cost of the instrument means that the radiometer can be left in unsafe areas, and loss by destruction can be absorbed and the unit replaced [Harris et al., 2003b; Ripepe et al., 2004; Spampinato et al., 2015].

We here describe just such a low-cost radiometer system installed on Mt. Etna towards the end of 2011 to track explosive activity at the SE Crater (SEC) and New SE Crater (NSEC); a system well-known for its frequent lava fountain activity [e.g., Bonaccorso et al., 2011; Calvari et al., 2011; Sciotto et al., 2011; Ganci et al., 2012; Spampinato et al., 2015 and Fig. 4.1]. Events typically begin with strombolian activity increasing in burst frequency and intensity to climax in lava fountaining [e.g., Calvari et al., 2011; Spampinato et al., 2015]. Data processing thus focused on extracting event thermal energies for discrete – albeit high frequency – explosive bursts that comprised the build-up and transition to fountaining, revealing a systematic increase in event frequency and energy as the system evolved to fountaining; crossing clear thermal energy thresholds as the system switched regimes.

Figure 4.1: Photograph showing one of the lava fountaining episodes at the Mount Etna's New South-East crater since January 2011. *Photo took by Alessandro La Spina on 12 April 2012*

4.1 Eruption-size study

4.1.1 Target

Mount Etna was selected for this study, it being currently the most active volcano on Earth in terms of lava fountain activity. Eruptions occur both at the summit (3330 m above sea level), where currently there are four degassing craters, and from its flanks. Since 1999 the SEC, and now the NSEC [Behncke et al., 2014], have been particularly active with hundreds of fountaining events being recorded through 2014.

The instrument used in this study was a thermopile-based radiometer manufactured by Optris, this being the CTfast-LT15F (Fig. 1.1.c and Appendix A.4). It offers an extremely short response time of 6 ms and temperature measurement range from -50 to 975 °C in the spectral range 8-14 μm. Here, we used a sampling rate of 50 Hz allowing acquisition of a

huge amount of data with a small memory footprint, this corresponding to 3000 values per minute which is equivalent to 24 kb per minute. The radiometer was also equipped with a small internal display allowing visualisation, in real time, of temperature in Celsius, as well as voltage output. We here use apparent temperature, uncorrected for emissivity or atmospheric effects, although emissivity should be close to one and, at this altitude, atmospheric effects will be negligible [Harris, 2013].

The radiometer was set up at the Belvedere site (EBEL, Fig. 4.2). Considering the low power draw of the radiometer (20 mA), power requirement and data logging needs were trivial [e.g., Harris et al., 2005; Murè et al., 2013]. Data were collected automatically and transmitted via telemetry to the Osservatorio Etneo of Istituto Nazionale di Geofisica e Vulcanologia [Murè et al., 2013; Spampinato et al., 2015]. This allowed near-real time tracking of the eight lava fountain events that occurred between 2012 and 28 February 2013 when EBEL station was buried by a lava flow [Spampinato et al., 2015]. To compare waveforms collected during the precursory strombolian activity, we examined thermal data for normal explosive activity at Stromboli. Stromboli's events are typically defined as a weak but persistent bursts of incandescent ballistic ejecta [e.g., Patrick et al., 2007] and ash-rich eruptions [e.g., Patrick, 2007], in events lasting a few seconds and repeating at a rate 13 events per hour [Harris and Ripepe, 2007c; Ripepe et al., 2008]. In 2012 and 2014, two campaigns were completed on Stromboli during which thermal cameras were used to acquire high-frame rate videos focusing on the vent [Bombrun et al., 2015a; 2015b] and a wider field of view to cover the whole plume [Harris et al., 2013b; Bombrun et al., 2015b]. To obtain similar values to those obtained by the radiometer at Mt. Etna, we calculated the average temperature for a conical field of view (i.e., a circle in the 2D image) through time (Fig. 4.3) during seven events.

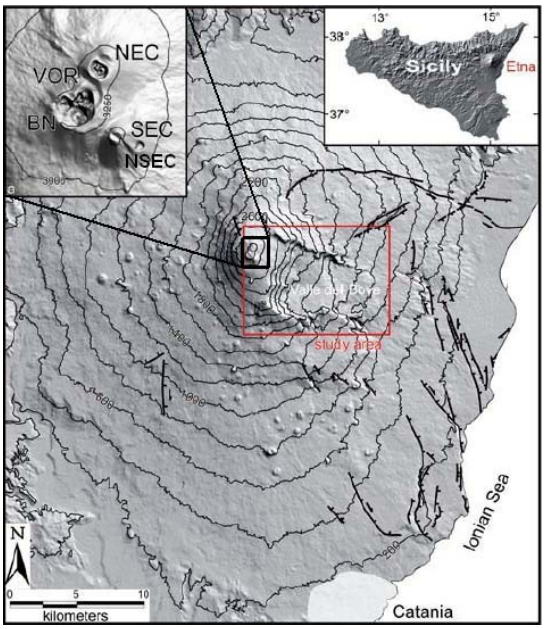

Figure 4.2: Shaded relief of Mt. Etna volcano. The red rectangle is our region of interest containing the location of Bocca Nuova (BN), Voragine (VOR), North-East Crater (NEC), South-East Crater (SEC), and the New South-East Crater (NSEC) studied here; distance from the EBEL station was ≈1km. The Valle del Bove is the zone generally affected by lava flows fed by the NSEC. *Figure taken from Behncke et al., 2014.*

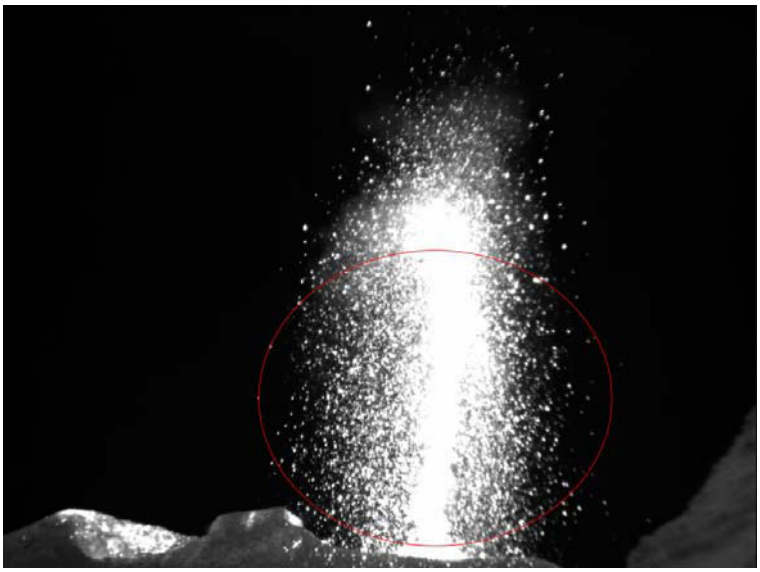

Figure 4.3: Example of the simulation of a radiometer FOV in thermal imagery (thermal image of North-East crater at Stromboli taken on 18 May 2014).

4.1.2 Algorithm

The objective of the algorithm was to temporally define a discrete explosive ("strombolian") event (Fig. 4.4). An event is composed of an ascension phase and a descent phase. Ascension begins with an initial jet that results in a waveform onset with a steep slope. An inflexion point may characterise the first burst phase, after which the apparent temperature increases more rapidly to the climax ($T_{peakMax}$). The descent phase can consist of a steadily declining trend during which emission wanes, and can be overprinted by new peaks if further bursts occur. After the event, a cooling curve is recorded, due to the effect of cooling ejecta lying on the cone outer flank between events. To define an event, we need to obtain times corresponding to each of its component phases. To do this we used an algorithm based on the work of Bertrand et al., [2011].

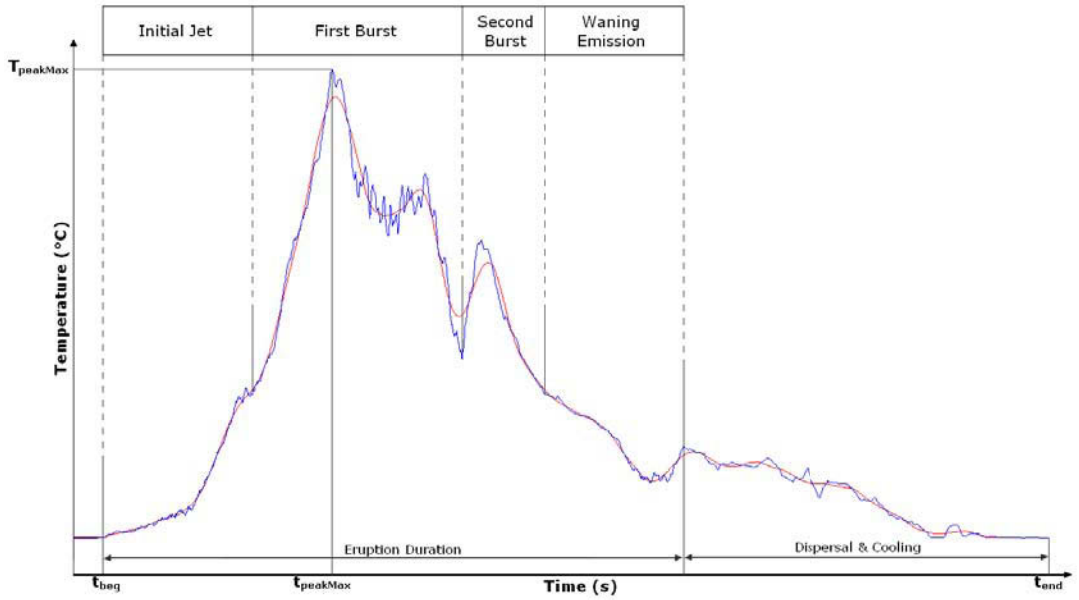

Figure 4.4: Thermal waveform of a strombolian explosion recorded on 4 March 2012 (raw data in blue, SG_o in red).

We first considered the whole data set covering the entire lava fountain episode. Due to the huge amount of data, a first step is to reduce the number of values. In the case of the whole dataset, we iterated three times resampling at 1/10 of the original sample rate during each iteration. As a result, a sequence of 1 248 000 points will be reduced to 1248 points. The beginning (t_{beg}) and the end (t_{end}) of the entire data set are known and can be extracted directly.

For individual strombolian events within each whole data set, we needed to use a 2D window of 1000 samples in size (W_{cur}) to cover linearly the data. In the case of no activity, the radiometer will still record noise, this being environmental modifications such as variable levels of solar reflection, clouds, vent puffing, and fumarolic degassing. To correct for this noise, we needed to define the noise timespan so as to calculate an average noise value. To do this, we computed the correlation coefficient (ϱ_i) and the p-Value ($pVal_i$) at time i, between

smaller windows, these being [i-50; i] and [i; i+50]. Empirically, we found that the noise timespan corresponded to W_{noise}= [k-50; k], with k being the smallest value of W_{cur} which gave ϱ_k> 0.5 and $pVal_k$< 0.05. Once the noise is removed from the data, we can detect the beginning each event, this being the point when a value switches from negative to positive, as well as the end (positive to negative). Now, to define the event temporal conditions, we begin from the time ($t_{peakMax}$) of the maximum value ($T_{peakMax}$) and descend down both sides of the waveform until the switch conditions are reached. Now the beginning (t_{beg}) and the end (t_{end}) of the event can be defined.

4.1.3 Parameter computation

The temperature at the beginning (T_{beg}) and at the end (T_{end}) of the event was trivial to extract, these being the temperatures recorded at t_{beg} and t_{end}; as was the event duration ($t_{event} = t_{end} - t_{beg}$). By considering the difference in temperature and the duration of the ascending limb ($t_{asc} = (t_{peakMax} - t_{beg})$) and the descending limb ($t_{desc} = t_{end}t_{peakMax}$), we can also compute the slope of ascent ($S_{asc} = (T_{peakMax} - T_{beg})/t_{asc}$) and descent ($S_{desc} = (T_{end} - T_{peakMax})/t_{desc}$). Next, we used a Savitzky-Golay filter [Savitzky and Golay, 1964] to smooth the data (SG_0, the oth derivative) and to estimate the derivatives of the smoothed signal (SG_i being the ith derivative). Visually, SG_0 is a perfect representation of the ideal thermal waveform associated with a normal explosion at Stromboli as described by Harris [2013] and given in Fig. 4.4. SG_1 values of zero provide us the local limits, these being either a local minimum or maximum point. We can also define the inflection point (Fig. 4.4) as the point where SG_2 changes sign. The value of the function may not reach exact zero, so we search for change in the sign to define the points surrounding the zero point of the function.

Finally, the number of SG_1 maximum points will correspond to the number of bursts (N_{peaks}).

Now we can compute the radiant exitance (M_{rad}), the radiant flux (Φ_{rad}) and the radiant energy (Q_{rad}). The Stefan-Boltzmann law allows us to express the power radiated by the target surface in terms of temperature. This law is given by :

$$M_{rad} = \varepsilon \sigma T^4 \tag{4.1}$$

where ε is the emissivity of the surface, T the temperature and σ the Stefan-Boltzmann's constant (5.670373×10^{-8} Wm^{-2} K^{-4}). Because radiant exitance is the radiant flux emitted by a surface per unit area, we integrate the radiant exitance to obtain radiant flux:

$$\Phi_{rad} = \oint_{\Sigma} M_{rad} dA_{FOV} \tag{4.2}$$

where A_{FOV} is the area of the emitting surface, i.e. the field of view (FOV) of the radiometer. Finally, radiant energy is the radiant flux integrated through time so that:

$$Q_{rad} = \int_{t_{beg}}^{t_{end}} \Phi_{rad} dt = \int_{t_{beg}}^{t_{end}} \oint_{\Sigma} \varepsilon \sigma T^4 dA_{FOV} dt \tag{4.3}$$

Now for each event, we have 12 non-independent parameters based on temporal and energetic characteristics of the waveform that can be used to define its shape, energy and temporal evolution.

4.2 Results

We begin by considering a single fountaining episode from NSEC on 4 March 2012 which lasted 12 hours. The following description is translated from INGV-OE Bollettino N°10 [2012]. The episode began at 04:29 UTC with an increase in the volcanic tremor amplitude and of strombolian event frequency and intensity. Shortly after 06:00 UTC, a lava flow spread in the direction of the western wall of Valle del Bove (Fig. 4.2), while explosive activity continued to grow with the climax and transition to fountaining occurring around 07:10 UTC.

Strombolian activity lasted 02h40, during which 278 strombolian events were detected by our radiometer system, meaning that, when time averaged, the activity rate was 110 events per hour. Emission durations ranged from 4 s to 57 s with an average of 19 s (Table 4.1). The number of bursts detected during a single event ranged from 1 to 10 with an average of 3. The radiant energy emitted by individual events ranged from 7.0×10^6 J to 4.9×10^8 J (average = 6.5×10^7 J), with the total energy released during the entire episode being 1.8×10^{10} J. Temporally, the number of peaks recorded in any one minute picked up from 2 to 4 per minute during the first hour to 8 to 15 thereafter (Fig. 4.5.a). In parallel with this, the duration of each event also ramped up (Fig. 4.5.b) and the peak temperature underwent a systematic increase (Fig. 4.5.c). Because all three of these parameters are integrated in the measure of radiant energy, the minute-by-minute plot of energy collapses to a trend whereby there is a steady increase at a rate of 5.4×10^6 J per minute over the 2.5 hour long episode (Fig. 4.5.d).

In total, we have data for seven other episodes, these being three lava fountains of 2012, i.e., 18 March, 12 April, and 24 April, and four from February 2013, i.e., those of the 19, 21,

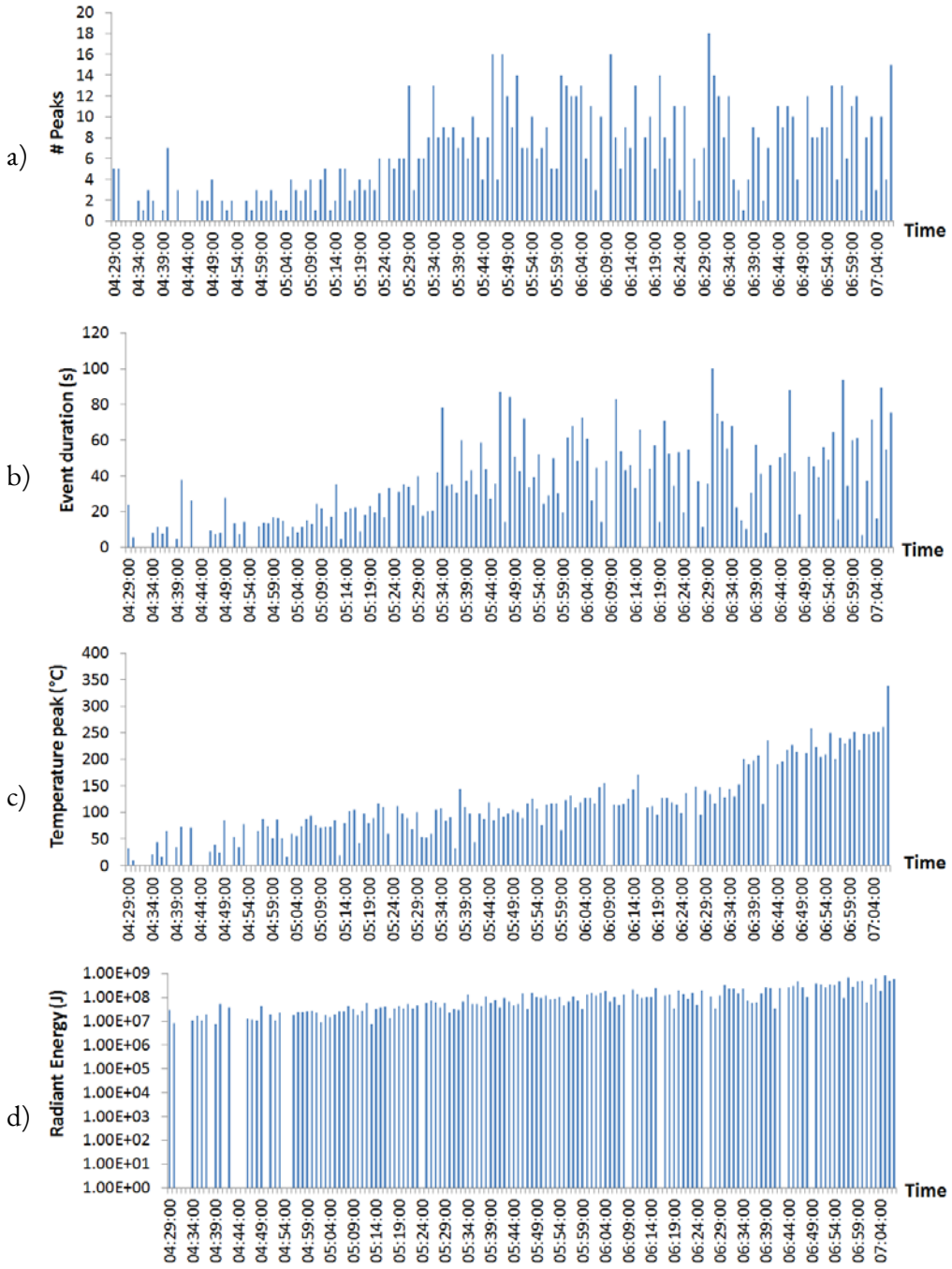

Figure 4.5: Evolution of characteristic parameters such as number of peaks (a), event duration (b), peak temperature (c), and radiant energy (d) trough time during the March 24, 2012 episode.

Table 4.1: Comparison of temporal and energy-based parameters for lava fountains recorded in 2012 and 2013.

Date	Number of strombolian events detected	Average duration (s)	Average Radiant Energy (J)	Total Radiant Energy (J)
04/03/12	278	19	6.5×10^7	1.8×10^{10}
18/03/12	650	13	5.1×10^7	1.3×10^{10}
12/04/12	257	18	7.9×10^7	5.1×10^{10}
23/04/12	389	20	2.3×10^8	8.8×10^{10}
19/02/13	66	21	1.3×10^8	1.2×10^{10}
21/02/13	85	21	2.9×10^7	1.9×10^9
23/02/13	85	20	3.5×10^7	3.0×10^9
28/02/13	116	23	3.7×10^7	4.4×10^9

23 and 28 (Appendix C.1). Together, these episodes provided us a total of 1 927 recorded events and 8 537 peaks, with event counts ranging between 66 and 650 per episode, with an average of 241 events comprising an episode. In terms of average event duration, there was little difference between each year, durations ranging from 4 to 59 s in 2012 (average = 18 s) and 4 to 55 s (average = 21 s) in 2013 (Table 4.1). However, in terms of average number of events (overview in Table 4.1) recorded the 2012 episodes had more events (393) than the 2013 episodes (88), so that the average event frequency was greater in 2012 (39 events/hr) than in 2013 (13 events/hr). Most events had radiant energies of 3.0×10^6 to 5.8×10^9 J with an average of 1.0×10^8 J. The total energy of each episode was 1.3×10^{10} J to 8.8×10^{10} J (average = 4.2×10^{10}) in 2012, and 1.9×10^9 J to 1.2×10^{10} J (average = 5.3×10^9) in 2013 (Table 4.1). At Stromboli, emission durations ranged from 25 s to 73 s with an average of 48 s. The number of bursts detected during a single event ranged from 1 to 2. The radiant energy ranged from 2.1×10^8 J to 6.0×10^8 J with an average of 3.2×10^8 J. We note that even if the duration for events at Stromboli was longer on average, the average radiant energy was weaker than at Etna.

Our analysis indicates that thermal energy is the driver of the process. To test this hypothesis, we plotted all of the data for all parameters in a three dimensional space. Visualisation of multi-dimensional data is a challenge for many domains so that an array of techniques has been proposed to allow effective data visualisation [see Oliveira and Levkowitz, 2003 for review]. Here, we used a variation of the Stochastic Neighbor Embedding method named t-SNE [van der Maaten and Hinton, 2008]. This machine learning algorithm is a nonlinear dimensionality reduction technique that visualises multi-dimensional data by giving each event a location in three-dimensional space. First, t-SNE generates a probability distribution by converting the high-dimensional Euclidean distances between data points in such way that the more data points are similar, the higher the probability of being selected. The same process is completed over the points in the low-dimensional space but using a heavy-tailed Student-t distribution instead of the Gaussian distribution used in SNE. Second, the algorithm minimises a symmetrical Kullback-Leibler divergence between the two joint probability distributions using a gradient descent method. Taken together, t-SNE separates dissimilar datapoints by means of large pairwise distances, and bring similar datapoints closer together by assigning them small pairwise distances. Visual representation of the events recorded at Mount Etna follows an approximately helicoidally path ending in a sink (Fig. 4.6.a, Fig. 4.6.b). This sink attracts all of the weak energy events; while the highest energies lie along the path. If we plot events with temporal markers (Fig. 4.6.a), events early in each episode are part of the sink; but later events form the path, the strongest events being those furthest from the sink. This supports a thermal process whereby event energy increases over six orders of magnitude during the episode. If we complete a rank order analysis of all our event energies [Pyle, 1998], we find that the lower limit to the system is at an energy of 2.9×10^6 J

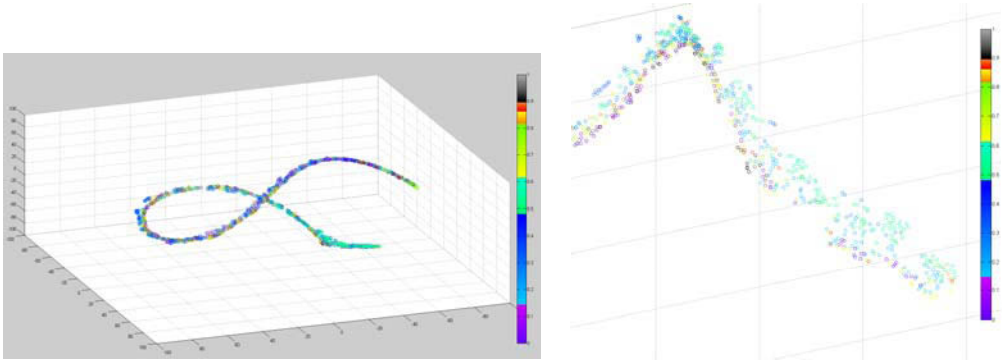

(a) (b)

Figure 4.6: Visual representation of the events recorded at Mount Etna based on the temporal and energy-based parameters. The manifold presents an approximately helicoidally shape (a) ending in a sink where all the weaker events lie(b).

(Fig. 4.7). This is the typical value of the sink events meaning that the sink is composed of many similar, but weak (the lowest energy possible), events. As we move up the path, events become stronger as we move away from the sink (Fig. 4.6.b). The threshold for an event to be just outside this field is close to 10^7 J. The rank order analysis predicts that the highest possible event we can expect is 8.1×10^9 J.

4.3 Discussion

In Fig. 4.8, we assess event shape in terms of the following normalised shape index: $(S_{asc} \quad S_{desc})/(S_{asc} + S_{desc})$. Using this index, an event waveform with little or no waning phase will have a positive value whereas an impulsive event with a long waning phase will have a negative value; a symmetric waveform will have a value of zero. We found that 1 508 (78 %) of our events had a short waxing phase with a dominant waning phase. Of the remaining events, 313 (16 %) had waning phases that were shorter than the waxing phase and 112 (6 %) were symmetric. The 313 events that had short waning phases were typically found later in

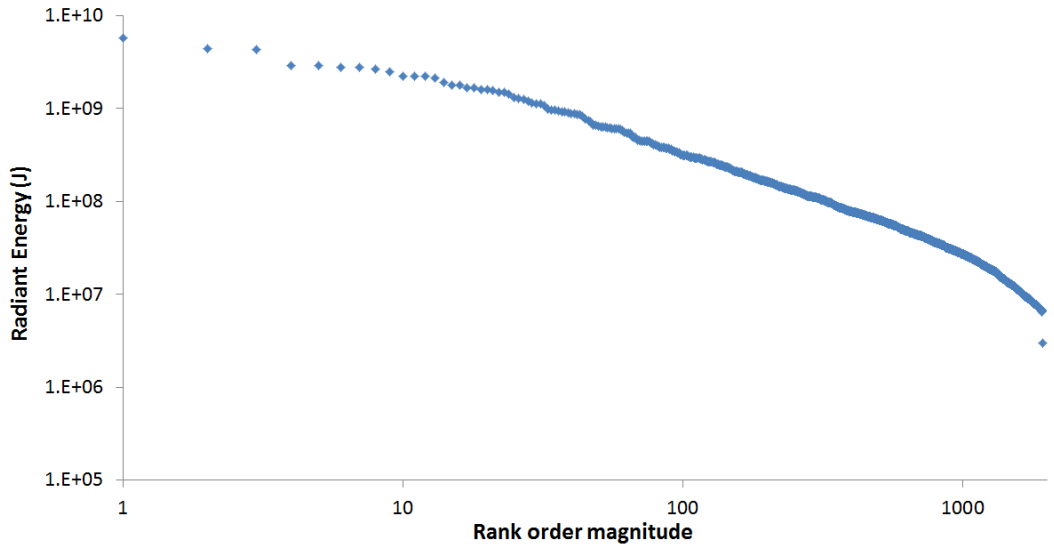

Figure 4.7: Rank order plot for all event radiances. The strongest events trend to an asymptote representative of the upper limit while the weakest events point towards the lower limit of the system.

the episode, around 3.4 hours after the beginning of the first event. This is consistent with the activity sequence commonly observed during Mount Etna's lava fountaining episodes, during which strombolian events are discrete and well separated in time at the beginning of the episode, but become more and more frequent as we approach the climax [e.g., Lautze et al., 2004; Spampinato et al., 2012]. Thus, in our case, the evolution to "short-waning" events is due to increased event frequency, so that the waxing-limb of the following event overprints, and thus prematurely terminates, the waning-limb of the preceding event. We can thus say that climax was reached after 3.4 hours during which time the event frequency, duration, peak temperature and thermal energy all steadily increased. These "strombolian" emissions are thus precursors to true lava fountains; where we find that the transition to fountaining involves crossing over a thermal energy threshold of 10^9 J, with a maximum possible event energy being 10^{10} J. Lowest energies are 10^6 J, while energies for normal explosive activity at

Stromboli (10^8 J) indicate that each eruptive episod begins with events weaker than those typically observed at Stromboli until around one hour and 15 minutes into the eruption, when the component events become thermally stronger, needing to exceed a threshold of 10^7 J to begin the path out of the sink and towards the transition to fountaining.

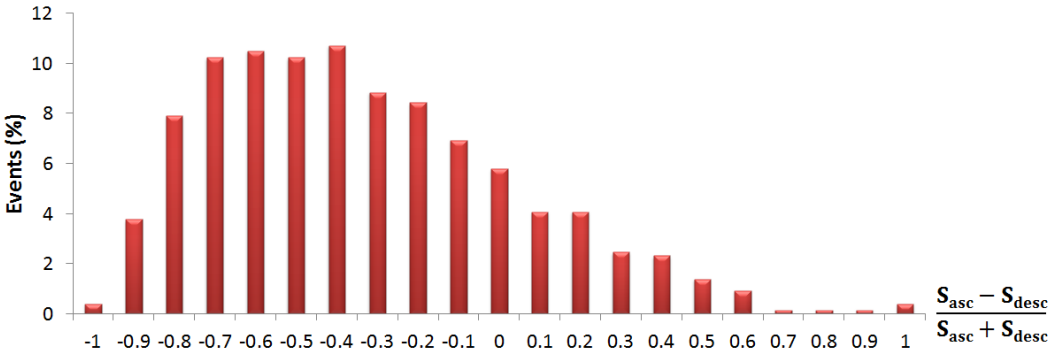

Figure 4.8: Event shape distribution of the whole data set (4 explosions in 2012 and 4 explosions from 2013). Most of the events have a short waxing phases with a dominant waning phase.

Statistically, the events of 2012 were stronger than in 2013, having an average thermal energy 5×10^7 J greater than those recorded in 2013. Although event durations were similar during the two years, the average number of events was greater in 2012, being 394 as opposed to 88 in 2013. This points to a diminishment in the magnitude and intensity of the fountaining activity between the two years. It also points to a change in style of the activity whereby, although event duration remained the same, their frequency and thermal energy diminished. This could indicate a decrease in the flux of gaseous and solid material involved in each event. Fountains at Etna have been interpreted in terms of fast ascent of gas-rich batches from the deep source [Harris and Neri, 2001] or due to collapse of foam collecting in a shallow holding chamber [Allard et al., 2005]. Either way, the amount of gas rising or accumulating prior to each event appears to have diminished, thus explaining the change in intensity, magnitude

and style, consistent with the degassing model of Vergniolle and Gaudemer [2011] to explain cycles of degassing and fire-fountaining to effusive activity. It is of note that, after this study Etna witnessed two effusive events which appear to have been heralded by a decrease in the intensity of fountaining events.

4.4 Conclusion

We developed an algorithm to obtain a robust database of 1 927 explosive events to compute radiometer-derived parameters such as event duration, duration of event waxing/waning phases, the slope for the waxing/waning phases and event radiant energy. This allows automated tracking of strombolian and fountaining events using a near-real time feed of radiometer data. While the deployment of the radiometer allows low-cost (expendable) and safe, but close, thermal observations; the thermal data allow event characterisation and tracking.

In 2012-13, for Etna, we find that fountaining episodes evolve from a steadily increasing, in terms of frequency and thermal energy, phase of strombolian events. Using our statistically robust data set we are able to define thermal thresholds that mark the transition to fountaining, as well as the point at which the energy of precursory events begins to increase away from those of the initial low energy onset events.

These energy thresholds will, though, have to be defined depending on radiometer distance or angular field of view. If, for example, we moved our radiometer back 5 km the effects of atmosphere and the presence of cold sky in the background would change the FOV-integrated radiance. However, for a stable instrument-target geometry, relative changes are a trustworthy and reliable measure of event relative energy.

That's no moon. It's a space station.

Star Wars, A New Hope - Ben Obi-Wan Kenobi

5

Space-based Hot Spot Detection

5.1 The Satellite System

5.1.1 AVHRR evolution

In 1960, the satellite TIROS-2 was launched by the National Oceanic and Atmospheric Administration (NOAA) carrying with it the first infrared radiometer into Earth orbit. Between 1960 and 2005, 34 satellites have been launched in the TIROS-NOAA series allowing continuous thermal monitoring of Earth, and being the workhorse for thermal remote sensing of volcanic hot spots [Harris, 2013]. NOAA's primary aim was to provide meteorological, as well as sea-surface reflection and temperature, data. Thus, sensor-systems on the satellite series were not designed to detect and measure volcanic hot spots. All the same, a publication occurred in 1982 [Weisnet and D'Aguanno, 1982] showing how infrared (IR) data from the Advanced Very High Resolution Radiometer (AVHRR) on NOAA-6 could be used to detect the lava lake active at Mount Erebus (Antarctica). Since then, data from AVHRR sensors flown on the NOAA-series has been used to study:

- Lava domes [Dehn et al., 2000];
- Lava lakes [Harris et al., 1999];
- Hot pyroclastic flows [Denniss et al., 1998];
- Lava flows [Harris et al., 1997d];
- Plumes [Holaske and Rose, 1996];

The latest imaging instrument flown on the NOAA-series is the AVHRR/3 as carried on NOAA-19. Complementing NOAA-18 (which carries AVHRR/2), these two polar-orbiting

Table 5.1: Abbreviations, limits to the regions of the electromagnetic spectrum within the IR waveband, and numbering system for the AVHRR channels

Division Name	Abbreviation	Wavelength	AVHRR Channel
Visible	VIS	0.4-0.7 μm	1 (0.58-0.68 μm)
Near-infrared	NIR	0.7-1.1 μm	2 (0.725-1.0 μm)
Short-wavelength infrared	SWIR	1.1-3.0 μm	3A (1.58-1.64 μm)
Mid-wavelength infrared	MIR, MWIR	3.0-5.0 μm	3B (3.55-3.93 μm)
Long-wavelength infrared	TIR, LWIR	5.0-20 μm	4 (10.30-11.30 μm) 5 (11.50-12.50 μm)

satellites are constantly circling the Earth in an almost north-south orbit, passing close to both poles. Operating as a pair, these satellites ensure that data for any region on the Earth are no more than six hours old and/or apart. The pixel instantaneous field of view is 1.3 mrad by 1.3 mrad (to give a nominal - at nadir - pixel size of 1.1 km by 1.1 km). The AVHRR/3 sensor (Appendix A.5) aimed to provide spectral radiance data for weather investigations through passively measured VIS, NIR, SWIR, MIR, and TIR emission. Thus, it has six channels which collect at-sensor radiance across the wavebands given in Table 5.1. While AVHRR data in the MIR has long been shown to be extremely sensitive to sub-pixel hot spots [Wiesnet and D'Aguanno, 1982; Dozier, 1981; Harris et al., 1995], data collected in the TIR can provide unsaturated data for hot spot parametrization [e.g., Harris, 1996].

The first algorithm designed to automatically detect hot spots in satellite data was developed by the fire-community in the mid-1980s by Flannigan and Vonder Haar [1986]; it used AVHRR data. Later, an algorithm, VAST, was developed by Harris et al., [1995] to serve as an early notice system for the onset of volcanic effusive (and sometimes also explosive) eruptions as detected by AVHRR. In their review, Steffke and Harris [2011] classified all existing algorithms used by the fire and volcanological community to detect hot spots into three classes:

1. Spatial context - Hot spots are defined by the differentiation of a pixel brightness from its surrounding pixels, i.e., anomalous pixels are different from their spatial background [e.g., Harris et al., 1995].

2. Temporal context - A hot spot is found through divergence from temporal norms, i.e., the pixel brightness is compared with all preceding values [e.g., Tramutoli, 1998].

3. Spectral character - This uses a fixed threshold to separate hot pixels from cold pixels according to their spectral properties [e.g., Wright et al., 2002].

In this study, we used IR data collected by the NOAA-19 satellite to develop an algorithm capable of disregarded saturated pixels due to non-volcanic sources, and of detecting and evaluating valid pixels associated with a volcanic event, mainly the eruption of lava flows at Mount Etna and Stromboli (Fig 5.1). Our aim was to provide a volcano hot spot data base companion to the existing MODVOLC resource [Wright et al., 2002], that runs off of Moderate Resolution Imaging Spectroradiometer (MODIS) data, for installation at AVHRR receiving stations.

5.1.2 Image Corrections

In this study, we used images provided by the NERC-NEODASS service based at the Plymouth Marine Laboratory (Plymouth, UK). Data were stored in 13 bit image files with a typical file string being "01jul14023 1etbt3.13bit", this being the channel 3 brightness temperature (bt3) image acquired on the 01 July 2014 at 02:31 UT. Information files (.info) were also provided containing image header data including:

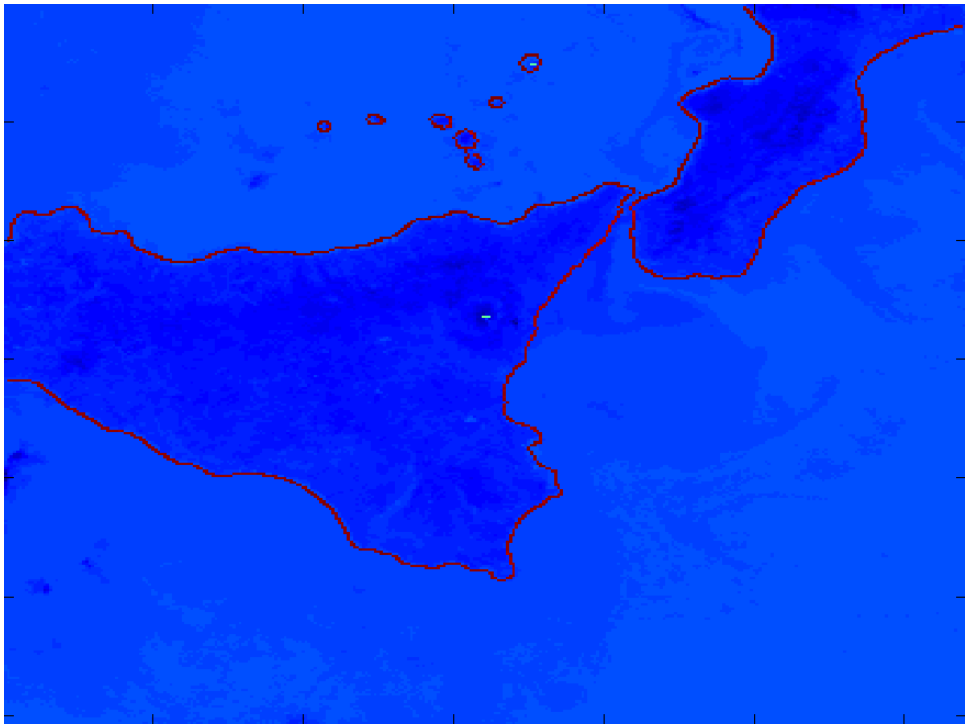

Figure 5.1: Activity at Stromboli and Mount Etna (in cyan) recorded by the AVHRR on NOAA-19 on 7 July 2014. Coasts have been highlighted in red.

- Image information (date, pass time, dimensions, bits/pixel, pixel size, latitude, and longitude);
- Satellite information (product name, satellite name, satellite direction = ascending or descending);
- Calibration coefficients (gain (G) and intercept (In)).

This information was used to convert pixel values (x) to brightness temperature by:

$$\begin{aligned} \mathrm{T} &= (\mathrm{x\ In}) + \mathrm{G} && (°\mathrm{C}) \\ \mathrm{T} &= (\mathrm{x\ In}) + \mathrm{G} + 273.15 && (\mathrm{K}) \end{aligned} \tag{5.1}$$

Next, we need to correct the atmospheric and emissivity effects. To do so, we convert each brightness temperature (T) to a spectral radiance ($\mathcal{M}$) using the Planck function:

$$\mathcal{M}(\nu, T) = c_1 \nu^3 \left[\exp(-\frac{c_2 \nu}{T}) - 1\right]^{-1} \quad (mW sr^{-1} m^{-2} cm) \tag{5.2}$$

where c_1 and c_2 are two constants respectively equal to 1.191×10^{-5} mW sr^{-1} cm^{-4} and 1.439 cm K; ν is the wavenumber (in cm^{-1}) and T is pixel brightness temperature (in K). Following the NOAA KLM user's guide Appendix D.6 [*], we set the wavenumber of channel 3B (ν_{MIR}) and channel 4 (ν_{TIR}) to 928.9 cm^{-1} and 2670 cm^{-1}, respectively . Once temperature has been converted to spectral radiance, we can correct for emissivity and atmospheric effects (transmissivity, plus the contribution of upwelling radiance in the TIR and reflection in the MIR).

[*] www.ncdc.noaa.gov/oa/pod-guide/ncdc/docs/klm/html/d/app-d6.htm

5.1.3 Lava flow parameters

The mixed pixel problem, as stated by Campbell [1986], occurs "when a pixel is composed of two or more areas that differ greatly in respect to brightness", so that the average becomes composed of "several very different values, and the single digital value that represents the pixel may not accurately represent any of the categories present.". For example, during satellite imaging of a lava flow, it cannot be assumed that pixels occupied by the lava flow are thermally pure. Considering the distance of the satellite from the ground (833-870 km in the case of NOAA), the spatial resolution is coarse and thus the pixel is a mixture of pure background and active lava flow which is, itself, an extremely heterogeneous thermal surface. To solve this problem, we used a weighted average method based on the Planck Function and which, following Marsh et al. [1980], defined the pixel-integrated spectral radiance ($\mathcal{M}$) as:

$$\mathcal{M}(\lambda, T_{int}) = p\,\mathcal{M}(\lambda, T_{lava}) + (1 - p)\mathcal{M}(\lambda, T_{amb}) \tag{5.3}$$

in which, λ is the wavelength, T_{lava} is the temperature of the high-temperature surface, T_{amb} is that of the low-temperature (or ambient) surface, T_{int} is the pixel-integrated temperature, and p is the proportion of the pixel covered by surfaces at temperature T_{lava}. By isolating the proportion p, the two-component thermal mixture model of Dozier [1980] becomes:

$$p = \frac{\mathcal{M}(\lambda, T_{int}) - \mathcal{M}(\lambda, T_{amb})}{\mathcal{M}(\lambda, T_{lava}) - \mathcal{M}(\lambda, T_{amb})} \tag{5.4}$$

Following Harris et al. [1997c], we used a T_{amb} = 0.26 °C and, because of uncertainty in the value of the lava surface, we separated the lava temperature into two cases: a "cold" case where

$T_{lava,cold}$ = 100 °C, and a "hot" case where $T_{lava,hot}$ = 500 °C. In the next step of this study, we will use the term *case* when the information does not depend on the case (e.g., p_{case} for the proportion) and proportions p_{cold} or p_{hot} if the result applies to a specific case.

Now, knowing the area of one pixel (A_{pix}) from the information file, we can estimate the area (A_{case}) covered by material at temperature $T_{lava,case}$ through A_{case}=$p_{case}A_{pix}$. Next, to calculate the time-averaged discharge rate ($TADR$), we used a best-fitting method, whereby an empirical relation was set between the total active lava area ($A_{lava,case} = \sum A_{case}$) and TADR using a coefficient (a_{case}). Following Harris [2013] we used, for the "cold" case, a_{cold}= 5.5×10^{-6} and a_{hot}= 150×10^{-6} for the "hot" case. Now, we obtain for the two cases:

$$\begin{aligned} \mathrm{TADR}_{min} &= \mathrm{a}_{cold}\, \mathrm{A}_{lava,cold} \\ \mathrm{TADR}_{max} &= \mathrm{a}_{hot}\, \mathrm{A}_{lava,hot} \end{aligned} \tag{5.5}$$

TADR is the total volume of lava emplaced over a known period of time during an eruption and is directly related to flow area and length [e.g. Walker et al., 1973; Wadge, 1978; Malin, 1980; Pieri and Baloga, 1986; Kilburn and Lopes, 1988; Pinkerton and Wilson, 1994; Harris et al., 2007]. TADR can also be used to assess the ratio between erupted and degassed mass [e.g. Francis et al., 1993; Allard et al., 1994; Ripepe et al., 2005].

5.2 Hot Spot Segmentation

5.2.1 Image Pre-processing

According to the NOAA KLM User's Guide - Section 3.1, most detectors operating in the MIR and TIR have saturation levels that are quite low, their temperature range being

Table 5.2: Potential causes of saturation in the AVHRR IR wavebands

	TIR saturated	TIR unsaturated
MIR saturated	Active lava Cloud reflection Acquisition problems (including scan edge and sun glint problems)	Active lava Lakes, water reflection Cloud reflection Wild fires
MIR unsaturated	Cloud reflection	

180-335 K (-93 - 62 °C). Thus, during hot summer days, clouds, lakes, and/or fires can saturate the pixel without being an active lava area (Table 5.2). A pre-processing phase thus needs to consider each saturated pixel following the Table 5.2 rules and convert them either in the maximal value if the pixel really is hot (T_{max}=70 °C) or the minimal value if the pixel is at an Earth surface or cloud ambient temperature (T_o=0 °C):

$$T_{sat} = \begin{cases} T_o + 273.15, & \text{if TIR saturated} \\ T_{max} + 273.15, & \text{if MIR saturated and TIR unsaturated but "hot"} \end{cases} \quad (5.6)$$

For example, we consider two acquisitions from 2 July 2014 (Figure 5.2 (a)) and 10 July 2014 (Figure 5.2 (b)). In these images, saturated pixels are in dark blue, the MIR channel is on the left, and the TIR channel is on the right. The first image pair presents a problem of acquisition i.e. a problem due to sun glint [Setzer and Verstraete, 1994] over the sea to the East and South-East of Sicily which saturates a large area of pixels in both channels (Figure 5.2 (a)). If more than the half of the image is saturated, we considered that we will not be able to achieve detection and the image is rejected. However, if saturation is not widespread, we used the algorithm to detect volcanic activity at the two targets in this sub-image, Etna and Stromboli. The second pair shows volcanic activity at Mount Etna in the MIR as well

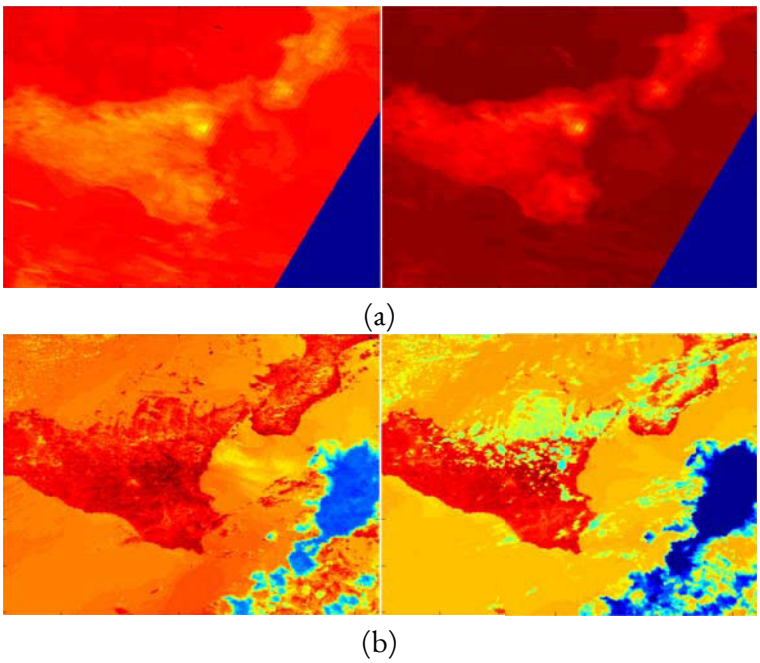

(a)

(b)

Figure 5.2: Saturated pixels (dark blue) in the MIR (left) and in the TIR (right) channels. We have saturation from problem of acquisition (sun glint)(a), and/or from volcanic activity and lakes/water reflection (b.left), cloud reflections (b.right).

as apparent hot spots due to lakes/water reflection (Figure 5.2 (b.left)). At the same time, the TIR channel is saturated due to cloud reflections (Figure 5.2 (b.right)).

5.2.2 Detection Methods

We used combinations of wavebands to enhance our detection capabilities. Several methods are known to be efficient each with pros and cons [Steffke and Harris, 2011]. Here we used a voting system that fed off of four methods. The difference in sensitivities between the MIR and TIR to a sub-pixel hot spot will mean that the pixel-integrated temperature for the hot spot pixel will be higher in the MIR than in the TIR. Thus, the subtraction of the brightness temperature in the TIR (T_{TIR}) from that in the MIR (T_{MIR}) will give a resolvable difference

($\Delta T = T_{MIR} - T_{TIR}$) usually showing up as a positive value against a flat background of near-zero values. Thus, use of ΔT is a good way of detecting thermal anomalies at active volcanoes [Harris et al., 1995], as well as for rejecting solar heated areas since they will have similarly high temperatures in both the MIR and TIR. However, differential atmospheric and reflection effects will also cause the brightness temperatures in the two wavebands to differ.

Based on this concept, the normalised thermal index (NTI) was defined by Wright et al. [2002]:

$$NTI = \frac{R_{MIR} - R_{TIR}}{R_{MIR} + R_{TIR}} \tag{5.7}$$

in which R_{MIR} and R_{TIR} are the spectral radiances in the MIR and TIR. The NTI uses the sensitivity difference to sub-pixel hot spots between the MIR and TIR, as in the ΔT method. In this case, the result is normalised so that as we move from a cold surface to a hot surface the NTI will move from -1.0 to +1.0. For example, a surface with a temperature of -50 °C will have a NTI= -0.99; however, for a 1000 °C surface, the NTI will be positive and equal to 0.91. The threshold needed for a hot spot to be detected by this method will depend on the proportion of the pixel occupied by the hot source. Harris [2013] showed that the best value for a threshold would be -0.9, but a hot spot at 250 °C will need to attain an area of 2.0×10^{-3} m² to be resolvable in a 1 km² pixel, and 1.78×10^{-4} m² at 500 °C.

To apply the next two methods, we need to define an average representation of the image (I_{av}), this being:

$$I_{av} = \left[\frac{T_{MIR} + T_{TIR}}{2}\right] + \left[\frac{R_{MIR} + R_{TIR}}{2}\right] \tag{5.8}$$

The aim is to not consider a hot spot as a high intensity pixel but as an outlier in an otherwise homogeneous area. Thus, a first method involves separating the different classes or sub-pixel

components (ground, sea, clouds, other). We applied Otsu's method [Otsu, 1979] to automatically select three thresholds based on the minimisation of intra-class variance. The original Otsu method calculates the optimum threshold so that the bi-modal histogram of the image (e.g., foreground and background) combined with the class-histogram spread (intra-class variance) is minimal. The multithresholding problem is straightforward by virtue of the discriminant criterion which is a function of these two variables, but becomes more complicated as the number of classes increases. If the thresholds selected are not good enough, i.e. the discriminant criterion does not converge, we thus need to (automatically) reduce the number of classes to two. However, active lava pixels will be in the warmer class, so that we consider every pixel over the higher threshold as a being part of the hot spot mask.

The last method is based on the mathematical morphology transformation defined by Bai and Zhou [2010]. This method improves the contrast of the image by extracting image regions which are different from their surrounding regions. The modified new white top-hat ($MNWTH$) transformation is defined by:

$$MNWTH(f) = f - min\left\{\left[(f \oplus \Delta B) \ominus B_b\right], f\right\} \tag{5.9}$$

where $\oplus$ is the dilation operator and $\ominus$ the erosion. Parameters ΔB and B_b are both square-shaped structuring elements. We apply a 21 pixel diameter box with, following Bai and Zhou [2010], which includes a three-pixel wide perimeter for definition of ΔB. That is, pixels in the central 15-pixel-wide box have values of zero, and the three-pixel-wide perimeter has values of one. Here, we applied the $MNWTH$ to I_{av} to enhance the contrast between the homogeneous background and hot spots in the image.

In most of these methods, a threshold (th) has to be defined. For the first two algoritmhs

these were defined as $th_{\Delta T}$=10 and th_{NTI}=-0.8. However, considering the histograms of ΔT and NTI (Fig 5.3 for NTI), there was a serious discrepancy between the bins.

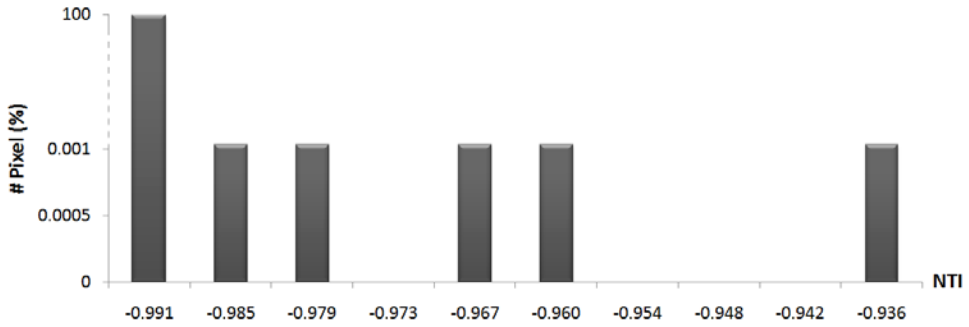

Figure 5.3: Pixel distribution in function of NTI values. Most of the pixels are in the lower bin.

Thus, we used dynamic thresholds for each method which considered pixel values (*pix*) that met the criteria $pix > m + 3 * \sigma$, in which m is the mean and σ is the standard deviation of the pixel statistics for the image. Finally, by applying a voting system, every pixel admitted by more than two of the four methods becomes part of the final hot spot mask.

Now that most of the hot spots are detected, the mask created includes pixels containing active lava or hot vents, but false detections (clouds, lakes and/or fires) can occur. To clean up the mask, we can calculate the geographical coordinates of each detected pixel so as to distinguish fires and lake reflection effects from active lava. The information file gives us both the longitude and latitude range (lon_{min}-lon_{max}; lat_{min}-lat_{max}) as well as the dimensions of the image (Im_{width}; Im_{height}). Thus, we can convert a pixel position (X_{pix}, Y_{pix}) into geographical coordinates (X_{lon}, Y_{lat}) through the cross-multiplication ($X_{lon} = lon_{min} + X_{pix} * lon_{max}$-$lon_{min}/im_{width}$; $Y_{lat} = \text{lat}_{min} - Y_{pix} * \text{lat}_{max}$-$\text{lat}_{min}/im_{height}$). This allows us to verify that the pixel detected is part of a volcanic window, this being the volcano geographical coordinates plus or minus a boundary equal to 0.10 degrees (Table 5.3).

Table 5.3: Volcano geographical coordinates

Volcano	Latitude	Longitude
Stromboli	38.70 – 38.90	15.11 – 15.31
Etna	37.65 – 37.85	14.89 – 15.09

Table 5.4: Statistical comparison between the algorithm output and (human) visual detection

Error Type	TP	FP	FN		TN
			$FN_{>300}$	FN_{OW}	
Number of pixels (%)	283 (71%)	1 (<1%)	57 (14%)	57 (14%)	6 302 002
Total	398				6 302 400

5.3 Performance

5.3.1 Visual validation

We compared the segmentation provided by the algorithm with a visual analysis completed by a human operator. Considering the large amount of data recorded by the AVHRR, the comparison was limited to the month of July 2014. The data set is, thus, composed of 74 images in two channels (MIR and TIR) each 303×320 pixels in size.

To complete a statistical analysis, we first grouped each pixel amongst four categories (Table 5.4):

1. True positive (TP) - pixels detected as "hot" by both the algorithm and the human;
2. True negative (TN) - pixels labeled as "not-hot" pixel by both methods;
3. False positive (FP) - pixels considered by the algorithm but not by the human; and
4. False negative (FN) - pixels considered "hot" by the human but not the algorithm.

False negatives can result from two sources. If the whole sub-image is rather "cold", the human may detect pixels as a result of increased contrast in the image with warm, but not volcanic, surfaces; second, if the pixel is out of the volcanic window then it will be selected by the human but not by the algorithm (Table 5.3). We thus improved our FN definition by considering only pixels that had temperatures greater than 300 K ($FN_{>300}$) and by separating the "out window" pixels (FN_{OW}), so that $FN = FN_{>300} + FN_{OW}$.

In our study, FP represents false detections that occur inside the volcanic window but which are not associated with volcanic activity. The human can easily separate them because they are spatially distance from the cluster of hot pixels at the lava flow sited. However, the algorithm accepts them because there is no spatial continuity rule. Thus, it is the hardest case to deal with and our aim is to minimise its impact. For example, we note that we can drastically reduce FN_{OW} by increasing the volcanic window by 0.15 degrees (equivalent to adding 10 pixels in each dimension); however, the number of FP exploded.

The last criterion we can examine is the similarity between the operator decisions and the algorithm results. However, considering the size of each image and the definition of TN (i.e., pixels not flagged as "hot" by either method), the total number of true negative pixels in our whole data set is over 6 billion pixels. Therefore, statistically, there is a discrepancy in number between the TN error type and the other categories. Thus, we considered an asymmetric type of binary metric for the similarity coefficient [Choi et al., 2010] and removed the TN value from the statistics. The Jaccard similarity coefficient [Jaccard, 1901] measures similarity between finite sample sets, and, in a case of binary attributes, it becomes a useful measure of the overlap within which the two data sets share their attributes. The Jaccard similarity coefficient (J) is defined as the size of the intersection of the sample sets divided by the size of

the union of the sample sets:

$$J = \frac{TP}{TP + FP + FN} \tag{5.10}$$

and, in our case, J= 71 %. On this data set from July 2014, 283 pixels (71 %) were correctly detected by both the human detection and the algorithm. Amongst the 115 remaining pixels, 57 (14 %) had temperatures over 300 K but were not detected by the algorithm, and 57 were outside of the volcanic window and, thus, were rejected by the post-processing geographical location test. Only one pixel was detected as being FP, it being due to enhanced the reflection from a ground object in the Mt. Etna window (Table 5.4). Thus, our algorithm minimises the impact of the FP detections to close to zero.

5.3.2 Robustness against saturation causes

Saturated pixels can be a result of volcanic activity, but others may be produced by other natural phenomena (Table 5.2). In this study, we assumed that these causes were independent and, thus, we processed the whole data set with the only requirement being that the majority of the image was not saturated (i.e., less than half the number of pixels were below saturation). However, although the post-processing phase cleaned the image data set up, we also wanted to filter these causes to allow the algorithm to detect wild fires or other interesting patterns (lakes, streams), whose size may be an indicator of other natural hazards such as drought or flooding.

First, we considered cloud reflections and acquisition (scan edge and sun glint) problems. In our data set, cloud reflection problems affected only one of the channels (either MIR or TIR). In the case of acquisition problem, sun glint caused a single large saturated area, and the scan edge problem resulted on an extensive, and coherent, polygonal area on one side of

the sub-image or the other.

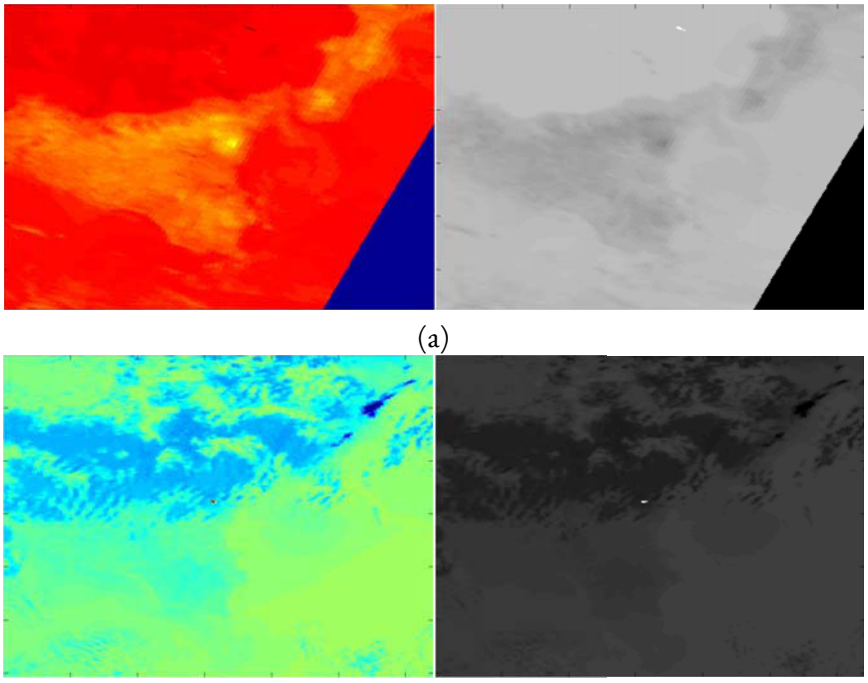

(a)

(b)

Figure 5.4: Average representation of the MIR and TIR channels (left), despite the presence of saturated pixels (in dark blue) due to problem of acquisition (a) or clouds reflection (b), the algorithm is able to detect the volcanic activity (in white on the right).

We considered two images recorded on 02 July 2014 (Figure 5.4 (a)) and 11 July 2014 (Figure 5.4 (b)). On the left, we display the I_{av} image with saturated pixels in dark blue, and the result of the detection on the right in gray scale with white pixels being pixels detected as hot spots. The first image shows the acquistion problem (Figure 5.4 (a.left)). The number of saturated pixel is less than half the total number of pixels in the image so that the algorithm processed it. Saturation occurred in both channels, thus equation 5.6 returned the minimal value, T_o, for these pixels. However, their intensities were too weak to be detected, so that the algorithm just detected the volcanic activity at Stromboli (Figure 5.4 (a.right)). The second image pair

shows volcanic activity at Mount Etna which was covered by clouds. Saturation is present only in the TIR and the volcanic activity only in the MIR. Thus, I_{av} spreads the thermal range and displays both the cloud that, once again, the equation 5.6 reduces to T_o (Figure 5.4 (b.left)), and the volcanic activity which was detected as hot spots by the algorithm (Figure 5.4 (b.right)).

The final cause of saturation which occurred in our data set was the reflection from lakes and heat emitted by wild fires. Saturation occurred mainly in the MIR and, unlike "cold" clouds, the same pixels in the TIR channel were "hot". Thus, equation 5.6 could not define the difference with volcanic activity and changed pixels to the maximum value T_{max} during the pre-processing phase. On the left hand image in Figure 5.5, recorded on 2 July 2014, the average representation I_{av} displays pixels which have the same thermal features as volcanic hot spots, and thus, are detected in the same way (Figure 5.5, right). Our algorithm is thus able

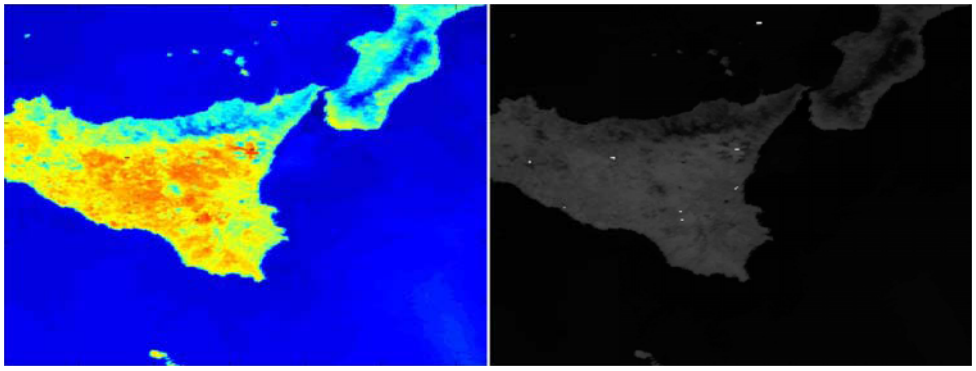

Figure 5.5: Presence of saturated pixels with same features than volcanic activity (left), so that the algorithm detected them (right)

to detect all hot spots in thermal images recorded by a satellite, and can differentiate volcanic activity from wild fires/lake reflections through a post-processing - location check - phase.

Table 5.5: Fields of data output from the MODVOLC algorithm

Field 1	Unix time of the hot-spot observation in UCT.
Field 2	Modis sensor (i.e. Terra or Aqua).
Fields 3-7	Year/Month/Day/Hour/Min time of the hot-spot observation in UCT.
Fields 8-9	Geodetic longitude and latitude of the hot-spot centre-point.
Fields 10-14	Spectral radiance (W m^{-2} sr^{-1} μm^{-1}) in the MODIS bands 21, 22, 6, 31, and 32 of the hot-spot pixel.
Fields 15-18	Satellite zenith, satellite azimuth, solar zenith, and solar azimuth of the hot-spot pixel, in degrees.
Fields 19-20	Location of the hot-spot pixel in image coordinates.
Field 21	NTI of the hot-spot pixel.
Field 22	The sun-glint angle, computed from the sun-sensor geometry data

5.3.3 MODVOLC

The MODVOLC algorithm automatically scans each image of the Earth's surface collected by the MODIS sensor carried on-board the NASA satellite [†]. The orbit of this sensor which is mounted on two satellites (Terra and Aqua) separated by six hours in time allows four hot-spot observations every day. Thus each day, for each detected hot spot, the date, time, location and intensity are recorded (Table 5.5).

Our final motivation is to install our software at NERC-NEODASS so to provide an AVHRR-parallel to MODVOLC, but only (currently) for Europe. Installation of the software at other stations would extend the coverage. Preliminary comparisons between the two algorithms have, however, highlighted temporal/spatial resolution problems which we need to be solve. For example on 2 July 2014, our algorithm detected only one weak pixel at Stromboli at 00:37 and 10 pixels at 02:19 while MODVOLC detected two pixels at Stromboli at 01:10. if comparisons in terms of energy are distorted because of the timespan between acqui-

[†] http://modis.higp.hawaii.edu/cgi-bin/modisnew.cgi

sitions (lava flow was spreading during this period), combining these temporal information can narrow down the onset times of the eruption between 01:10 and 02:19.

5.4 Future progress

We used data from the AVHRR flown on NOAA-19 satellite to detect volcanic events at Stromboli and Mount Etna. The aim was to merge accepted (and already operational) approaches with new image processing methods, such as the MNWTH and intra-class clustering, to generate a new hybrid hot spot detection method. Because AVHRR was originally designed for weather forecast and sea surface temperature purposes, the temperature ranges of the thermal channels are quite low and thus, pixels are often saturated over high temperature surfaces [Harris et al., 1995b]. However, and especially when the environment is warm (e.g. during summertime) and/or when the surface is highly reflective, saturated pixels will occur over ambient surfaces. A "cleaning" pre-processing phase can reduce the impact of these artifacts, but small highly-reflective surfaces such as lakes can have the same features in the image as a lava flow and, thus, are detected as well. We used geographical masks derived from the satellite in a post-processing phase to constrain our detection to volcanic windows and to minimise the impact of these false positives.

Finally, we tested our algorithm on data recorded over Sicily and the Aeolian Islands during July 2014. We compared the algorithm output with human segmentation as completed visually. The algorithm detected 283 hot spots pixels compared with 398 counted by the human. Statistically, we have a coefficient of similarity of 71 %. For the 115 remaining pixels, 57 were not detected by the algorithm despite having a temperature greater than 300 K, and 57 were cleaned-up by the post-processing phase, these being those human-detection cases

that were outside of the volcanic window. A larger window will reduce this impact, but will increase the risk of including non-volcanic hot spots or reflective anomalies. Our plan is to install this algorithm at the Plymouth Marine Laboratory to run in near-real time on in-coming AVHRR data so as to set it up a parallel service to MODVOLC to monitor volcanic hazards in Europe, as well as fires and water resources, using AVHRR as complement to MODIS.

6

Conclusion

Over the past 20 years, the volcanological community has come to widely accept thermal remote sensing as an operational contribution to volcano science and surveillance. The exploitation of data collected by thermal cameras as well as space- and ground-based radiometers provides a better understanding of volcanic phenomena and eruption dynamics, thus providing another approach to add to multi-disciplinary studies aimed to understanding, tracking, forecasting, mitigating and responding to eruptive crises. A major advantage is that IR equipment often resolve hot targets that haze, fog and gassy conditions obscure from the naked eye. However, analysis routines are far from being fully automated and terabytes of data remain unutilized on hard disks, waiting to be processed.

I mainly focused an developing automated methodologies for parameter extraction for explosion plumes at Strombolian systems. Their activity is relatively weak, but with a wide range of phenomena and particle sizes (plumes, lava flow, bombs, lapilli, ash) and where methods can be easily tested and then scaled to more dangerous explosive types. Amongst the numerous volcanoes with strombolian activity, several have safe areas where events can be recorded within hundreds of meters of the source and provide a reliable source of data, thus becoming outstanding natural laboratories for studying the source and dynamics of explosive emissions.

The main motivation of this thesis was to study volcanic components from ash to lava flow through thermal vision and thus, to develop *ad hoc* algorithms to allow their measurement from such a view. My first study focused on large (bomb and lapilli) vent-leaving particles. They are representative of the degree of fragmentation occurring at the source during an eruption. I used high-speed thermal camera to follow fast moving particles (> 300 m/s) for which data sets, at the beginning of this thesis, were lacking. The thermal camera was also

equipped with a magnification lens to focus on the vent and thus record particles as closer as possible to the fragmentation point. I developed an algorithm to detect pyroclastic particles, track them during their ascent, and extract parameters such as velocity, size, mass and shape. The algorithm was validated by experimental data, during which I replicated particles with hot ball-bearings. Then, I applied the algorithm on 31 eruptions recorded during two field-trips to Stromboli in 2012 and 2014. The algorithm was able to extract parameters for 83 000 particles generating a statistically robust database. Finally, these output strengthen support for a model suggestive of the presence of a cap at the head of the magma column during pyroclastic-dominated explosions, and its absence during gas-dominated events.

The second project dealt with volcanic plumes of finer (ash) particles. Such emissions are dangerous phenomenon for both human health and transportation so that reliable models to predict their evolution need to be initialized. Plume behavior is influenced by several environmental variables which are difficult to constrain, especially through direct sampling. Here, I developed an interface to automatically follow volcanic plume ascent in near-real time, and to extract parameters such as height, width, velocity, and spreading angle. I validated the robustness of the algorithm on natural cases at Santiaguito and Stromboli, and on experiments completed at Munich, Buffalo and Paris. These sequences were chosen to cover a maximum spread of environmental conditions (wind, warm/cold, clouds, trees) and plume morphologies (jet, starting plume, rooted and discrete thermal).

In the third investigation, I was interested in the transient process during lava fountain episodes. Those episodes studied began with milder strombolian events which continuously increased in energy until climax was reached, producing major plumes (i.e., hazard was maximised). A lava fountain episode can be feed during several days so that continuous monitor-

ing is easier with a permanent station. However, the very real threat of destruction of near-vent installation by the lava flow inundation resulting of lava fountain episodes, suggests the use of low cost material would be beneficial. Here, I used a cheap radiometer setup at Mount Etna which recorded the lava fountain activity of the New South-East crater. INGV Catania provided us data for eight episodes occurring between 2012 and 28 February 2013. The objective was to analyse thermal waveforms recorded by the radiometer, extract every strombolian event during the transient phase and to characterise them in terms of energy. The algorithm detected 1 927 events and extracted parameters such as event duration, waxing/waning slopes, and radiant energy. Finally, using dimensionality reduction, I observed the energies defining a 3D-path to the highest energy (i.e., the climax) which allowed us to define thermal thresholds that mark the beginning of the transient phase and the transition to fountaining activity.

The last project tackled lava flows, resulting from strombolian and fountaining activity, as seen from space. Latest satellite systems, such as AVHRR/3 on the NOAA-series, able to record radiance information are use in detecting and tracking event evolution. However, this type of satellite-sensor system was originally designed for weather purposes so that the thermal channels have saturation levels that are quite low. As a result, saturated pixels are widespread, especially during hot periods of the year, making the task of automatic hot spot detection difficult. In this study, I investigated the possible improvements to existing methods for volcanic activity detection through use of satellite thermal images with widespread saturation. Plymouth Marine Laboratory provided data acquired for the month of July 2014, when a strombolian vent on the outer flan of the Bocca Nuova fed a series of lava flows. I implemented two methods, the MNWTH approach - as used in the first project since the aim was similar, i.e. to detect small pixel-sized targets, and a second based on Otsu's method. I

also changed existing methods by define dynamic thresholds to improve the flexibility of detection. The algorithm results for July 2014 showed 71 % of similarity with human (manual) classification. Saturated pixels were correctly classified during the process except those with features similar to those of saturated volcanic pixels, such as lake reflection.

This thesis presented several approaches to detect and track different dynamic volcanic targets in thermal data. Thinking beyond algorithmic, this work only scratches the surface of strombolian activity mechanisms. Future prospects for each project are detailed individually in the different chapters. Mainly, they need to be made more user-friendly and to be developed by a larger community which is not limited to volcanology. Indeed, the problematics are similar in many domains (astronomy, oceanology) where thermal remote sensing is soaring but data analysis is still done manually. Studies such as this help to demonstrate how image processing and thermal remote sensing can be used in symbiosis to advance scientific research.

A

Equipment Technical Specifications

A.1 FLIR SC655 Camera Technical specifications

FLIR SC655 Technical Specifications

Imaging and optical data	
Field of view (FOV)	25° x 18.8°
Minimum focus distance	0.4 m
Focal Length	24.5 mm
Spatial resolution (IFOV)	0.69 mrad
Lens identification	Automatic
F-number	1.0
Thermal sensitivity/ NETD	<0.05°C @ + 30°C/ 50 mK
Image frequency	50 Hz
Focus	Automatic or manual (built in motor)
Detector data	
Detector type	Focal Plane Array (FPA), uncooled microbolometer
Spectral range	7.5–13 µm
IR resolution	640 × 480 pixels
Detector pitch	17 µm
Detector time constant	Typical 8 ms
Measurement	
Object temperature range	-20°C to +150°C 0°C to +650°C
Accuracy	±2°C or ±2% of reading
Measurement analysis	
Atmosphere transmission correction	Automatic, based on inputs for distance, atmospherictemperature and relative humidity
Optics transmission correction	Automatic, based on signals from internal sensors
Emissivity correction	Variable from 0.01 to 1.0
Reflected apparent temperature correction	Automatic, based on input of reflected temperature
External optics / windows correction	Automatic, based on input of optics / window transmission and temperature
Measurement corrections	Global object parameters
USB	
USB	Control and image
USB, standard	USB 2 HS
USB, connector type	USB Mini-B
USB, communication	TCP/IP socket-based FLIR proprietary
USB, image streaming	16-bit 640 x 480 pixels @ 25Hz 16-bit 640 x 240 pixels @ 50Hz 16-bit 640 x 120 pixels @ 100Hz - Signal linear - Temperature linear - Radiometric
USB, protocols	TCP, UDP, SNTP, RTSP, RTP, HTTP, ICMP, IGMP, ftp, SMTP, SMB (CIFS), DHCP, MDNS (Bonjour), uPnP
Ethernet	
Ethernet	Control and image
Ethernet, type	Gigabit Ethernet
Ethernet, standard	IEEE 802.3
Ethernet, connector type	RJ-45
Ethernet, communication	TCP/IP socket-based FLIR proprietary and GenICam protocol
Ethernet, image streaming	16-bit 640 × 480 pixels @ 50 Hz 16-bit 640 × 240 pixels @ 100 Hz 16-bit 640 × 120 pixels @ 200 Hz - Signal linear - Temperature linear - Radiometric GigE Vision and GenICam compatible
Ethernet, protocols	TCP, UDP, SNTP, RTSP, RTP, HTTP, ICMP, IGMP, ftp, SMTP, SMB (CIFS), DHCP, MDNS (Bonjour), uPnP

Digital input / output	
Digital input, purpose	Image tag (start, stop, general), Image flow ctrl.(Stream on/off), Input ext. device (programmatically read)
Digital input	2 opto-isolated, 10-30 VDC
Digital output, purpose	Output to ext. device (programmatically set)
Digital output	2 opto-isolated, 10-30 VDC, max 100 mA
Digital I/O, isolation voltage	500 VRMS
Digital I/O, supply voltage	12/24 VDC, max 200 mA
Digital I/O, connector type	6-pole jackable screw terminal
Power system	
External power operation	12/24 VDC, 24W absolute max
External power, connector type	2-pole jackable screw terminal
Voltage	Allowed range 10-30 VDC
Environmental data	
Operating temperature range	-15°C to +50°C
Storage temperature range	-40°C to +70°C
Humidity (operating and storage)	IEC 60068-2-30/24 h 95% relative humidity +25°C to +40°C
EMC	• EN 61000-6-2:2001 (Immunity) • EN 61000-6-3:2001 (Emission) • FCC 47 CFR Part 15 Class B (Emission)
Encapsulation	IP 30 (IEC 60529)
Bump	25 g (IEC 60068-2-29)
Vibration	2 g (IEC 60068-2-6)
Physical data	
Weight	0.7 kg
Camera size (L x W x H)	216 x 73 x 75 mm
Tripod mounting	UNC1/4"-20 (on three sides)
Base mounting	2 x M4 thread mounting holes (on three sides)
Housing material	Aluminium

Scope of delivery
Hard transport case or cardboard box
Infrared camera with lens
Calibration certificate
Ethernet™ cable
Mains cable
Power cable, pig-tailed
Power supply
Printed Getting Started Guide
Printed Important Information Guide
USB cable
User documentation CD-ROM
Utility CD-ROM
Warranty extension card or Registration card
Supplies & Accessories
High temp option +300°C to 2000°C (+572°F to 3632°F) for FLIR SC645/SC655
Power supply for A/SC3XX and A/SC6XX
Power cord EU
Power cord US
Power cord UK
USB cable Std A <-> Mini-B, 2 m/6.6 ft.
Hard transport case for A/SC3XX and A/SC6XX series T197038 ThermoVision™
System Developers Kit Ver. 2.6
FLIR ResearchIR 1.2 T197453L5 FLIR ResearchIR 1.2, 5 user licenses
FLIR ResearchIR 1.2, 10 user licenses
FLIR QuickPlot 1.2 T197454L5 FLIR QuickPlot 1.2, 5 user licenses
FLIR QuickPlot 1.2, 10 user licenses

Asia Pacific Headquarter Hong Kong
FLIR Systems Co Ltd.
Room 1613 – 16, Tower 2
Grand Central Plaza
138 Shatin Rural Committee
Road, N.T, Hong Kong
Tel: +852 2792 8955
Fax: +852 2792 8952
Email: flir@flir.com.hk

China Head Office - Shanghai
FLIR Systems (Shanghai) Co., Ltd
Tel: +86 21 5169 7628
Fax: +86 21 5466 0289
e-mail: info@flir.cn

Japan Office - Tokyo
FLIR Systems Japan K.K.
Tel: +81 3 6277 5681
Fax: +81 3 6277 5682
e-mail: info@flir.jp

Korea Office - Seoul
FLIR Systems Korea Co., Ltd
Tel: +82 2 565 2714
Fax: +82 2 565 2718
e-mail: sales@flirkorea.com

Taiwan Representative Office
Tel: +886 2 27579862
Fax: +886 2 27576723
e-Mail: flir@flir.com.hk

India Representative Office
Tel: +91 11 4606 7100
Fax: +91 11 4606 7110
e-mail: flir@flir.com.hk

FLIR®

www.flir.com/thg

100930 SC655 datasheet_en

A.2 Lens T198166 Technical specifications

Technical Data

IR lens, f=88.9 mm with case and T6xx support (7°)

Part number:
T198166

March 29, 2012, 01:25 AM

Technical data	
Field of view (FOV)	7° x 5.3° (8.7° diagonally)
Minimum focus distance	2.0 m (6.6 ft.)
Focal length	88.9 mm (3.5 in.)
Spatial resolution (IFOV)	0.19 mrad
Lens identification	Automatic
F-number	1.3
Number of lenses	3 (3 asph)
MTF @ 70% of FOV	Normal requirements (52%)
Distortion	3%
Weight	0.77 kg (0.70 lb.)
Weight, lens	0.71 kg (1.57 lb.)
Size (L x D)	96 x 126 mm (3.78 x 4.96 in.), excluding support
Front lens diameter	96 mm (3.78 in.)

Shipping information

- Lens
- Lens case
- Front lens cap
- Rear lens cap
- Mounting support
- Lens mounting instructions

A.3 FLIR SC660 Camera Technical specifications

FLIR SC660 Technical Specifications

Imaging and optical data	
Field of view (FOV) / Minimum focus distance	24° × 18° / 0.3 m
Spatial resolution (IFOV)	0.65 mrad
Thermal sensitivity / NETD	<30 mK @ +30°C
Image frequency	30 Hz (60/120 Hz with windowing)
Focus	Automatic (one shot or follow the laserspot) or manual (electric or on the lens)
Zoom	1–8× continuous, digital zoom, including panning
Focal Plane Array (FPA) / Spectral range	Uncooled microbolometer / 7.5–13 µm
IR resolution	640 × 480 pixels
Image presentation	
Display	Built-in widescreen, 5.6 in. LCD, 1024 × 600 pixels
Viewfinder	Built-in, tiltable LCD, 800 × 600 pixels
Automatic image adjustment	Continuous / manual; linear or histogram based
Manual image adjustment	Level/span / max / min
Contrast optimization	Automatic, adjustable DDE
Image modes	IR-image, visual image, thermal fusion, picture in picture, thumbnail gallery
Reference image	Shown together with live IR image
Measurement	
Temperature range	–40°C to +1500°C
Accuracy	±1°C or ±1% of reading for limited temperature range, ±2°C or ±2% of reading
Measurement analysis	
Spotmeter	10
Area	5 boxes or circles with max. / min. / average
Automatic hot / cold detection	Max / Min temp. value and position shown within box, circle or on a line
Isotherm	2 with above / below / interval
Profile	1 live line (horizontal or vertical)
Difference temperature	Delta temperature between measurement functions or reference temperature
Reference temperature	Manually set or captured from any measurement function
Emissivity correction	Variable from 0.01 to 1.0 or selected from editable materials list
Measurement corrections	Reflected temperature, optics transmission, atmospheric transmission and external optics
Measurement function alarm	Audible/visual alarms (above / below) on any selected measurement function
Humidity alarm	1 humidity alarm, including dew point alarm
Insulation alarm	1 insulation alarm
Set-up	
Set-up commands	Configurable measurement tools menu; configure information to be shown in image; 2 Programmable buttons; user profiles; local adaptation of units, language, date and time formats
Storage of images	
Image storage	Standard JPEG, including measurement data, on memory card Built-in RAM for burst recording
Image storage mode	IR / visual images; simultaneous storage of IR and visual images Visual image is automatically associated with corresponding IR image
Periodic image storage	Every 10 seconds up to 24 hours
Panorama	For creating panorama images in FLIR Reporter Building software
Image annotations	
Voice	60 seconds stored with the image
Text	Predefined text or free text from PDA (via IrDA) stored with the image
Image marker	4 on IR or visual image
GPS	Location data automatically added to every image from built-in GPS
Video recording and streaming	
Radiometric IR-video recording	Real-time to built-in RAM, transferable to memory card.
Radiometric IR-video streaming	Real-time full dynamic to PC using FireWire 30 Hz or 60/120 Hz with windowing using FLIR ResearchIR
Non-radiometric IR-video recording	MPEG-4 to memory card
Non-radiometric IR-video streaming	MPEG-4 to PC using USB or WLAN (optional)
Digital camera	
Built-in digital camera	3.2 Mpixel, auto focus, and video lamp
Laser pointer	
Laser	Activated by dedicated button
Laser mode	Auto Focus/Level/Spotmeter
Laser alignment	Position is automatic displayed on the IR image
Data communication interfaces	
Interfaces	USB-mini, USB-A, IrDA, composite video, headset connection
Power system	
Battery	Li Ion, 3 hours operating time
Charging system	In camera (AC adapter or 12 V from a vehicle) or 2-bay charger
Power management	Automatic shutdown and sleep mode (user selectable)
Environmental data	
Operating temperature range	–15°C to +50°C
Storage temperature range	–40°C to +70°C
Humidity (operating and storage)	IEC 68-2-30/24 h 95% relative humidity +25°C to +40°C
Encapsulation	IP 54 (IEC 60529)
Bump	25 g (IEC 60068-2-29)
Vibration	2 g (IEC 60068-2-6)
Physical data	
Camera weight, incl. lens and battery	1.8 kg
Cameras size, incl. lens (L × W × H)	299 × 144 × 147 mm
Tripod mounting	UNC ¼"-20

Camera includes:
Hard transport case
Infrared camera with lens
Battery (2 ea., one inserted in camera, one outside camera)
Battery charger
Calibration certificate
FLIR QuickReport™ PC software CD-ROM
FireWire cable, 4/6
FireWire cable, 6/6
Headset
Lens cap (mounted on lens)
Lens cap (2 ea.)
Mains cable
Memory card-to-USB adapter
Memory card with adapter
Power supply
Printed Getting Started Guide
Shoulder strap
USB cable
User documentation CD-ROM
Video cable
Warranty extension card or Registration card
Supplies & Accessories
Close-up IR lens 0.5X, f = 75 mm (fits 24° IR lens) for ThermaCAM and FLIR 600 series
IR lens f = 76 mm, 12°, incl. case for FLIR 600 series
IR lens, f = 131 mm, 7°, incl. case for FLIR 600 series
IR lens f = 19 mm, 45°, incl. case for FLIR 600 series
IR lens f = 38 mm, 24°, incl. case for FLIR 600 series
Macro lens 1x (25 um) with case
High temperature option +2000°C
High temperature option +1500°C
Battery
Battery charger, incl. power supply and cable
Battery charger, incl. power supply and cable
Battery charger, incl. power supply and cable
Battery charger, incl. power supply with multi plugs
Power supply, incl. multi plugs
SD memory card, 1 GB
Adapter, SD memory card to USB
Memory card micro-SD with adapters
USB cable Std A <-> Mini-B, 2 m
FireWire cable 6/6, 2.0 m
FireWire cable 4/6, 2.0 m
Video cable, RCA <-> RCA, 2.0 m
Cigarette lighter adapter kit, 12 VDC, 1.2 m
Hard transport case for FLIR B/P/SC640
Headset, 3.5 mm plug
Remote Control Unit
FLIR Reporter Ver. 8.3 Professional (Sec. device)
FLIR Reporter Ver. 8.3 Professional
FLIR Reporter Ver. 8.3 Standard (Sec. device)
FLIR Reporter Ver. 8.3 Standard
FLIR BuildIR
FLIR Reporter Ver. 8.5 Standard
FLIR Reporter Ver. 8.5 Professional
Cover Visual Camera mkII

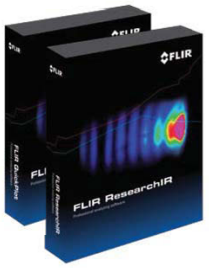

Optional softwares for R&D requirements

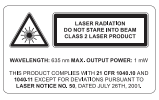

FLIR Systems Australia Pty Ltd
10 Business Park Drive
Notting Hill VIC 3168
Ph: (03) 9550 2800
Fax: (03) 9558 9853
info@flir.com.au
www.flir.com.au

A.4 CTfast-LT15F Radiometer Technical specifications

More Precision. optris

optris® CTfast

Precise noncontact temperature measurement
from -50 to 975°C

FEATURES

- One of the smallest infrared sensors worldwide with extrem short response time down to 6 ms (90 % signal)
- Fast analog output (0/4 - 20 mA, 0 - 5/10 V) with smart real time data processing
- Instant digital 0/10 V output with a response time of 4 ms (50% signal)
- Continuous process monitoring with an unchoppered sensor system
  Note: Conventional fast pyroelectrical infrared sensors with mechanical chopper see processes only part of the time
- Easy to assemble in multiple arrays for line scanning of small and fast objects (hot spot detection) using a RS485 bus communication
- Rugged up to 120°C ambient temperature without cooling

General specifications	
Environmental rating	IP 65 (NEMA-4)
Ambient temperature	sensing head: -20 - 120°C electronics: 0 - 85°C
Storage temperature	sensing head: -40 - 120°C electronics: -40 - 85°C
Relative humidity	10 - 95%, non condensing
Vibration (sensor)	IEC 68-2-6: 3 G, 11 - 200 Hz, any axis
Shock (sensor)	IEC 68-2-27: 50 G, 11 ms, any axis
Weight	sensing head 40 g electronics 420 g
Electrical specifications	
Analog output	0/4 - 20 mA, 0 - 5/10 V or thermocouple J, K
Alarm output	Open - collector (24V / 50mA)
Digital output	0/10 V (10 mA) optional: relay: 2 x 60 V DC/42 V AC; 0.4 A; optically isolated
Digital interface (optional)	USB, RS232 or RS485 , CAN, Profibus DP, Ethernet
Output impedances	mA max. 500 Ω (with 8 - 36 V DC) mV min. 100 kΩ load impedance thermocouple 20 Ω
Inputs	programmable functional inputs for external emissivity adjustment, ambient temperature compensation, trigger (reset of hold functions)
Cable length	1 m (standard), 3 m, 8 m, 15 m
Current draw	max. 100 mA
Power supply	8 - 36 V DC

Measurement specifications	
Temperature range (scalable via programming keys or software)	-50°C bis 975°C
Spectral range	8 - 14 µm
Optical resolution (90% energy)	LT15F 15:1
	LT25F 25:1
System accuracy (at ambient temperature 23 ±5°C	±1% oder ±2°C[1), 2)]
Repeatability (at ambient temperature 23 ±5°C)	±0.75% oder ±0.75°C[1), 2)]
Temperature resolution (NETD)	LT15F 0.2 K[2), 3)]
	LT25F 0.4 K[2), 3)]
Response time[4)]	analog output (90%): LT15F 9 ms LT25F 6 ms
	digital output (50%): LT15F 4 ms LT25F 3 ms
Emissivity/Gain (adjustable via programming keys or software)	0.100 - 1.100
Transmissivity/Gain (adjustable via programming keys or software)	0.100 - 1.100
Signal processing (parameter adjustable via programming keys or software, respectively)	peak hold, valley hold, average; extended hold function with threshold and hysteresis

[1)] whichever is greater with dynamic noise compression
[2)] at object temperatures ≥ 20°C
[3)] at time constant 100 ms with smart averaging and T_{Obj} 25°C
[4)] with dynamic adaption at low signal levels

A.5 AVHRR/3 Technical specifications

GEOSPATIAL SYSTEMS

POES AVHRR/3

ITT EXELIS

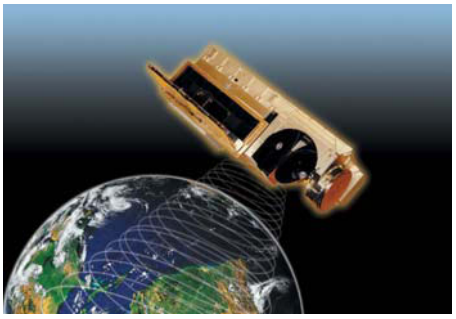

INTERNALLY RECOGNIZED AS THE OPERATIONAL IMAGER FOR GLOBAL WEATHER DATA

The Advanced Very High Resolution Radiometer (AVHRR) from ITT Exelis, flies on all NOAA Polar-orbiting Operational Environmental Satellites (POES). The third generation AVHRR has resulted in improvements in performance and operational capabilities, and improved spectral performance: low light energy detection, snow/ice discrimination, forest fire detection, sea surface temperature, and global vegetation index.

SIX-CHANNELS ENHANCES IMAGERY

The AVHRR/3 sensor is a six-channel imaging radiometer that detects energy in the visible and infrared portions of the electromagnetic spectrum. It measures reflected solar and radiated thermal energy from the land, clouds, sea and the atmosphere. The information collected is used as the primary source for global updates of meteorological data and is a vital tool used by scientists and many others to determine environmental changes that effect everyone on earth.

KEY FEATURES	
Application	Operational atmospheric and surface imagery from low earth orbit
Satellites	NOAA 's: K,L,M,N, and N'; Metop-1; Metop-2; Metop-3
Orbit	Low earth orbit @ 833 km (450 miles)
Technology	Continuously rotating (360 rpm) crosstrack scanner with multiband relay optics and continuous internal thermal calibration
Aperture	20.3 cm (8 inches)
Spatial Resolution	1.1 km (1310 microradians) in all channels
Channel Registration	Better than 100 microradians
Sensitivity	Ch 1 and Ch 2 – 9:1 S/N for 0.5% Albedo Ch 3A – 20:1 S/N for 0.5% Albedo Ch 3B, Ch 4, and Ch 5 – <0.12°K at 300°K Scene Temperature
Detector Cooling	2-stage passively cooled radiator (controlled to 105°K)
Detectors	Photoconductive HgCdTe, Photovoltaic InGaAs, InSb and Silicon

GEOSPATIAL SYSTEMS

POES AVHRR/3

SPECIFICATIONS – Spectral Channels, Detectors, and Purpose

Ch.	Wavelength µm	Wave Number cm-1	Detector Type	Purpose		
1	0.63	15,873	Silicon	Cloud Cover	Snow Cover	Vegetation Index
2	0.863	11,587	Silicon	Earth Radiation Budget	Surface Water Boundaries	Vegetation Index
3A	1.61	6,211	In-Ga-As	Snow/Cloud Cover	Water/Ice Clouds	Vegetation Canopy Moisture
3B	3.72	2,688	In-Sb	Water Vapor Correction	Thermal Mapping	
4	10.8	926	Hg-Cd-Te	Thermal Mapping		
5	12.0	833	Hg-Cd-Te	Water Vapor Correction	Thermal Mapping	

OPERATIONAL SURFACE AND IMAGE PRODUCTS

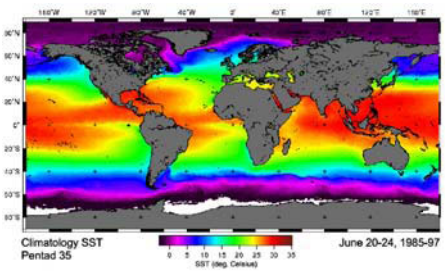

The Climatology Sea Surface Temperature (SST) data is a reprocessing of historical AVHRR SST record data, dating back to 1985. It's produced by the Physical Oceanography Distributed Active Archive Center at the Jet Propulsion Laboratory/Caltech.

THIRD GENERATION METSAT IMAGER

- 6 spectral channels
- 1.1 km diameter FOV
- Small size: 30x 40x 80cm
- Low weight: <33 kg
- Low power: <29 W
- Data rate: <670 Mbps
- > 5 year demonstrated on-orbit life (3 year requirement)

SENSOR PROVIDES

- Irreplaceable calibrated radiometric inputs to the numerical weather forecast models for every continent in the world.
- Significant events imagery tracking: floods – fires – snow storms – hurricanes – volcanoes – dust storms.

Exelis Inc.
1919 West Cook Road
P. O. Box 3700
Fort Wayne, Indiana 46801
USA
260-451-6000

www.exelisinc.com

ITT EXELIS

B

Dataset of Strombolian Ballistics Parameters

B.1 Southwest 2012 Data Set

Reference	Number of Detected Particles	Duration	
		Number of Frames	Times (s)
09-27_154909271	1,788	2,692	13
09-27_155839983	3,064	1,600	8
09-28_135432903	715	1,000	5
09-30_125847157	3,015	2,352	12
09-30_131721017	975	3,698	18
09-30_132029052	4,215	9,999	50
09-30_133102430_1	648	3,300	16
09-30_133102430_2	1,255	2,485	12
09-30_134451828	5,240	4,513	23
09-30_135413067	4,382	3,376	17
10-05_144505552	1,392	2,502	13
10-05_145321701	1,558	2,215	119
10-05_150241747	1,305	2,963	15
All	29,552	3,284[a]	16[a]

[a] Mean value.

Reference	Width (cm)				
	Maximum	Minimum	Mean	Median Value	Standard Deviation
09-27_154909271	59	5.8	12	10	5.4
09-27_155839983	62	5.8	14	12	6.5
09-28_135432903	50	5.7	10	9	5.2
09-30_125847157	50	5.5	12	11	5.2
09-30_131721017	42	5.5	14	12	4.9
09-30_132029052	56	5.5	14	12	5.2
09-30_133102430_1	52	5.5	14	12	6.6
09-30_133102430_2	41	5.5	12	11	4.9
09-30_134451828	46	5.5	11	10	4.3
09-30_135413067	37	5.5	11	10	4.0
10-05_144505552	64	5.9	14	12	5.2
10-05_145321701	48	5.9	12	10	5.6
10-05_150241747	62	5.9	15	13	7.4
Mean	51	5.6	12	11	5.4

Reference	Velocity (m/s)				
	Maximum	Minimum	Mean	Median Value	Standard Deviation
09-27_154909271	224	8.3	37	27	29
09-27_155839983	218	8.4	34	27	23
09-28_135432903	199	8.4	35	25	29
09-30_125847157	198	8.0	33	25	24
09-30_131721017	158	8.9	24	20	15
09-30_132029052	195	8.1	29	24	18
09-30_133102430_1	203	9.0	22	19	18
09-30_133102430_2	180	8.4	27	22	18
09-30_134451828	204	7.7	32	24	23
09-30_135413067	216	8.2	34	27	23
10-05_144505552	221	9.3	41	35	29
10-05_145321701	209	8.5	41	30	32
10-05_150241747	223	8.5	34	26	27
Mean	204	8.4	33	25	24

	Mass (kg)					
Reference	Maximum	Minimum	Mean	Median Value	Standard Deviation	Total
09-27_154909271	158	0.2	2.2	0.8	6.4	3,900
09-27_155839983	185	0.2	3.4	1.4	8.1	10,377
09-28_135432903	81	0.2	1.8	0.6	6.1	1,270
09-30_125847157	110	0.2	2.0	0.9	4.8	6,137
09-30_131721017	58	0.2	2.8	1.5	4.5	2,698
09-30_132029052	142	0.2	2.8	1.5	5.8	11,822
09-30_133102430_1	108	0.2	3.8	1.5	10	2,489
09-30_133102430_2	60	0.2	1.9	0.9	3.9	2,360
09-30_134451828	71	0.2	1.4	0.7	3.1	7,261
09-30_135413067	32	0.2	1.2	0.7	2.2	5,449
10-05_144505552	214	0.2	4.5	1.6	6.1	6,224
10-05_145321701	101	0.2	2.2	0.9	5.5	3,467
10-05_150241747	135	0.2	4.6	1.6	11	5,949
Mean	112	0.2	2.7	1.1	6.0	5,339

B.2 Southwest 2014 Data Set

Reference	Number of Detected Particles	Duration	
		Number of Frames	Times (s)
05-18_132733420	3,246	3,761	19
05-18_132801415	2,318	3,373	17
05-18_133328389	4,200	4,437	22
05-18_133918611	4,385	2,913	15
05-18_134008344	2,187	3,122	16
05-18_135314670	3,019	1,984	10
05-18_135359440	3,243	2,302	11
05-18_135801197	2,215	1,986	10
05-18_141207229	612	1,215	6.1
05-18_141608738	2,839	1,839	9.2
05-18_142529169	1,150	1,168	5.9
05-18_143354953	813	1,837	9.2
05-18_144559561	1,266	1,408	7.0
All	31,493	2,411[a]	12[a]

[a] Mean value.

Reference	Width (cm)				
	Maximum	Minimum	Mean	Median Value	Standard Deviation
05-18_132733420	50	5.7	7.7	5.7	4.5
05-18_132801415	53	5.7	7.9	5.7	4.6
05-18_133328389	58	5.7	7.5	5.7	4.4
05-18_133918611	63	5.7	7.4	5.7	4.3
05-18_134008344	53	5.7	8.1	5.7	5.1
05-18_135314670	54	5.7	7.3	5.7	3.8
05-18_135359440	70	5.7	7.3	5.7	4.3
05-18_135801197	58	5.7	8.0	5.7	5.3
05-18_141207229	54	5.7	9.9	5.7	7.7
05-18_141608738	54	5.7	7.4	5.7	3.8
05-18_142529169	54	5.7	8.8	5.7	6.3
05-18_143354953	73	5.7	12	7.1	10
05-18_144559561	55	5.7	8.5	5.7	6.1
Mean	58	5.7	8.3	5.8	5.4

Reference	Velocity (m/s)				
	Maximum	Minimum	Mean	Median Value	Standard Deviation
05-18_132733420	222	8.0	48	34	38
05-18_132801415	224	8.0	53	40	40
05-18_133328389	226	8.0	52	39	39
05-18_133918611	221	8.1	54	42	40
05-18_134008344	219	8.2	47	34	38
05-18_135314670	220	8.1	48	34	38
05-18_135359440	222	8.2	59	47	42
05-18_135801197	216	8.0	50	38	38
05-18_141207229	209	8.3	42	29	37
05-18_141608738	219	8.0	57	45	40
05-18_142529169	196	8.3	43	30	34
05-18_143354953	184	8.2	42	30	32
05-18_144559561	224	8.2	46	32	38
Mean	216	8.1	49	37	38

Reference	Mass (kg)					Total
	Maximum	Minimum	Mean	Median Value	Standard Deviation	
05-18_132733420	106	0.2	1.0	0.2	4.4	3,116
05-18_132801415	127	0.2	1.0	0.2	5.5	2,427
05-18_133328389	182	0.2	1.0	0.2	5.5	4,019
05-18_13391861l	220	0.2	0.9	0.2	5.8	4,098
05-18_134008344	117	0.2	1.2	0.2	6.2	2,714
05-18_135314670	149	0.2	0.7	0.2	4.5	2,242
05-18_135359440	268	0.2	0.9	0.2	7.1	3,001
05-18_135801197	172	0.2	1.4	0.2	7.8	3,016
05-18_141207229	125	0.2	3.0	0.2	12	1,844
05-18_141608738	122	0.2	0.8	0.2	4.0	2,151
05-18_142529169	132	0.2	1.9	0.2	8.4	2,149
05-18_143354953	287	0.2	5.8	0.3	20	4,741
05-18_144559561	157	0.2	1.8	0.2	8.5	2,280
Mean	166	0.2	1.6	0.2	7.7	2,908

B.3 Northeast 2014 Data Set

Reference	Number of Detected Particles	Duration	
		Number of Frames	Times (s)
05-17_172319583	5,021	1,737	8.7
05-17_180115473	3,952	1,535	7.7
05-17_182500440	5,316	3,232	16
05-17_185245215	5,304	2,175	11
05-17_193118327	2,582	1,494	7.5
All	22,175	2,035[a]	10[a]

[a] Mean value.

Reference	Width (cm)				
	Maximum	Minimum	Mean	Median Value	Standard Deviation
05-17_172319583	60	6.1	9.3	7.6	5.2
05-17_180115473	57	6.1	9.2	7.6	5.3
05-17_182500440	64	6.1	9.7	7.6	5.9
05-17_185245215	61	6.1	9.1	7.6	5.1
05-17_193118327	49	6.1	8.7	6.1	5.1
Mean	58	6.1	9.2	7.3	5.3

	Velocity (m/s)				
Reference	Maximum	Minimum	Mean	Median Value	Standard Deviation
05-17_172319583	240	9.4	56	42	40
05-17_180115473	232	8.7	52	39	38
05-17_182500440	237	8.8	49	35	37
05-17_185245215	237	8.6	53	40	39
05-17_193118327	234	8.7	54	40	40
Mean	235	8.7	52	38	39

	Mass (kg)					
Reference	Maximum	Minimum	Mean	Median Value	Standard Deviation	Total
05-17_172319583	194	0.2	1.5	0.3	5.9	7,554
05-17_180115473	148	0.2	1.5	0.3	6.3	6,003
05-17_182500440	223	0.2	1.9	0.3	7.6	10,255
05-17_185245215	215	0.2	1.4	0.3	5.9	7,586
05-17_193118327	84	0.2	1.4	0.2	5.3	3,542
Mean	168	0.2	1.6	0.3	6.3	6,846

C

Dataset of Strombolian Event Parameters

C.1 New South-East Crater 2012-2013 Data Set

Date	Number of Detected Events	Episode Duration		Total Radiant Energy
		Starting time (GMT,HH:MM)	Total duration (HH:MM)	
04/03/12	278	04:00	12:00	1.8×10^{10}
18/03/12	257	02:00	10:00	1.3×10^{10}
12/04/12	650	05:00	13:00	5.1×10^{10}
23/04/12	389	01:00	06:56	8.8×10^{10}
19/02/13	86	00:00	06:00	1.2×10^{10}
21/02/13	66	02:15	21:45	1.9×10^{9}
23/02/13	85	16:40	07:20	3.0×10^{9}
28/02/13	116	08:15	05:00	4.4×10^{9}

Date	Event Duration				
	Maximum	Minimum	Mean	Median Value	Standard Deviation
04/03/12	57	4.0	19	14	12
18/03/12	51	4.0	13	8.1	10
12/04/12	59	4.0	18	15	11
23/04/12	57	4.0	20	18	12
19/02/13	55	4.0	21	19	12
21/02/13	55	4.1	21	17	13
23/02/13	52	4.9	20	15	13
28/02/13	53	4.5	23	20	13
Mean	55	4.2	19	16	12

	Event Radiant Energy				
Date	Maximum	Minimum	Mean	Median Value	Standard Deviation
04/03/12	4.9×10^{8}	7.0×10^{6}	6.5×10^{7}	3.7×10^{7}	7.2×10^{7}
18/03/12	4.3×10^{8}	6.6×10^{6}	5.1×10^{7}	1.2×10^{7}	8.1×10^{7}
12/04/12	1.8×10^{9}	6.7×10^{6}	7.9×10^{7}	2.7×10^{7}	1.6×10^{8}
23/04/12	5.8×10^{9}	6.5×10^{6}	2.3×10^{8}	3.3×10^{7}	6.3×10^{8}
19/02/13	2.6×10^{9}	3.0×10^{6}	1.3×10^{8}	3.2×10^{7}	3.7×10^{8}
21/02/13	8.8×10^{7}	7.6×10^{6}	2.9×10^{7}	2.4×10^{7}	1.7×10^{7}
23/02/13	4.4×10^{8}	8.1×10^{6}	3.5×10^{7}	2.3×10^{7}	5.2×10^{7}
28/02/13	1.5×10^{8}	7.8×10^{6}	3.7×10^{7}	3.4×10^{7}	2.3×10^{7}
Mean	1.5×10^{9}	6.7×10^{7}	8.2×10^{7}	2.8×10^{7}	1.8×10^{8}

References

[**Aksakal, 2013]** Aksakal S. K. (2013). Geometric accuracy investigations of SEVIRI highresolution visible (HRV) level 1.5 Imagery. *Remote Sens.*, **5**, 2475–2491, doi:10.3390/rs5052475

[**Allard et al., 1994]** Allard P., Carbonnelle J., Métrich N., Loyer H. and Zettwoog P. (1994). Sulphur output and magma degassing budget of Stromboli volcano. *Nature*, **368**, 326–330, doi:10.1038/368326a0

[**Allard et al., 2005]** Allard P., Burton M., and Murè F. (2005). Spectroscopic evidence for a lava fountain driven by previously accumulated magmatic gas. *Nature*, **433**(7024), 407–410, doi:10.1038/nature03246

[**Amon and Pearson, 2009]** Amon F., and Pearson C. (2009). Thermal Imaging in Firefighting and Thermography Applications. *Radiometric Temperature Measurements: II. Applications*, **43**, 279–331.

[**Andronico et al., 2008]** Andronico D., Cristaldi A., and Scollo S. (2008). The 4–5 September 2007 lava fountain at South-East Crater of Mt Etna, Italy. *J. Volcanol.Geotherm.Res.*, **173**, 325–328, doi:10.1016/j.jvolgeores.2008.02.004.

[**Arora et al., 2008]** Arora N., Martins D., Ruggerio D., Tousimis E., Swistel A.J., Osborne M.P. and Simmons R.M. (2008). Effectiveness of a noninvasive digital infrared thermal imaging system in the detection of breast cancer. *The American Journal of Surgery*, **196**(4), 523–526, doi: 10.1016/j.amjsurg.2008.06.015.

[**Bai and Zhou, 2010]** Bai X. and Zhou F. (2010). Analysis of new top-hat transformation and the application for infrared dim small target detection. *Pattern Recognit.*, **43**(6), 2145–2156, doi: 10.1016/j.patcog.2009.12.023

[**Ball and Pinkerton, 2006]** Ball M. and Pinkerton H. (2006). Factors affecting the accuracy of thermal imaging cameras in volcanology. *Journal of Geophysical Research*, **111**(B11203). doi: 10.1029/2005JB003829.

[**Ballestracci and Nougier, 1984]** Ballestracci R. and Nougier J. (1984). Detection by infrared thermography and modeling of an icecapped geothermal system in Kerguelen archipelago. *Journal of Volcanology and Geothermal Research*, **20**, 85–99.

[**Barberi et al., 1993]** Barberi F., Carapezza M. L., Valenza M. and Villari L. (1993). The control of lava flow during the 1991–1992 eruption of Mt. Etna. *Journal of Volcanology and Geothermal Research*, **56**, 1–34. doi: 10.1016/0377-0273(93)90048-V.

[**Baxter, 2000]** Baxter P. J. (2000). Impacts of eruptions on human health. In: *Sigurdsson, H. (Ed.), Encyclopedia of Volcanoes. Academic Press*, pp. 1035–1043.

[**Behncke et al., 2006]** Behncke B., Neri M., Pecora E., Zanon V. (2006). The exceptional activity and growth of the Southeast Crater, Mount Etna (Italy), between 1996 and 2011. *Bull. Volcanol.*, **69**(2), 149–173, doi: 10.1007/s00445-006-0061-x.

[**Behncke et al., 2014]** Behncke B., Branca S., Corsaro R. A., De Beni E., Miraglia L. and Proietti C. (2014). The 2011–2012 summit activity of Mount Etna: Birth, growth and products of the new SE crater. *Journal of volcanology and geothermal research*, **270**, 10–21, doi:10.1016/j.jvolgeores.2013.11.012

[**Bertrand et al., 2011]** Bertrand P. R., Fhima M. and Guillin A. (2011). Off-line detection of multiple change points by the filtered derivative with p-value method. *Sequential Analysis*, **30**(2), 172–207, doi :10.1080/07474946.2011.563710

[**Bhattacharyya, 1943]** Bhattacharyya A. (1943). On a measure of divergence between two statistical populations defined by their probability distributions. *Bull.Calcutta Math. Soc.*, **35**(1), 99–109.

[**Blackburn et al., 1976]** Blackburn E., Wilson L. and Sparks R. (1976). Mechanisms and dynamics of strombolian activity. *J. Geol. Soc. Lond.*, **132**(4), 429–440, doi :10.1144/gsjgs.132.4.0429

[**Bland and Altman, 1986]** Bland J.M. and Altman D. (1986). Statistical methods for assessing agreement between two methods of clinical measurement. *The Lancet*, **327**(8476), 307–310
Originally published as Volume 1, Issue 8476.

[**Blong, 1984]** Blong R.J. (1984). *Volcanic hazards: a sourcebook on the effects of eruptions*, Academic Press, Australia, 424 p.

[**Bluth and Rose, 2004]** Bluth G.J. and Rose W.I. (2004). Observations of eruptive activity at Santiaguito volcano, Guatemala. *Journal of Volcanology and Geothermal research*, **136**(3), 297–302.

[**Bombrun et al., 2014]** Bombrun M., Barra V. and Harris A. (2014). Algorithm for particle detection and parameterization in high-frame-rate thermal video. *J. Appl. Remote Sens.*, **8**(1), 083549–083549, doi: 10.1117/1.JRS.8.083549.

[**Bombrun et al., 2015a]** Bombrun M., Harris A., Gurioli L., Battaglia J. and Barra V. (2015a). Anatomy of a Strombolian eruption: Inferences from particle data recorded with thermal video. *Journal of Geophysical Research: Solid Earth*, **120**(4), 2367–2387, doi :10.1002/2014JB011556

[**Bombrun et al., 2015b]** Bombrun M., Barra V. and Harris A. (2015b). Analysis of Thermal Video for Coarse to Fine Particle Tracking in Volcanic Explosion Plumes. *Image Analysis*, 366–376. Springer International Publishing, doi: 10.1007/978-3-319-19665-7_30

[**Bonaccorso et al., 2011]** Bonaccorso A., Caltabiano T., Currenti G., Del Negro C., Gambino S., Ganci G., ...and Boschi E. (2011). Dynamics of a lava fountain revealed by geophysical, geochemical and thermal satellite measurements: The case of the 10 April 2011 Mt. Etna eruption. *Geophysical Research Letters*, **38**(24), doi :10.1029/2011GL049637

[**Bonaccorso et al., 2013a]** Bonaccorso A., Calvari S., Currenti G., Del Negro C. , Ganci G., Linde A., Napoli R., Sacks S. and Sicali A. (2013a). From source to surface: Dynamics of Etna's lava fountains investigated by continuous strain, magnetic, ground and satellite thermal data. *Bull. Volcanol.*, **75**(690), doi:10.1007/s00445-013-0690-9.

[**Bonaccorso et al., 2013b]** Bonaccorso A., Currenti G., Linde A. and Sacks S. (2013b), New data from borehole strainmeters to infer lava fountain sources (Etna 2011-2012). *Geophys. Res. Lett.*, **40**, 3579–3584, doi:10.1002/grl.50692.

[**Bonadonna et al., 2012]** Bonadonna C., Folch A., Loughlin S. and Puempel H. (2012). Future developments in modelling and monitoring of volcanic ash clouds: outcomes from the first IAVCEI-WMO workshop on Ash Dispersal Forecast and Civil Aviation. *Bulletin of volcanology*, **74**(1), 1–10, doi : 10.1007/s00445-011-0508-6

[**Bonneville et al., 1985]** Bonneville A., Vasseur G. and Kerr Y. (1985). Satellite thermal infrared observations of Mt. Etna after the 17th March 1981 eruption. *Journal of Volcanology and Geothermal Research*, **24**, 293–313, doi: 10.1016/0377-0273(85)90074-5

[**Bonneville and Kerr, 1987]** Bonneville A. and Kerr Y. (1987). A thermal forerunner of the 28th March 1983 Mt. Etna eruption from satellite thermal infrared data. *Journal of Geodynamics*, **7**(1-2), 1–31, doi: 10.1016/0264-3707(87)90061-5

[**Branan et al., 2008]** Branan Y.K., Harris A., Watson I.M., Phillips J.C., Horton K., Williams-Jones G. and Garbeil H. (2008). Investigation of at-vent dynamics and dilution using thermal infrared thermometers at Masaya Volcano, Nicaragua. *Journal of Volcanology and Geothermal Research*, **169**, 34–47, doi: 10.1016/j.jvolgeores.2007.07.021

[**Brutzer et al., 2011]** Brutzer S., Hoferlin B. and Heidemann G. (2011). Evaluation of background subtraction techniques for video surveillance. *Computer Vision and Pattern Recognition (CVPR), 2011 IEEE Conference on*, 1937–1944, doi: 10.1109/CVPR.2011.5995508

[**Budzier et al., 2006]** Budzier H., Krause V., Böhmer S., Gerlach G. and Hoffmann U. (2006). Fast microbolometer-based infrared camera system. *DIAS Infrared GmbH*, **20**.

[**Bursik, 2001]** Bursik M. (2001). Effect of wind on the rise height of volcanic plumes. *Geophys. Res. Lett*, **28**(18), 3621–3624. doi: 10.1029/2001GL013393.

[**Butterworth, 1968]** Butterworth G.J. (1968). Effect of detector response time on the distortion of spectral peaks of gaussian shape. *J of Physics E*, **1**(12), 1165–1167, doi: 10.1088/0022-3735/1/12/305

[**Caballero et al., 2001]** Fernández-Caballero A., Castillo J. C., Serrano-Cuerda J. and Maldonado-Bascón S. (2011). Real-time human segmentation in infrared videos. *Expert Syst. Appl.*, **38**(3), 2577–2584, doi: 10.1016/j.eswa.2010.08.047.

[**Calvari et al., 2011]** Calvari S., Salerno G. G., Spampinato L., Gouhier M., La Spina A., Pecora E., Harris A.J.L., Labazuy P., Biale E. and Boschi E. (2011). An unloading foam model to constrain Etna's 11-13 January 2011 lava fountaining episode. *J. Geophys.Res.*, **116**, B11207, doi:10.1029/2011JB008407.

[**Campbell, 1986]** Campbell J. B. (1986). Introduction to Remote Sensing. *New York: The Guildford Press*, 551 p

[**Canny, 1986]** Canny J. (1986). A computational approach to edge detection. *Pattern Analysis and Machine Intelligence, IEEE Transactions on*, **PAMI-8**(6), 679–698, doi: 10.1109/TPAMI.1986.4767851

[**Carazzo et al., 2008a]** Carazzo G., Kaminski E. and Tait S. (2008a). On the rise of turbulent plumes: Quantitative effects of variable entrainment for submarine hydrothermal vents, terrestrial and extra terrestrial explosive volcanism. *Journal of Geophysical Research: Solid Earth (1978–2012)*, **113**(B9), doi: 10.1029/2007JB005458.

[**Carazzo et al., 2008b]** Carazzo G., Kaminski E. and Tait S. (2008b). On the dynamics of volcanic columns: A comparison of field data with a new model of negatively buoyant jets. *Journal of Volcanology and Geothermal Research*, **178**(1), 94–103, doi: 10.1016/j.jvolgeores.2008.01.002.

[**Carazzo et al., 2014]** Carazzo G., Girault F., Aubry T., Bouquerel H. and Kaminski E. (2014). Laboratory experiments of forced plumes in a density-stratified crossflow and implications for volcanic plumes. *Geophysical Research Letters*, **41**(24), 8759–8766, doi: 10.1002/2014GL061887.

[**Carey and Bursik, 2000]** Carey S. and Bursik. M. (2000). Volcanic plumes. In: *Sigurdsson, H. (Ed.), Encyclopedia of Volcanoes. Academic Press*, pp. 527–544.

[**Casadevall, 1993]** Casadevall T.J. (1993). Volcanic hazards and aviation safety: Lessons of the past decade, *FAA Aviation Safety Journal*, **2**(3), 1–11.

[**Cerminara et al., 2015]** Cerminara M., Ongaro T. E., Valade S. and Harris A. J.L. (2015). Volcanic plume vent conditions retrieved from infrared images: A forward and inverse modeling approach. *Journal of Volcanology and Geothermal Research*, **300**, 129–147. doi: 10.1016/j.jvolgeores.2014.12.015.

[**Choi et al., 2010]** Choi S. S., Cha S. H. and Tappert C. C. (2010). A survey of binary similarity and distance measures. *Journal of Systemics, Cybernetics and Informatics*, **8**(1), 43–48.

[**Chouet et al., 1974]** Chouet B., Hamisevicz N. and McGetchin T. R. (1974). Photoballistics of volcanic jet activity at Stromboli. *J. Geophys. Res.*, **79**(32), 4961–4976, doi: 10.1029/JB079i032p04961.

[**Cimarelli et al., 2014]** Cimarelli C., Alatorre-Ibargüengoitia M. A., Kueppers U., Scheu B. and Dingwell D. B. (2014). Experimental generation of volcanic lightning. *Geology*, **42**(1), 79–82, doi: 10.1130/G34802.1.

[**Clarke et al., 2002]** Clarke A. B., Voight B., Neri A. and Macedonio G. (2002). Transient dynamics of vulcanian explosions and column collapse. *Nature*, **415**(6874), 897–901, doi: 10.1038/415897a.

[**Colo, 2012]** Coló L. (2012). Study of vesiculation in basalt magma through volcanological, textural and geophysical analyses: The case study of Stromboli. *PhD dissertation, Department of Earth Sciences, Univ. Firenze, Florence, Italy.*

[**Crapper, 1977]** Crapper P. F. (1977). Forced plume characteristics, **Tellus**, 29, 470–475.

[**Curran, 1985]** Curran P. J. (1985). Principles of Remote Sensing. *Harlow: Longman Scientific and Technical*, 282 p.

[**Dai et al., 1995]** Dai Z., Tseng L. K. and Faeth G. M. (1995). Velocity statistics of round, fully developed, buoyant turbulent plumes. *Journal of heat transfer*, bf 117(1), 138–145, doi: 10.1115/1.2822294.

[**Daubechies, 1992]** Daubechies I. (1992). Ten lectures on wavelets. *Philadelphia: Society for industrial and applied mathematics.*, **61**, 198–202, doi: 10.1137/1.9781611970104

[**Dean et al., 1996]** Dean K. G., Searcy C., Wyatt C., George S. and Engle K. (1996, July). Monitoring volcanoes in the North Pacific Ocean region using satellite imagery, modeling and meteorological data. In *Proceedings (CD) from the Pan Pacific Hazard Conference, Vancouver, Canada***27**.

[**Dean et al., 1998]** Dean K., Servilla M., Roach A., Foster B. and Engle K. (1998). Satellite monitoring of remote volcanoes improves study efforts in Alaska. *Eos, Transactions American Geophysical Union*, **79**(35), 413–423, doi: 10.1029/98EO00316

[**Dean et al., 2002]** Dean K. G., Dehn J., Engle K., Izbekov P., Papp K. and Patrick M. (2002). Operational satellite monitoring of volcanoes at the Alaska Volcano Observatory. *Adv Environ Monit Model*, **1**(1), 3–35.

[**Dean et al., 2004]** Dean K. G., Dehn J., Papp K. R., Smith S., Izbekov P., Peterson R., ...and Steffke A. (2004). Integrated satellite observations of the 2001 eruption of Mt. Cleveland, Alaska. *Journal of Volcanology and Geothermal Research*, **135**(1), 51–73, doi: 10.1016/j.jvolgeores.2003.12.013.

[**Decker and Peck, 1967]** Decker R. W. and Peck D. L. (1967). Infrared radiation from Alae lava lake, Hawaii. *US Geol. Surv. Prof. Pap.*, **575D**, 169–175.

[**Dehn et al., 2000]** Dehn J., Dean K. and Engle K. (2000). Thermal monitoring of North Pacific volcanoes from space. *Geology*, **28**(8), 755–758, doi: 10.1130/0091-7613(2000)28.

[**Dehn et al., 2001]** Dehn J., Harris A. J. and Ripepe M. (2001, December). Infrared imaging of Strombolian eruptions. In *AGU Fall Meeting Abstracts*, **1**, 1.

[**Dehn et al., 2002]** Dehn J., Dean K. G., Engle K. and Izbekov P. (2002). Thermal precursors in satellite images of the 1999 eruption of Shishaldin Volcano. *Bulletin of Volcanology*, **64**(8), 525–534, doi: 10.1007/s00445-002-0227-0.

[**Delle Donne and Ripepe, 2012]** Delle Donne D. and Ripepe M. (2012). High-frame rate thermal imagery of Strombolian explosions: Implications for explosive and infrasonic source dynamics. *Journal of Geophysical Research: Solid Earth (1978–2012)*, **117**(B9), doi: 10.1029/2011JB008987

[**Denniss et al., 1998]** Denniss A.M., Harris A.J.L., Rothery D.A., Francis P.W. and Carlton R.W. (1998). Satellite observations of the April 1993 eruption of Lascar volcano. *International Journal of Remote Sensing*, **19**(5), 801–821. doi: 10.1080/014311698215739.

[**Dozier, 1980]** Dozier J. (1980). Satellite identification of surface radiant temperature fields of subpixel resolution. *NOAA Technical Memorandum*, NOAA-81021710, Washington DC: National Earth Satellite Service, 17 p.

[**Dozier, 1981]** Dozier J. (1981). A method for satellite identification of surface temperature fields of subpixel resolution. *Remote Sensing of Environment*, **11**, 221–229, doi: 10.1016/0034-4257(81)90021-3.

[**Faust et al., 2014]** Faust O., Acharya U. R., Ng E. Y. K., Hong T. J. and Yu W. (2014). Application of infrared thermography in computer aided diagnosis. *Infrared Physics & Technology*, **66**, 160–175, doi: 10.1016/j.infrared.2014.06.001.

[**Flannigan and Vonder Haar, 1986]** Flannigan M. D. and Vonder Haar T. H. (1986). Forest fire monitoring using NOAA satellite AVHRR. *Canadian Journal of Forest Research*, **16**, 975–982, doi: 10.1139/x86-171.

[**Formenti et al., 2003]** Formenti Y., Druitt T. H. and Kelfoun K. (2003). Characterisation of the 1997 Vulcanian explosions of Soufrière Hills Volcano, Montserrat, by video analysis. *Bulletin of Volcanology*, **65**(8), 587–605, doi: 10.1007/s00445-003-0288-8.

[**Francis and Rothery, 1987]** Francis P.W. and Rothery D. A. (1987). Using the Landsat Thematic Mapper to detect and monitor active volcanoes: an example from Lascar volcano, northern Chile. *Geology*, **15**, 614–617, doi: 10.1130/0091-7613(1987)15.

[**Fraunfelder et al., 1983]** Fraunfelder F. T., Kalina R. E., Buist A. S., Bernstein R. S. and Johnson D. S. (1983). Ocular effects following the volcanic eruptions of Mount St Helens. *Archives of ophthalmology*, **101**(3), 376–378.

[**Ganci et al., 2011]** Ganci G., Vicari A., Fortuna L. and Del Negro C. (2011). The HOTSAT volcano monitoring system based on combined use of SEVIRI and MODIS multispectral data. *Annals of Geophysics*, **54**(5), 544–550, doi: 10.4401/ag-5338

[**Ganci et al., 2012]** Ganci G., Harris A. J. L., Del Negro C., Guéhenneux Y., Cappello A., Labazuy P., ... and Gouhier M. (2012a). A year of lava fountaining at Etna: volumes from SEVIRI. *Geophysical Research Letters*, **39**, L06305. doi: 10.1029/2012GL051026.

[**Ganci et al., 2013]** Ganci G., James M. R., Calvari S. and Del Negro C. (2013). Separating the thermal fingerprints of lava flows and simultaneous lava fountaining using ground-based thermal camera and SEVIRI measurements. *Geophysical Research Letters*, **40**(19), 5058–5063, doi: 10.1002/grl.50983.

[**Gaudin et al., 2014a]** Gaudin D., Moroni M., Taddeucci J., Scarlato P. and Shindler L. (2014). Pyroclast Tracking Velocimetry: A particle tracking velocimetry-based tool for the study of Strombolian explosive eruptions. *Journal of Geophysical Research: Solid Earth*, **119**(7), 5369–5383, doi: 10.1002/2014JB011095.

[**Gaudin et al., 2014b]** Gaudin D., Taddeucci J., Scarlato P., Moroni M., Freda C., Gaeta M. and Palladino D. M. (2014). Pyroclast Tracking Velocimetry illuminates bomb ejection and explosion dynamics at Stromboli (Italy) and Yasur (Vanuatu) volcanoes. *Journal of Geophysical Research: Solid Earth*, **119**(7), 5384–5397, doi: 10.1002/2014JB011096.

[**Gawarecki et al., 1965]** Gawarecki S. J., Lyon R. J. P. and Nordberg W. (1965). Infrared spectral returns and imagery of the Earth from space and their application

to geological problems, Scientific Experiments for Manned Orbital Flight. *American Astronautical Society Science and Technology Series*, **4**, 13–133.

[**Genco et al., 2014]** Genco R., Ripepe M., Marchetti E., Bonadonna C. and Biass S. (2014). Acoustic wavefield and Mach wave radiation of flashing arcs in strombolian explosion measured by image luminance. *Geophysical Research Letters*, **41**(20), 7135–7142, doi: 10.1002/2014GL061597.

[**Goto et al., 2014]** Goto A., Ripepe M. and Lacanna G. (2014). Wideband acoustic records of explosive volcanic eruptions at Stromboli: New insights on the explosive process and the acoustic source. *Geophysical Research Letters*, **41**(11), 3851–3857, doi: 10.1002/2014GL060143.

[**Gouhier et al., 2012]** Gouhier M., Harris A., Calvari S., Labazuy P., Guéhenneux Y., Donnadieu F. and Valade S. (2012). Lava discharge during Etna's January 2011 fire fountain tracked using MSG-SEVIRI. *Bulletin of Volcanology*, **74**(4), 787–793, doi: 10.1007/s00445–011–0572-y.

[**Gudmundsson et al., 2011]** Gudmundsson G. (2011). Respiratory health effects of volcanic ash with special reference to Iceland. A review. *The clinical respiratory journal*, **5**(1), 2–9, doi: 10.1111/j.1752-699X.2010.00231.x.

[**Gudmundsson et al., 2012]** Gudmundsson M. T., Thordarson T., Höskuldsson Á., Larsen G., Björnsson H., Prata F. J., ... and Jónsdóttir I. (2012). Ash generation and distribution from the April-May 2010 eruption of Eyjafjallajökull, Iceland. *Scientific reports*, **2**(572). doi: doi:10.1038/srep00572.

[**Gurioli et al., 2013]** Gurioli L., Harris A. J., Colò L., Bernard J., Favalli M., Ripepe M. and Andronico D. (2013). Classification, landing distribution, and associated flight parameters for a bomb field emplaced during a single major explosion at Stromboli, Italy. *Geology*, **41**(5), 559–562, doi: 10.1130/G33967.1.

[**Gurioli et al., 2014]** Gurioli L., Colò L., Bollasina A. J., Harris A. J. L., Whittington A. and Ripepe M. (2014). Dynamics of Strombolian explosions: inferences from field and laboratory studies of erupted bombs from Stromboli volcano. *Journal of Geophysical Research: Solid Earth*, **119**(1), 319–345, doi: 10.1002/2013JB010355.

[**Harris, 1996]** Harris A. J. L. (1996). Towards automated fire monitoring from space: semi-automated mapping of the January 1994 New South Wales wild-fires using AVHRR data. *International Journal of Wildland Fire*, **6**(3), 107–116. doi: 10.1071/WF9960107.

[**Harris, 2013]** Harris A. J. L. (2013). *Thermal Remote Sensing of Active Volcanoes: A User's Manual*, Cambridge Univ. Press, Cambridge, U. K.

[**Harris et al., 1995]** Harris A. J. L., Swabey S. E. J. and Higgins J. (1995). Automated thresholding of active lavas using AVHRR data. *International Journal of Remote Sensing*, **16**(18), 3681–3686, doi: 10.1080/01431169508954654.

[**Harris et al., 1996]** Harris A. J. L., Stevens N. F., Maciejewski A. J. H. and Röllin P. J. (1996). Thermal evidence for linked vents at Stromboli. *Acta Vulcanologica*, **8**, 57–62.

[**Harris et al., 1997a]** Harris A. J. L. and Stevenson D. S. (1997a). Thermal observations of degassing open conduits and fumaroles at Stromboli and Vulcano using remotely sensed data. *Journal of Volcanology and Geothermal Research*, **76**, 175–198.

[**Harris et al., 1997b]** Harris A. J. L. and Stevenson D. S. (1997b). Magma budgets and steady-state activity of Vulcano and Stromboli volcanoes. *Geophysical Research Letters*, **24**(9), 1043–1046.

[**Harris et al., 1997c]** Harris A. J., Butterworth A. L., Carlton R. W., Downey I., Miller P., Navarro P. and Rothery D. A. (1997c). Low-cost volcano surveillance from space: case studies from Etna, Krafla, Cerro Negro, Fogo, Lascar and Erebus. *Bulletin of Volcanology*, **59**(1), 49–64, doi: 10.1007/s004450050174.

[**Harris et al., 1997d]** Harris A.J.L., Blake S., Rothery D.A. and Stevens N.F. (1997d). A chronology of the 1991 to 1993 Etna eruption using AVHRR data: implications for real time thermal volcano monitoring. *Journal of Geophysical Research*, **102**(B4), 7985–8003. doi: 10.1029/96JB03388.

[**Harris et al., 1999]** Harris A.J.L., Wright R. and Flynn L.P. (1999). Remote monitoring of Mount Erebus Volcano, Antarctica, using Polar Orbiters: Progress and Prospects. *Internal Journal of Remote Sensing*, **20**(15&16), 3051–3071. doi: 10.1080/014311699211615.

[**Harris and Neri, 2002]** Harris A. J. L. and Neri M. (2002). Volumetric observations during paroxysmal eruptions at Mount Etna: pressurized drainage of a shallow chamber or pulsed supply? *Journal of Volcanology and Geothermal Research*, **116**, 79–95, doi: 10.1016/S0377-0273(02)00212-3.

[**Harris et al., 2002]** Harris A. J. L., Flynn L. P., Matias, O. and Rose W. I. (2002). The thermal stealth flows of Santiaguito: implications for the cooling and emplacement of dacitic block lava flows. *Geological Society of America Bulletin*, **114**(5), 533–546, doi: 10.1130/0016-7606(2002)114.

[**Harris et al., 2003a]** Harris A. J., Rose W. I. and Flynn L. P. (2003a). Temporal trends in lava dome extrusion at Santiaguito 1922–2000. *Bulletin of Volcanology*, **65**(2-3), 77–89, doi: 10.1007/s00445-002-0243-0.

[**Harris et al., 2003b]** Harris A. J., Johnson J., Horton K., Garbeil H., Ramm H., Pilger E., ... and Marchetti E. (2003). Ground-based infrared monitoring provides new tool for remote tracking of volcanic activity. *EOS, Transactions American Geophysical Union*, **84**(40), 409–418, doi: 10.1029/2003EO400001.

[**Harris et al., 2005]** Harris A.J., Pirie D., Horton K., Garbeil H., Pilger E., Ramm H., ... and Poggi P. (2005). DUCKS: low cost thermal monitoring units for near-vent deployment. *Journal of volcanology and geothermal research*, **143**(4), 335–360, doi: 10.1016/j.jvolgeores.2004.12.007.

[**Harris and Ripepe, 2007a]** Harris A. and Ripepe M. (2007a). Synergy of multiple geophysical approaches to unravel explosive eruption conduit and source dynamics–A case study from Stromboli. *Chemie der Erde - Geochemistry*, **67**(1), 1–35, doi: 10.1016/j.chemer.2007.01.003.

[**Harris and Ripepe, 2007b]** Harris A. J. L. and Ripepe M. (2007b). Regional earthquake as a trigger for enhanced volcanic activity: evidence from MODIS thermal data. *Geophysical Research. Letters*, **34**, L02304. doi: 10.1029/2006GL028251.

[**Harris and Ripepe, 2007c]** Harris A. and Ripepe M. (2007c). Temperature and dynamics of degassing at Stromboli. *J. of Geophys. Res.*, **112**, B03205. doi: 10.1029/2006JB004393.

[**Harris et al., 2007]** Harris A.J.L., Dehn J. and Calvari S. (2007). Lava effusion rate definition and measurement: a review. *Bulletin of Volcanology*, **70**(1), 1–22. doi: 10.1007/s00445-007-0120-y.

[**Harris et al., 2008]** Harris A. J., Ripepe M., Calvari S., Lodato L. and Spampinato L. (2008). The 5 April 2003 explosion of Stromboli: timing of eruption dynamics using thermal data. *The Stromboli Volcano: An Integrated Study of the 2002-2003 Eruption*, 305–316, doi: 10.1029/182GM25.

[**Harris et al., 2012]** Harris A. J., Ripepe M. and Hughes E. A. (2012). Detailed analysis of particle launch velocities, size distributions and gas densities during normal explosions at Stromboli. *Journal of Volcanology and Geothermal Research*, **231**, 109–131, doi: 10.1016/j.jvolgeores.2012.02.012.

[**Harris et al., 2013a]** Harris A. J.L., Delle Donne D., Dehn J., Ripepe M. and Worden A. K. (2013a). Volcanic plume and bomb field masses from thermal infrared camera imagery. *Earth and Planetary Science Letters*, **365**, 77–85. doi: 10.1016/j.epsl.2013.01.004.

[**Harris et al., 2013b]** Harris A. J. L., Valade S., Sawyer G. M., Donnadieu F., Battaglia J., Gurioli L., ...and Lacanna G. (2013b). Modern multispectral sensors help track explosive eruptions. *Eos, Transactions American Geophysical Union*, **94**(37), 321–322, doi: 10.1002/2013EO370001.

[**Heliker and Mattox, 2003]** Heliker C. and Mattox T. N. (2003). The first two decades of the Pu'u 'O'o-Kupaianaha eruption: chronology and selected bibliography. *US Geol Surv Prof Pap*, **1676**, 1–28.

[**Holasek et al., 1996]** Holasek R. E., Self S. and Woods A. W. (1996). Satellite observations and interpretation of the 1991 Mount Pinatubo eruption plumes. *Journal of Geophysical Research: Solid Earth (1978–2012)*, **101**(B12), 27635–27655, doi: 10.1029/96JB01179

[**Holaske and Rose, 1991]** Holaske R. E. and Rose W. I. (1991). Anatomy of 1986 Augustine volcano eruptions as recorded by multispectral image processing of digital AVHRR weather satellite data. *Bulletin of Volcanology*, **53**(6), 420–435. doi: 10.1007/BF00258183.

[**Holst, 2000]** Holst G. C. (2000). *Common Sense Approach to Thermal Imaging*, JCD, Winter Park, Florida.

[**Horwell and Baxter, 2006]** Horwell C. J. and Baxter P. J. (2006). The respiratory health hazards of volcanic ash: a review for volcanic risk mitigation. *Bulletin of Volcanology*, **69**, 1–24. doi: 10.1007/s00445-006-0052-y

[**Houghton and Gonnermann, 2008]** Houghton B. F. and Gonnermann H. M. (2008). Basaltic explosive volcanism: constraints from deposits and models. *Chemie der Erde-Geochemistry*, **68**(2), 117-140, doi: 10.1016/j.chemer.2008.04.002.

[**INGV-OE Bollettino N°10, 2012]** INGV-OE, (2012). *Bollettino settimanale sul monitoraggio vulcanico, geochimico e sismico del vulcano Etna, 27/02/2012 - 04/03/2012*

[**Jaccard, 1901]** Jaccard P. (1901). *Etude comparative de la distribution florale dans une portion des Alpes et du Jura*. Impr. Corbaz.

[**James et al., 2004]** James M. R., Lane S. J., Chouet B. and Gilbert J. S. (2004). Pressure changes associated with the ascent and bursting of gas slugs in liquid-filled vertical and inclined conduits. *Journal of Volcanology and geothermal Research*, **129**(1), 61–82, doi: 10.1016/S0377-0273(03)00232-4.

[**Jaupart and Vergniolle, 1989]** Jaupart C. and Vergniolle S. (1989). The generation and collapse of a foam layer at the roof of a basaltic magma chamber. *Journal of Fluid Mechanics*, **203**, 347–380, doi: 10.1017/S0022112089001497.

[**Jaggar, 1917a]** Jaggar T.A. (1917). Volcanologic investigations at Kilauea. *Am. J. Sci.*, **44**, 161–221, doi: 10.2475/ajs.s4-44.261.161.

[**Jaggar, 1917b]** Jaggar T.A. (1917). Thermal gradient of Kilauea lava lake. *Journal of the Washington Academy of Sciences*, **7**(3), 397–405.

[**Jessop and Jellinek, 2014]** Jessop D. E. and Jellinek A. M. (2014). Effects of particle mixtures and nozzle geometry on entrainment into volcanic jets. *Geophys. Res. Lett.*, **41**(11), 3858–3863, doi: 10.1002/2014GL060059.

[**Jessop et all, 2015]** Jessop D. E., Gilchrist J., Jellinek A. M. and Roche O. (2015). The effect of inertial particles, linear and annular vents on entrainment into volcanic jets. *Earth and Planetary Science Letters*, **in prep.**.

[**Johnson et al., 2004]** Johnson J. B., Harris A. J., Sahetapy-Engel S., Wolf R. and Rose W. I. (2004). Explosion dynamics of pyroclastic eruptions at Santiaguito Volcano. *Geophysical research letters*, **31**(6), doi: 10.1029/2003GL019079.

[**Johnson et al., 2005]** Johnson J. B., Harris A. J. and Hoblitt R. P. (2005). Thermal observations of gas pistoning at Kilauea Volcano. *Journal of Geophysical Research: Solid Earth (1978–2012)*, **110**(B11), doi: 10.1029/2005JB003944.

[**Jong, 1995]** Jong A. N. (1995, September). IRST and its perspective, *SPIE's 1995 International Symposium on Optical Science, Engineering, and Instrumentation*. International Society for Optics and Photonics, 206–213.

[**Kaminski et al., 2005]** Kaminski E., Tait S. and Carazzo G. (2005). Turbulent entrainment in jets with arbitrary buoyancy. *Journal of Fluid Mechanics*, **526**, 361–376, doi: 10.1017/S0022112004003209.

[**Kilburn and Lopes, 1988]** Kilburn C.R.J. and Lopes R.M.C. (1988). The growth of aa lava flow fields on Mount Etna, Sicily. *Journal of Geophysical Research* **93**(B12), 14759–14772. doi: 10.1029/JB093iB12p14759.

[**Kilgour et al., 2010]** Kilgour G., Manville V., Della Pasqua F., Graettinger A., Hodgson K. A. and Jolly G. E. (2010). The 25 September 2007 eruption of Mount Ruapehu, New Zealand: Directed ballistics, sutseyan jets, and ice-slurry lahars, *J. Volcanol. Geotherm. Res.*, **191**, 1–14, doi: 10.1016/j.jvolgeores.2009.10.015.

[**Kylili et al., 2014]** Kylili A., Fokaides P. A., Christou P. and Kalogirou S. A. (2014). Infrared thermography (IRT) applications for building diagnostics: A review. *Appl. Energy*, **134**, 531–549, doi: 10.1016/j.apenergy.2014.08.005.

[**Langmann et al., 2012]** Langmann B., Folch A., Hensch M. and Matthias V. (2012). Volcanic ash over Europe during the eruption of Eyjafjallajökull on Iceland, April–May 2010. *Atmospheric Environment*, **48**, 1–8. doi: 10.1016/j.atmosenv.2011.03.054.

[**Lautze et al., 2004]** Lautze N. C., Harris A. J., Bailey J. E., Ripepe M., Calvari S., Dehn J., ...and Evans-Jones K. (2004). Pulsed lava effusion at Mount Etna during 2001. *Journal of volcanology and geothermal research*, **137**(1), 231-246, doi: 10.1016/j.jvolgeores.2004.05.018

[**Lautze and Houghton, 2005]** Lautze N. C. and Houghton B. F. (2005). Physical mingling of magma and complex eruption dynamics in the shallow conduit at Stromboli volcano, Italy. *Geology*, **33**(5), 425–428, doi: 10.1130/G21325.1.

[**Li et al., 2001]** Li B., Chellappa R., Zheng Q., Der S., Nasrabadi N., Chan L. and Wang L. (2001). Experimental evaluation of FLIR ATR approaches – A comparative study. *Comput. Vision Image Understanding*, **84**(1), 5–24, doi: 10.1006/cviu.2001.0938.

[**Leduc et al., 2015]** Leduc L., Gurioli L., Harris A., Colò L. and Rose-Koga E. F. (2015). Types and mechanisms of strombolian explosions: characterization of a gas-dominated explosion at Stromboli. *Bulletin of Volcanology*, **77**(1), 1–15, doi: 10.1007/s00445-014-0888-5.

[**Lorenz, 1970]** Lorenz V. (1970), Some aspects of the eruption mechanism of the Big Hole Maar, central Oregon. *Geol. Soc. Am. Bull.*, **81**, 1823–1830, doi: 10.1130/0016-7606(1970)81.

[**MacDonald, 1963]** MacDonald G. A. (1963). Physical properties of erupting Hawaiian magmas. *Geological Society of America Bulletin*, **74**(8), 1071–1078.

[**MacDonald, 1972]** Macdonald, G. A. (1972). *Volcanoes*. Englewood Cliffs (NJ): Prentice-Hall Inc., 510p.

[**MacQueen, 1967]** MacQueen J. (1967, June). Some methods for classification and analysis of multivariate observations. In *Proceedings of the fifth Berkeley symposium on mathematical statistics and probability*, **1**(14), 281–297.

[**Mahulikar, 2007]** Mahulikar S. P., Sonawane H. R. and Arvind Rao G. (2007). Infrared signature studies of aerospace vehicles. *Progress in Aerospace Sciences*, **43**(7), 218–245. doi: 10.1016/j.paerosci.2007.06.002.

[**Malin, 1980]** Malin M.C. (1980). Lengths of Hawaiian lava flows. *Geology*, **8**(7), 306–308. doi: 10.1130/0091-7613

[**Marchetti and Harris, 2008]** Marchetti E. and Harris A.J.L. (2008). Trends in activity at Pu'u 'O'o during 2001-2003: insights from the continuous thermal record. *Geological Society, London, Special Publications*, **307**, 85–101. doi: 10.1144/SP307.6

[**Marchetti et al., 2009]** Marchetti E, Ripepe M., Harris A.JL. and Delle Donne D. (2009). Tracing the differences between Vulcanian and Strombolian explosions using infrasonic and thermal radiation energy. *Earth and Planetary Science Letters*, **279**, 273–281, doi: 10.1016/j.epsl.2009.01.004

[**Marsh et al., 1980]** Marsh S. E., Switzer P., Kowalk W. S. and Lyon R. J. P. (1980). Resolving the percentage of component terrains within single resolution elements. *Photogrammetric Engineering and Remote Sensing*, **46**(8), 1079–1086.

[**Martin et al., 1986]** Martin T. R., Wehner A. P. and Butler J. (1986). Chapter 7: Evaluation of Physical Health Effects Due to Volcanic Hazards: The Use of Experimental Systems to Estimate the Pulmonary Toxicity of Volcanic Ash. *American journal of public health*, **76**(Suppl), 59–65.

[**McGetchin et al., 1974]** McGetchin T. R., Settle M. and Chouet B. A. (1974). Cinder cone growth modeled after Northeast crater, Mount Etna, Sicily. *Journal of Geophysical Research*, **79**(23), 3257–3272, doi: 10.1029/JB079i023p03257.

[**McGimsey et al., 1999]** McGimsey R. G., Schneider D. J., Neal C. A. and Roach A. L. (1999). Use of FLIR observations during eruptive repose at two Alaskan volcanoes. *Annual American Geophysical Union Meeting, San Francisco, CA, USA, December, 1999*, V32A–07.

[**Mercalli, 1907]** Mercalli G., (1907). I vulcani attivi della Terra. *Ulrico Hoepli, Milano*, 422 p.

[**Miller and Casadevall, 2000]** Miller T. P., and Casadevall T. J. (2000). Volcanic ash hazards to aviation. In: *Sigurdsson, H. (Ed.), Encyclopedia of Volcanoes. Academic Press*, pp. 915–930.

[**Morton et al., 1956]** Morton B. R., Taylor G. and Turner J. S. (1956, January). Turbulent gravitational convection from maintained and instantaneous sources. In *Proceedings of the Royal Society of London A: Mathematical, Physical and Engineering Sciences*, **234**(1196), 1–23. The Royal Society.

[**Morton, 1959]** Morton B. R. (1959). Forced plumes. *Journal of Fluid mechanics*, **5**(01), 151–163.

[**Murè et al., 2013]** Murè F., Larocca G., Spampinato L., Caltabiano T., Salerno G. G., Montalto P. and Scuderi L. (2013). Installazione di un radiometro nell'area sommitale del vulcano Etna. *Rapporti Tecnici INGV*.

[**Newhall and Self, 1982]** Newhall C. G. and Self S. (1982). The volcanic explosivity index (VEI): An estimate of explosive magnitude for historical volcanism, *J. Geophys.Res.*, **87**(C2), 1231–1238, doi:10.1029/JC087iC02p01231.

[**Oliveira and Levkowitz, 2003]** Oliveira M. C. F. and Levkowitz H. (2003). From visual data exploration to visual data mining: a survey. *Visualization and Computer Graphics, IEEE Transactions on*, **9**(3), 378–394, doi :10.1109/TVCG.2003.1207445

[**Oppenheimer, 1989]** Oppenheimer C. (1989). AVHRR volcano hot spot monitoring. *Proceedings of the 4th AVHRR data users' meeting. Rothenberg (Sweden): 3–5 September 1989*, pp. 335–338.

[**Oppenheimer, 1991]** Oppenheimer C. (1991). Lava flow cooling estimated from Landsat Thematic Mapper infrared data: the Lonquimay eruption (Chile, 1989). *Journal of Geophysical Research: Solid Earth (1978–2012)*, **96**(B13), 21865–21878, doi: 10.1029/91JB01902.

[**Oppenheimer, 1993]** Oppenheimer C. (1993). Thermal distributions of hot volcanic surfaces constrained using three infrared bands of remote sensing data. *Geophysical research letters*, **20**(6), 431–434, doi: 10.1029/93GL00500.

[**Oppenheimer, 1998]** Oppenheimer C. (1998). Review article: Volcanological applications of meteorological satellites. *International Journal of Remote Sensing*, **19**(15), 2829–2864, doi: 10.1080/014311698214307.

[**Oppenheimer and Francis, 1989]** Oppenheimer C. and Francis P. (1997). Remote sensing of heat, lava and fumarole emissions from Erta Ale volcano, Ethiopia. *International Journal of Remote Sensing*, **18**(8), 1661–1692, doi: 10.1080/014311697218043.

[**Otsu, 1979]** Otsu Nobuyuki (1979 January). A Threshold Selection Method from Gray-Level Histograms. *Systems, Man and Cybernetics, IEEE Transactions on*, **9**(1), 62–66.

[**Patrick, 2007]** Patrick M. R. (2007). Dynamics of Strombolian ash plumes from thermal video: Motion, morphology, and air entrainment. *Journal of Geophysical Research: Solid Earth (1978–2012)*, **112**(B6), doi: 10.1029/2006JB004387.

[**Patrick,et al., 2007]** Patrick M. R., Harris A. J., Ripepe M., Dehn J., Rothery D. A. and Calvari S. (2007). Strombolian explosive styles and source conditions: insights from thermal (FLIR) video. *Bulletin of volcanology*, **69**(7), 769–784, doi: 10.1007/s00445-006-0107-0.

[**Patrick,et al., 2010]** Patrick M. R., Kauahikaua J. P. and Antolik L. (2010). MATLAB tools for improved characterization and quantification of volcanic incandescence in Webcam imagery: Applications at Kilauea Volcano, Hawaii. *US Geol. Surv. Tech. Methods*, **13**, 1–16.

[**Petersen et al., 2012]** Petersen G. N., Bjornsson H. and Arason P. (2012). The impact of the atmosphere on the Eyjafjallajökull 2010 eruption plume. *Journal of Geophysical Research: Atmospheres (1984–2012)*, **117**(D20). doi: 10.1029/2011JD016762.

[**Piccardi, 2004]** Piccardi M. (2004). Background subtraction techniques: a review. In *Systems, man and cybernetics, 2004 IEEE international conference on*, **4**, 3099–3104. doi: 10.1109/ICSMC.2004.1400815.

[**Pieri and Baloga, 1986]** Pieri D.C. and Baloga S.M. (1986). Eruption rate, area, and length relationships for some Hawaiian lava flows. *Journal of Volcanology and Geothermal Research*, **30**(1), 29–45. doi: 10.1016/0377-0273(86)90066-1.

[**Pinkerton and Wilson, 1994]** Pinkerton H. and Wilson L. (1994). Factors effecting the lengths of channel-fed lava flows. *Bulletin of Volcanology*, **56**(2), 108–120. doi: 10.1007/BF00304106.

[**Pioli et al., 2008]** Pioli L., Rosi M., Calvari S. et al. (2008). The eruptive activity of 28 and 29 December 2002. *American Geophysical Union Monograph*, **182**, 105–116, doi: 10.1029/182GM10.

[**Pyle, 1998]** Pyle D. M. (1998). Forecasting sizes and repose times of future extreme volcanic events. *Geology*, **26**(4), 367–370, doi :10.1130/0091-7613

[**Ramsey and Harris, 2013]** Ramsey M. S. and Harris A. J. L. (2013). Volcanology 2020: How will thermal remote sensing of volcanic surface activity evolve over next decade?. *J. Volcanol. Geoth. Res.*, **249**, 217–233. doi: 10.1016/j.jvolgeores.2012.05.011

[**Ripepe, 1996]** Ripepe M. (1996). Evidence for gas influence on volcanic seismic signals at Stromboli. *J. Volcanol.Geotherm. Res.*, **70**, 221–233. doi:10.1016/0377-0273(95)00057-7.

[**Ripepe et al., 1993]** Ripepe M., Rossi M. and Saccorotti G. (1993). Image processing of explosive activity at Stromboli. *J. Volcanol. Geotherm. Res.*, **54**(3–4), 335–351. doi:10.1016/0377-0273(93)90071-X.

[**Ripepe et al., 2001]** Ripepe M., Ciliberto S. and Della Schiava M. (2001). Time constraints for modeling source dynamics of volcanic explosions at Stromboli. *J. Geophys. Res.*, **106**(B5), 8713–8727. doi:10.1029/2000JB900374.

[**Ripepe et al., 2002]** Ripepe M., Harris A. J. L. and Carniel R. (2002). Thermal, seismic and infrasonic evidences of variable degassing rates at Stromboli volcano. *J. Volcanol. Geoth. Res.*, **118**, 285–297. doi: 10.1016/S0377-0273(02)00298-6.

[**Ripepe et al., 2004]** Ripepe M., Marchetti E., Poggi P., Harris A.J.L., Fiaschi A. and Ulivieri G. (2004). Seismic, acoustic, and thermal network monitors the 2003 eruption of Stromboli volcano. *EOS*, **85**(35), 329–332. doi: 10.1029/2004EO350001

[**Ripepe et al., 2005]** Ripepe M., Harris A. J.L. and Marchetti E. (2005). Coupled thermal oscillations in explosive activity at different craters of Stromboli volcano. *Geophys. Res. Lett.*, **32**, L17302. doi:10.1029/2005GL022711.

[**Ripepe et al., 2008]** Ripepe M., Donne D. D., Harris A.J.L., Marchetti E. and Ulivieri G. (2008). Dynamics of Strombolian activity, *The Stromboli Volcano: An Integrated Study of the 2002-2003 Eruption*, 39–48. doi: 10.1029/182GM05.

[**Ripepe and Harris, 2008]** Ripepe M. and Harris A.J.L. (2008). Dynamics of the 5 April 2003 explosive paroxysm observed at Stromboli by a near-vent thermal, seismic and infrasonic array. *Geophysical Research Letters*, **35**, L07306. doi: 10.1029/2007GL032533.

[**Roach et al., 2001]** Roach A. L., Benoit J. P., Dean K. G. and McNutt S. R. (2001). The combined used of satellite and seismic monitoring during the 1996 eruption of Pavlof volcano, Alaska. *Bulletin of Volcanology*, **62**, 385–399. doi: 10.1007/s004450000114.

[**Rosi et al., 2000]** Rosi M., Bertagnini A. and Landi P. (2000). Onset of the persistent activity at Stromboli volcano (Italy). *Bull. Volcanol.*, **62**(4–5), 294–300. doi:10.1007/s004450000098.

[**Rose, 1987]** Rose W. I. (1987). Volcanic activity at Santiaguito Volcano, 1976–1984. *Geological Society of America Special Paper*, **212**, 17–28. doi: 10.1130/SPE212-p17.

[**Rothery et al., 1988]** Rothery D. A., Francis P.W. and Wood C. A. (1988). Volcano monitoring using short wavelength infrared data from satellites. *Journal of Geophysical Research*, **93**(B7), 7993–8008. doi: 10.1029/JB093iB07p07993.

[**Sahetapy-Engel et al., 2004]** Sahetapy-Engel S. T. M., Flynn L. P., Harris A. J. L. et al. (2004). Surface temperature and spectral measurements at Santiaguito lava dome, Guatemala. *Geophysical Research Letters*, **31**, L19610. doi: 10.1029/2004GL020683.

[**Sahetapy-Engel et al., 2008]** Sahetapy-Engel S. T., Harris A. J. L. and Marchetti E. (2008). Thermal, seismic and infrasound observations of persistent explosive activity and conduit dynamics at Santiaguito Lava Dome, Guatemala. *Journal of Volcanology and Geothermal Research*, **173**, 1–14. doi: 10.1016/j.jvolgeores.2007.11.026.

[**Sahetapy-Engel and Harris, 2009]** Sahetapy-Engel S. T. and Harris A. J. L. (2009). Thermal-image-derived dynamics of vertical ash plumes at Santiaguito volcano, Guatemala. *Bulletin of Volcanology*, **71**, 827–830. doi: 10.1007/s00445–009–0284–8

[**Savitzky and Golay, 1964]** Savitzky A. and Golay M. J. (1964). Smoothing and differentiation of data by simplified least squares procedures. *Analytical chemistry*, **36**(8), 1627–1639. doi :10.1021/ac60214a047

[**Sawyer and Sawyer, 2006]** Sawyer G. M. and Sawyer M. R. (2006). Effects of a volcanic plume on thermal imaging data. *Geophysical Research Letters*, **33**, L14311. doi: 10.1029/2005GL025320

[**Schneider et al., 2000]** Schneider D. J., Dean K. G., Dehn J., Miller T. P. and Kirilanov V.Y. (2000). Monitoring and analyses of volcanic activity using remote sensing data at the Alaska Volcano Observatory: case study for Kamchatka, Russia, December 1997. *American Geophysical Union Monograph Series*, **116**, 161–177. doi: 10.1029/GM116p0065.

[**Schott, 2007]** Schott J. R. (2007). *Remote Sensing: The Image Chain Approach*, New York: Oxford University Press, 666 p.

[**Sciotto et al., 2011]** Sciotto M., Rowe C. A., Cannata A., Arrowsmith S., Privitera E. and Gresta S. (2011, December). Investigation of Volcanic Seismo-Acoustic Signals: Applying Subspace Detection to Lava Fountain Activity at Etna Volcano. In *AGU Fall Meeting Abstracts*, **1**, 2685.

[**Scorer, 1986]** Scorer R. S. (1986). Etna: the eruption of Christmas 1985 as seen by meteorological satellite. *Weather*, **41**(12), 378–384. doi: 10.1002/j.1477-8696.1986.tb03773.x

[**Self et al., 1980]** Self S, Kienle J and Huot J (1980). Ukinrek Maars, Alaska, II. Deposits and formation of the 1977 crater. *J. Volcanol. Geotherm. Res.*, **7**(1-2), 39–65. doi:10.1016/0377-0273(80)90019-0

[**Setzer and Verstraete, 1994]** Setzer, A. W. and Verstraete M. M. (1994). Fire and glint in AVHRR's channel 3: A possible reason for the non-saturation mystery. *Remote Sensing*, **15**(3), 711–718. doi: 10.1080/01431169408954111.

[**Shimozuru, 1971]** Shimozuru D. (1971). Observation of volcanic eruption by an infrared radiation meter. *Nature*, **234**, 457–459. doi: 10.1038/234457a0.

[**Shimozuru and Kagiyama, 1978]** Shimozuru D. and Kagiyama T. (1978). A newly devised infra-red ground scanner and its application to geothermal research in volcanoes. *Journal of Volcanology and Geothermal Research*, **4**, 251–264. doi: 10.1016/0377-0273(78)90016-1.

[**Smithsonian Institution, 2005]** Smithsonian Institution, (2005). *Bulletin of the Global Volcanism Program*.

[**Soucoup and McCully, 2005]** Soucoup D. and McCully R.T. (2005). *McCully's New Brunswick: Historic Aerial Photographs, 1931-1939*. Dundurn, 141 p.

[**Spampinato et al., 2011]** Spampinato L., Calvari S., Oppenheimer C. and Boschi E. (2011). Volcano surveillance using infrared cameras. *Earth-Science Reviews*, **106**, 63–91. doi: 10.1016/j.earscirev.2011.01.003.

[**Spampinato et al., 2012]** Spampinato L., Oppenheimer C., Cannata A., Montalto P., Salerno G. G. and Calvari S. (2012). On the time-scale of thermal cycles associated with open-vent degassing. *Bulletin of volcanology*, **74**(6), 1281–1292. doi :10.1007/s00445-012-0592-2

[**Spampinato et al., 2015]** Spampinato L., Sciotto M., Cannata A., Cannavò F., La Spina A., Palano M., ...and Caltabiano T. (2015). Multi-parametric study of the February-April 2013 paroxysmal phase of Mt. Etna New South-East crater. *Geochemistry, Geophysics, Geosystems.*. doi:10.1002/2015GC005795

[**Sparks et al., 1997]** Sparks R. S. J., Bursik M. I., Carey S. N. et al. (1997). *Volcanic Plumes*. Chichester: John Wiley & Sons, 574 p.

[**Shindler et al., 2012]** Shindler L., Moroni M. and Cenedese A. (2012). Using optical flow equation for particle detection and velocity prediction in particle tracking. *Appl. Math. Comput.*, **218**(17), 8684–8694. doi:10.1016/j.amc.2012.02.030.

[**Steffke and Harris, 2011]** Steffke A. M. and Harris A. J. L. (2011). A review of algorithms for detecting volcanic hot spots in satellite infrared data. *Bulletin of Volcanology*, **73**, 1109–1137. doi: 10.1007/s00445-011-0487-7.

[**Steinberg and Babenko, 1978]** Steinberg G. S. and Babenko J. L. (1978). Gas velocity and density determination by filming gas discharges. *J. Volcanol. Geotherm. Res.*, **3**, 89–98.

[**Stevenson and Blake, 1998]** Stevenson D. S. and Blake S. (1998). Modeling the dynamics and thermodynamics of volcanic degassing. *Bull. Volcanol.*, **60**, 307–317. doi:10.1007/s004450050234.

[**Stovall et al., 2010]** Stovall W.K., Houghton B.F., Gonnermann H., Fagents S.A. and Swanson D.A. (2010). Eruption dynamics of Hawaiian-style fountains: the case study of episode 1 of the Kilauea Iki 1959 eruption. *Bull. Volcanol.*. doi: 10.1007/s00445-010-0426-z.

[**Swanson et al., 1979]** Swanson D. A., Duffield W. A., Jackson D. B. and Peterson D. B. (1979). Chronological narrative of the 1969–1971 Mauna Ulu eruption of Kilauea volcano, Hawaii. *U.S. Geol. Surv. Prof. Pap.*, **1056**, 1–59.

[**Taddeucci et al., 2012a]** Taddeucci J., Scarlato P., Capponi A., Del Bello E., Cimarelli C., Palladino D., and Kueppers U.(2012a). High-speed imaging of Strombolian explosions: The ejection velocity of pyroclasts. *Geophys. Res. Lett.*, **39**, L02301. doi:10.1029/2011GL050404.

[**Taddeucci et al., 2012b]** Taddeucci, J., Alatorre-Ibargüengoitia M. A., Moroni M., Tornetta L., Capponi A., Scarlato P., Dingwell D. B., and De Rita D. (2012b). Physical parameterization of Strombolian eruptions via experimentally-validated modeling of high-speed observations. *Geophys. Res. Lett.*, **39**, L16306. doi:10.1029/201GL052772.

[**Tazieff, 1970]** Tazieff H. (1970). New investigations on eruptive gases. *Bulletin of Volcanology*, **34**, 421–438. doi: 10.1007/BF02596766.

[**Tootell, 1985]** Tootell B. (1985). *All Four Engines Have Failed: The True and Triumphant Story of Flight BA 009 and the 'Jakarta Incident'*.

[**Tramutoli, 1998]** Tramutoli V. (1998). Robust AVHRR Techniques (RAT) for environmental monitoring: theory and applications. *Proceedings of SPIE*, **3496**, 101–113. doi: 10.1117/12.332714.

[**Turner, 1962]** Turner J. S. (1962). The "starting plume" in neutral surroundings, *J. Fluid Mech.*, **13**, 356–368. doi:10.1017/S0022112062000762.

[**Turner, 1969]** Turner J. S. (1969). Buoyant plumes and thermals. *Annual Reviews of Fluid Mechanics*, **1**, 29–44. doi: 10.1146/annurev.fl.01.010169.000333.

[**Turner, 1973]** Turner J. S. (1973). Buoyancy Effects in Fluids. *Cambridge: Cambridge University Press*, 368 p.

[**Valade et al., 2014]** Valade S. A., Harris A. J. L. and Cerminara M. (2014). Plume Ascent Tracker: Interactive Matlab software for analysis of ascending plumes in image data. *Computers & Geosciences*, **66**, 132–144. doi: 10.1016/j.cageo.2013.12.015.

[**Valentine et al., 2015]** Valentine G. A., Graettinger A. H., Macorps É., Ross P. S., White J. D., Döhring E. and Sonder I. (2015). Experiments with vertically and laterally migrating subsurface explosions with applications to the geology of phreatomagmatic and hydrothermal explosion craters and diatremes. *Bulletin of Volcanology*, **77**(3), 1–17. doi: 10.1007/s00445-015-0901-7.

[**Vanderkluysen et al., 2012]** Vanderkluysen L., Harris A. J.L., Kelfoun K., Bonadonna C. and Ripepe M. (2012). Bombs behaving badly: Unexpected trajectories and cooling of volcanic projectiles. *Bull. Volcanol.*, **74**(8), 1849–1858. doi:10.1007/s00445-012-0635-8.

[**Van der Maaten and Hinton, 2008]** Van der Maaten L. and Hinton G. (2008). Visualizing data using t-SNE. *Journal of Machine Learning Research*, **9**(2579-2605), 85.

[**Vergniolle and Brandeis, 1996]** Vergniolle S. and Brandeis G. (1996). Strombolian explosions: A large bubble breaking the surface of a lava column as a source of sound. *J. Geophys. Res.*, **101**(B9), 20433–20447. doi:10.1029/96JB01178.

[**Vergniolle and Gaudemer, 2012]** Vergniolle S. and Gaudemer Y. (2012). Decadal evolution of a degassing magma reservoir unravelled from fire fountains produced at Etna volcano (Italy) between 1989 and 2001. *Bulletin of volcanology*, **74**(3), 725–742. doi :10.1007/s00445-011-0563-z.

[**Vergniolle and Mangan, 2000]** Vergniolle S. and Mangan M. (2000). Hawaiian and Strombolian eruptions. In: *Sigurdsson, H. (Ed.), Encyclopedia of Volcanoes. Academic Press*, pp. 447–461.

[**Vergniolle and Ripepe, 2008]** Vergniolle S. and Ripepe M. (2008). From Strombolian explosions to fire fountains at Etna Volcano (Italy): what do we learn from acoustic measurements?. *Geological Society, London, Special Publications*, **307**(1), 103–124. doi: 10.1144/SP307.7

[**Wadge, 1978]** Wadge G. (1978). Effusion rate and the shape of aa lava flow fields on Mount Etna. *Geology*, **6**(8), 503–506. doi: 10.1130/0091-7613(1978)6.

[**Walker, 1971]** Walker G. (1971). Grain-size characteristics of pyroclastic deposits. *J. Geol.*, **79**(6), 696–714.

[**Walker, 1973]** Walker G. P. (1973). Explosive volcanic eruptions: A new classification scheme. *Geol. Rundsch.*, **62**(2), 431–446. doi: 10.1007/BF01840108.

[**Walker et al., 1973]** Walker G. P. L., Huntingdon A. T., Sanders A. T. and Dinsdale J. L. (1973). Lengths of lava flows [and discussion]. *Philosophical Transactions of the Royal Society of London A: Mathematical, Physical and Engineering Sciences*, **274**(1238), 107–118.

[**Washington, 1917]** Washington H. S. (1917). Persistence of vents at Stromboli and its bearing on volcanic mechanism. *Geological Society of America Bulletin*, **28**(1), 249–278. doi: 10.1130/GSAB-28-249.

[**Weill et al., 1992]** Weill A., Brandeis G., Vergniolle S., Baudin F., Bilbille J., Fèvre J. F., ...and Hill X. (1992). Acoustic sounder measurements of the vertical velocity of volcanic jets at Stromboli volcano. *Geophysical Research Letters*, **19**(23), 2357–2360. doi: 10.1029/92GL02502.

[**Wiesnet and D'Aguanno, 1982]** Wiesnet D. R. and D'Aguanno J. (1982). Thermal imagery of Mount Erebus from the NOAA-6 satellite. *Antarctic Journal of the United States*, **17**, 32–34.

[**Williams and Friedman, 1970]** Williams Jr R. S. and Friedman J. D. (1970). Satellite observation of effusive volcanism. *British Interplanetary Society Journal*, **23**(6), 441–450.

[**Wilson et al., 1978]** Wilson L., Sparks R. S. J., Huang T. C. and Watkins N. D. (1978). The control of volcanic column heights by eruption energetics and dynamics. *Journal of Geophysical Research: Solid Earth (1978–2012)*, **83**(B4), 1829–1836. doi: 10.1029/JB083iB04p01829.

[**Wohletz et al., 1989]** Wohletz K., Sheridan M. and Brown W. (1989). Particle size distributions and the sequential fragmentation/transport theory applied to volcanic ash, *J. Geophys. Res.*, **94**(B11), 15703–15721. doi:10.1029/JB094iB11p15703.

[**Wolff and Sumner, 2000]** Wolff J.A. and Sumner J.M. (2000). Lava fountains and their products. In: *Sigurdsson, H. (Ed.), Encyclopedia of Volcanoes. Academic Press*, pp. 321–329.

[**Woods, 1988]** Woods A. W. (1988). The fluid dynamics and thermodynamics of eruption columns. *Bulletin of Volcanology*, *50*(3), 169–193. doi: 10.1007/BF01079681.

[**Woods, 1995]** Woods A. (1995). The dynamics of explosive volcanic eruptions. *Rev. Geophys.*, **33**(4), 495–530. doi:10.1029/95RG02096.

[**Woods, 2010]** Woods A. W. (2010). Turbulent plumes in nature, *Annu. Rev. Fluid Mech.*, **42**, 391–412. doi:10.1146/annurev-fluid-121108–145430.

[**Wooster and Rothery, 1992]** Wooster M. J. and Rothery D. A. (1992). Thermal monitoring of Lascar Volcano. *Chile, using*, **348**, 348.

[**Wright et al., 2002]** Wright R., Flynn L., Garbeil H., Harris A. J.L. and Pilger E. (2002). Automated volcanic eruption detection using MODIS. *Remote sensing of environment*, **82**(1), 135–155.

[**Wyatt and Dean, 1995]** Wyatt W. C. and Dean K. (1995). AVHRR observations of thermal anomalies associated with the 1994 eruption of Klyuchevskoi. *AGU Fall Meeting Abstracts*, December 1995, San Francisco, F540.

[**Yilmaz et al., 2003]** Yilmaz A., Shafique K. and Shah M. (2003). Target tracking in airborne forward looking infrared imagery. *Image and Vision Computing*, **21**(7), 623–635.

[**Yuhara et al., 1981]** Yuhara K., Ehara S. and Tagomori K. (1981). Estimation of heat discharge rates using infrared measurements by a helicopter-borne thermocamera over the geothermal areas of Unzen Volcano, Japan. *Journal of Volcanology and Geothermal Research*, **9**(1), 99–109.

[**Zettwoog and Tazieff, 1972]** Zettwoog P. and Tazieff H. (1972). Instrumentation for measuring and recording mass and energy transfer from volcanoes to atmosphere. *Bulletin Volcanologique*, **36**(1), 1–19. doi: 10.1007/BF02596979

[**Zhong and Sclaroff, 2003]** Zhong J. and Sclaroff S. (2003, October). Segmenting foreground objects from a dynamic textured background via a robust kalman filter. *In Computer Vision, 2003. Proceedings. Ninth IEEE International Conference on*, 44–50 doi: 10.1109/ICCV.2003.1238312.